Analysis of Stationary Crossflow Instability on HIFiRE–5 Using Direct Numerical Simulation

A THESIS
SUBMITTED TO THE FACULTY OF THE GRADUATE SCHOOL
OF THE UNIVERSITY OF MINNESOTA
BY

Derek John Dinzl

IN PARTIAL FULFILLMENT OF THE REQUIREMENTS
FOR THE DEGREE OF
Doctor of Philosophy

Graham V. Candler, Advisor

February, 2016

Acknowledgements

First and foremost I would like to thank my advisor, Professor Graham Candler, for his support and guidance in my work, and for making my graduate career a possibility. I should extend this thanks to Professor Candler's research group, members both past and present, for their help in my work and for making my graduate experience truly awesome. Special thanks go to Dr. Ioannis Nompelis and Dr. Pramod Subbareddy, who were constant sources of expert advice. Dr. Ross Wagnild helped greatly in my understanding of boundary layer stability theory and in forming the foundation of my work. I would also like to thank Dr. Wagnild and his wife Tessa for their extreme hospitality in welcoming me into their home during my internship stays in Albuquerque, NM. Joe Brock was an excellent teammate while learning hydrodynamic stability, and we spent many late nights in the office discussing work. Ross Chaudhry provided several great suggestions for analysis of my research, and was always good for brainstorming ideas. Jeff Komives served as a voice of reason and always supplied a discerning perspective on my work. I would also like to thank Anand Kartha, Sidharth GS, and Eric Tylzcak for their input and critique.

I would like to thank Dr. Matthew Borg, Dr. Roger Kimmel , and Dr. Thomas Juliano for the several conversations about my research and their experiments on HIFiRE–5. Their collaboration helped to guide the progress of my work. I would also like to thank Matthew Lakebrink for our discussions about stationary and traveling crossflow on HIFiRE–5, and for his help in comparing our HIFiRE–5 baseflows.

I must thank Sandia National Laboratories and the members of the Aerosciences department, especially Dr. Jeff Payne and Dr. David Kuntz, who provided an excellent internship which really aided in my development as a professional and challenged my abilities.

Lastly, I want to thank my friends and family for all of their love and support, and especially my parents, who helped me become who I am today.

This work was sponsored by the Air Force Office of Scientific Research under grant FA9550–12–1–0064.

Dedication

For my parents.

Abstract

Direct numerical simulation is performed on a 38.1% scale HIFiRE–5 forebody to study stationary crossflow instability. Computations use the US3D Navier–Stokes solver to simulate Mach 6 flow at Reynolds numbers of 8.1×10^6 /m and 11.8×10^6 /m, which are conditions used by quiet tunnel experiments at Purdue University. Distributed roughness with point–to–point height variation on the computational grid and maximum heights of 0.5–4.0 μm is used with the intent to emulate smooth–body transition and excite the naturally–occurring most unstable disturbance wavenumber.

Cases at the low Reynolds number condition use three grid sizes, and hence three different roughness patterns of varying wavelength, and demonstrate that the final flow solution is extremely dependent on the particular roughness pattern. The same roughness pattern is interpolated onto each grid which yields similar solutions, indicating grid convergence.

At the high Reynolds number condition, a steady physical mechanism is introduced which explains sharp increases seen in the wall heat flux for both computations and experiment. Namely, the sharp increase is caused by large streamwise velocity disturbances impinging on the wall.

Evolution of disturbance spanwise wavelength is computed, and it is found that this wavelength is more sensitive to Reynolds number than roughness, indicating that the disturbance wavelength is primarily flow–selected for these cases. The calculation of disturbance growth rates shows the region over which crossflow disturbances behave linearly and where nonlinear effects become important. The effect of roughness height and nose sharpness are considered, and both were found to have a large effect on the resulting heating pattern. Crossflow vortex coalescence is observed and a possible cause is discussed.

Contents

List of Tables

List of Figures

Chapter 1

Introduction

The presence of turbulent flow on hypersonic flight vehicles is responsible for significantly higher heating rates compared to laminar flow, and also affects drag, noise, and other phenomena. It is thus critically important to know where the flow on a vehicle transitions from a laminar state to a turbulent one. Transition to turbulence can be caused by the presence of any one of several flow instabilities which allow small disturbances to grow to sufficiently high amplitude to cause breakdown. While the Mack modes play a dominant role in the transition of many hypersonic boundary layers, crossflow instability can be the dominant mechanism in three-dimensional flowfields. This crossflow instability is present when pressure gradients cause a component of the flow within the boundary layer to be normal to the flow direction at the top of the boundary layer. When the flow is destabilized by body roughness or another steady forcing mechanism, crossflow instability leads to the formation of stationary vortices. This phenomenon is referred to as stationary crossflow instability.

The Hypersonic International Flight Research Experimentation Program (HIFiRE) Flight 5 vehicle is a 2–to–1 elliptical cone forebody which was designed to exhibit three–dimensional transition effects including crossflow instability. HIFiRE–5 has been the subject of various experiments and computational research attempting to characterize the transition environment and learn about the instabilities present. The research herein is intended to build on that body of work by using direct numerical simulation (DNS) with US3D, a finite–volume Navier–Stokes code, to study crossflow instability on HIFiRE–5. DNS resolves all of the scales of the flow by solving the governing equations

without any additional models. Computations simulate a 38.1% scale test article and conditions based on experiments at Purdue University.

Direct numerical simulation is a useful tool for studying crossflow instability in that it overcomes many of the drawbacks of other computational stability tools by simulating the fully nonlinear governing equations. Linear stability analysis has struggled historically with correctly predicting transition locations of crossflow dominated flows. This is because the assumptions of linear analysis are generally not appropriate for stationary crossflow, particularly the assumptions that the flow is parallel and that the disturbances are linear. Furthermore, stability tools are primarily only concerned with the location of transition onset, and are limited in their usefulness to learn more about the flow physics of stationary crossflow.

DNS also has advantages over experiments because the entire flow state is known, and computational data can be examined without the observational limitations of experimental setups. The present work is thus motivated by the shortcomings of linear stability analysis and experiments in the field of stationary crossflow instability, and supplies analysis to inform the advancement of stability tools and to corroborate experimental results.

Much of the initial research on crossflow instability was concerned with swept wings at low speeds. In the compressible regime, some work has been done on elliptical cone geometries, but DNS focus has been on an axisymmetric slender cone at an angle of attack. This work extends DNS to a new geometry, HIFiRE–5, and will demonstrate that flow–specific physics are responsible for stationary crossflow behavior that differs from the slender cone.

Virtually all computational research on stationary crossflow instability has relied on exciting disturbances using isolated roughness elements or distributed roughness with a resolved characteristic wavelength. This type of forcing generally causes a crossflow disturbance pattern that has a characteristic azimuthal wavelength which is related to the roughness. However, flight vehicles normally do not have this artificial roughness, and the test articles used at Purdue upon which this work is based are polished to a fine surface finish. This motivates the question of how to properly simulate smooth body transition where the roughness does not drive the disturbance wavenumber. The present work utilizes distributed roughness with height variations that are point–to–point on the

computational grid. These height variations are on the order of microns, corresponding roughly with actual roughness heights seen on test articles with a fine finish. This strategy is used with the desire of forcing the naturally occurring, flow–selected, most unstable disturbance wavenumber.

In summary, the present work utilizes the advantages of direct numerical simulation with a unique roughness approach to learn about stationary crossflow behavior on the HIFiRE–5 geometry. The work provides new insight into complex flow phenomena and the role of microscale roughness in exciting stationary crossflow. Results are compared to experiment, and aid in the understanding of experimental findings. Chapter 2 will begin by introducing the relevant background of transition and crossflow instability, along with descriptions of the HIFiRE–5 program and the research associated with it. Chapters 3 and 4 establish the governing equations and their numerical solution, respectively. Chapter 5 considers the approach used for these simulations, and Chapter 6 discusses the results. The dissertation finishes by drawing conclusions in Chapter 7.

Chapter 2

Background

This chapter begins with a basic review of concepts relevant to the present work. The chapter continues with an explanation of crossflow instability and previous crossflow research. It concludes by summarizing the programs which the present work is based upon.

2.1 Hydrodynamic Stability and Transition to Turbulence

The concept of transition to turbulence was introduced in the early 1870's with Reynolds' pipe flow experiments.[1] The study of transition and the field of hydrodynamic stability have since been heavily studied and still contain many unsolved problems in fluid mechanics. In a boundary layer, transition is the process by which a laminar flow progresses to a turbulent state. First, disturbances are introduced to the flow via external forcing, a process known as receptivity. Second, there is a period of disturbance growth due to the presence of an instability mechanism. Lastly, the disturbances reach a critical amplitude and turbulent spots intermittently appear. Shortly downstream of this region the flow breaks down into turbulence.[2]

The receptivity process encompasses how the amplitude of an outside forcing mechanism translates to an initial disturbance amplitude. Forcing mechanisms can be unsteady, such as free stream turbulence or noise, or they can be steady, such as body roughness. These forcing mechanisms can interact in ways that are not yet well understood. Receptivity is distinct from the stability problem, and in fact provides the initial

condition.

The period after the receptivity process is the subject of hydrodynamic stability. Disturbances which are introduced to the boundary layer can be amplified when a flow instability exists. In other words, a perturbation to a flow that is unstable will result in the perturbation growing rather than the flow returning to its initial state. A *local stability* problem pertains to the stability of the local flow profile at a given point, while a *global stability* problem pertains to the stability of the whole flowfield.[3] When considering local stability, the flow is assumed to be parallel, i.e., the boundary layer is slowly developing. If a disturbance in the local flow spreads both upstream and downstream, the flow is *absolutely unstable*, and if the disturbance is instead only swept downstream the flow is *convectively unstable*. A locally parallel flow can be *temporally unstable*, meaning that a disturbance amplitude at a fixed location in space will grow in time. The flow can also be *spatially unstable*, meaning that a disturbance amplitude at a fixed time can increase as you traverse space. Temporal and spatial growth rates are related by the disturbance group velocity.

Turbulent breakdown is characterized by the formation of somewhat organized packets of eddies which are intricately mingled and evolve chaotically. Shortly upstream of where the flow is fully turbulent, the laminar boundary layer sporadically bursts into turbulent spots and then re–laminarizes. The frequency of these spots increases downstream until they merge to form a turbulent front.

2.1.1 Paths to Turbulence

Figure 2.1 shows the various paths of transition as suggested by Morkovin et al.[4]. The path that a flow will take depends on the amplitude of the environmental forcing, with Path A corresponding to small amplitudes and Path E corresponding to the largest.

When environmental forcing is very small, the non–linear interactions between disturbances have a negligible effect. This results in a period of exponential growth, and this regime is referred to as the linear growth regime. It should be noted here that the word “linear” in this case refers to the linearity of the disturbances and not the slope of the disturbance amplitude.

For intermediate environmental forcing, two disturbances which are otherwise experiencing exponential decay can cause a brief period of increase in the disturbance energy

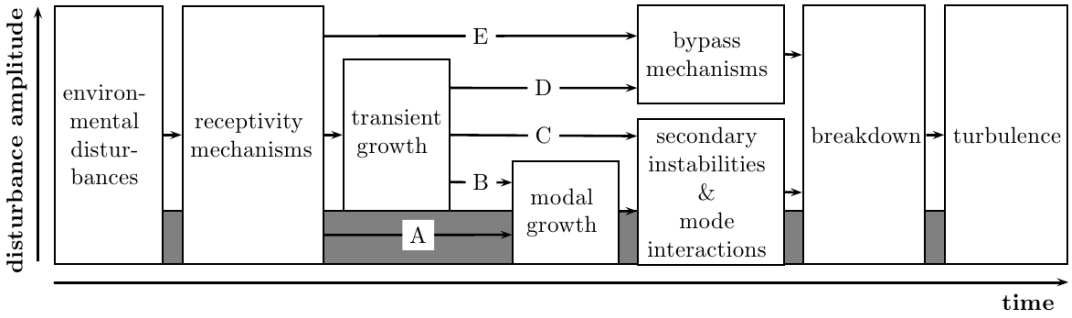

Figure 2.1: The various paths to turbulence as described by Morkovin. Image from Mack[5].

of the system. This behavior, called transient growth, is due to the non–normality of the mathematical operator governing the system.

Both linear growth and transient growth can result in disturbances that are large enough to produce new instabilities in the flow. These new instabilities are referred to as secondary instabilities, and they can in turn grow and lead to turbulent breakdown.

When environmental forcing is sufficiently large, the flow bypasses the disturbance growth regime altogether and instantly begins to break down. A common scenario where this occurs is when the flow separates while turning a corner, for instance when hitting a backward–facing step.

Crossflow instability, the topic of the present work, evolves along Path A.

2.1.2 Types of Instabilities

In a subsonic boundary layer, an inviscid instability exists when there is an inflection point in the velocity profile, and this inviscid instability is unconditionally unstable. While viscosity is typically thought of as having a stabilizing presence, a flow can also have viscous instability. In the incompressible regime, viscous instability most often results in the formation of Tollmien–Schlichting waves (T–S waves). T–S waves are vorticity disturbances which travel at the local bulk speed of the fluid in the boundary layer.

When considering hypersonic boundary layers, Mack [6] was the first to discover an infinite family of solutions to the compressible Rayleigh equation. This condition is

satisfied when a portion of the boundary layer is supersonic relative to the propagation speed of the disturbance. Figure 2.2 shows an example of a boundary layer where this is the case. The location where the disturbance phase velocity is Mach 1 relative to the bulk flow is referred to as the disturbance sonic line. Acoustic disturbances between the wall and this line become trapped in the boundary layer, because as they approach the disturbance sonic line they are effectively "lensed" back towards the wall. This family of disturbance modes is collectively referred to as the Mack modes. In this hypersonic regime, the compressible equivalent to T–S waves are called first mode disturbances, while the Mack modes begin with the second mode and higher. Second mode disturbances are the most unstable of the Mack modes, and are expected to dominate the transition process in many hypersonic boundary layers.

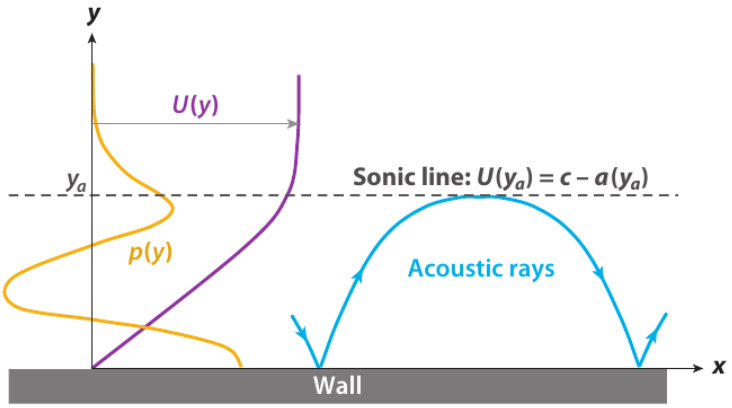

Figure 2.2: Image from Fedorov[7] depicting the trapping of Mack modes in the boundary layer.

Geometries with negative streamwise curvature are susceptible to Görtler instability. A boundary layer with no streamwise curvature has a pressure gradient that is nearly zero in the wall–normal direction. However, if there is sufficient concave curvature such that the radius of curvature is on the same order as the boundary layer, a non–zero pressure gradient will give rise to Görtler instability. This instability leads to the formation of streamwise vortices.

All of the instabilities mentioned here can have different parametric behavior when considering the effect Mach number, Reynolds number, wall cooling, etc., and each instability has been the subject of a host of research. The topic of this work is crossflow

instability, which is discussed at length in Section 2.2.

2.1.3 Traditional Solution Methodologies

Historically, much of the research on crossflow instability has employed some form of linear stability theory (LST), the basics of which are introduced in this section. The flow state is governed by the set of equations which conserves mass, momentum and energy. The variables which describe the flow can be decomposed into a basic state and a disturbance, i.e.,

$$U = U_0 + u'. \tag{2.1}$$

Subtracting the basic state equations from the governing equations results in the disturbance equations. These disturbance equations are non–linear in the disturbances and have terms which include the basic state variables. Solving the equations directly is computationally expensive, so many methods incorporate simplifying assumptions to obtain a disturbance solution. The first assumption is that disturbances have a particular form:

$$\phi\left(x, y, z, t\right) = \psi e^{i(\theta - \omega t)}. \tag{2.2}$$

Here, ϕ is the vector of disturbance variables, ψ is a shape function, and ω is a temporal frequency. The variable θ is some function of the spatial coordinates and wavenumbers. Equation 2.2 can be identified as a Fourier representation of the disturbances, where x is the streamwise direction, z is the azimuthal direction, and y is wall–normal. Typical functions for θ are given in Table 2.1. The most commonly employed method is the local method, which assumes a locally parallel flow, and that disturbances are wave–like in the x and z directions, with wavenumbers α and β, respectively. The parabolized stability equations (PSE) approach assumes that the flow is only weakly non–parallel, and accounts for upstream disturbance growth. The biglobal and triglobal approaches reduce the assumption of a wave–like solution to one direction and zero directions, respectively.

LST analysis assumes that disturbances are very small, such that their products are infinitesimal. This assumption linearizes the disturbance equations, and allows for considering the solution of one disturbance mode at a time. Utilizing these assumptions,

Method Name	θ **Function**	**Disturbance Form**
Local	$\alpha x + \beta z$	$\psi\left(y\right) e^{i(\alpha x+\beta z-\omega t)}$
PSE	$\int_{x_0}^{x} \alpha(s)ds + \beta z$	$\psi(y)e^{i\left(\int_{x_0}^{x} \alpha(s)ds+\beta z-\omega t\right)}$
BiGlobal	αx	$\psi\left(y,z\right) e^{i(\alpha x-\omega t)}$
TriGlobal	0	$\psi\left(x,y,z\right) e^{-i\omega t}$

Table 2.1: Disturbance forms for different linear stability methods.

the local method for solving the spatial stability problem reduces to an eigenvalue problem in α that can be solved in a wall–normal line at any point in the flow,

$$A\psi = \alpha\psi. \tag{2.3}$$

The eigenvalue α is complex, with the real part corresponding to the physical azimuthal wavenumber and the imaginary part corresponding to an amplification rate of the disturbances at that point. If $\alpha_i = 0$, the disturbance is neutrally stable, i.e., the disturbance does not grow or decay, and this point is called a *neutral point*. A is a sparse matrix which only depends on the basic state. Hence, the eigenvalue problem needs the basic state, a temporal frequency, and an azimuthal wavenumber as input to be solved at a point. Alternatively, the temporal stability problem can be solved using the local method, where the eigenvalue of the system is now a complex temporal frequency, and a real streamwise wavenumber must be supplied as input.

After solving for amplification rates at several points in the flow, the amplification rate can be integrated along a trajectory to get an idea of how much a disturbance may have grown along this path. The trajectory is generally selected given some insight into how the disturbance might propagate, for instance along an edge streamline. The integration allows for the calculation of the N factor[8], given by

$$N = \ln\left(\frac{A}{A_o}\right) = \int_{x_0}^{x} \sigma(s)ds \tag{2.4}$$

where A/A_0 is the disturbance amplitude over the initial disturbance amplitude, and σ is the disturbance growth rate, the form of which depends on the stability method. This calculated value of N is then empirically correlated with a value that implies the flow has transitioned. Critical N factors are typically quoted to be in the 5–10 range, depending

on the level of free stream forcing; higher forcing is associated with an expectation that the flow will transition at lower N factors [9].

PSE, biglobal, and triglobal methods reduce the number of assumptions on the stability problem at the cost of computational expense. Depending on the flow, these methods may be more appropriate and can give better answers than local analysis. Global stability methods are becoming more common with the increase in availability and power of computing resources.[10]

The governing equations are discussed in detail in Chapter 3. There are several reviews of linear stability analysis [11][12], and Mack 1984[13] is an excellent presentation of compressible stability theory.

2.2 Crossflow Instability

The discovery of crossflow instability is credited to Gray in 1952[14], who observed that transition occurred earlier on swept wings versus their unswept counterparts. Crossflow instability is caused by the existence of a pressure gradient in the boundary layer which is misaligned with the velocity vector at the edge of that boundary layer (the "edge" or "inviscid" velocity vector). This pressure gradient induces a component of flow in the spanwise direction, normal to the edge vector. Figure 2.3 shows a velocity profile which is broken down into a component parallel with the edge direction and the crossflow component. The profile of the crossflow component is bounded by a no–slip boundary condition at the wall and an asymptotic return to zero at the top of the boundary layer. These boundary conditions necessitate that an inflection point exists in the crossflow velocity profile. This inflection point is inviscidly unstable and is the source of crossflow instability.

2.2.1 Stationary and Traveling Modes

By definition, crossflow instability is exclusive to three-dimensional boundary layers. The nature by which these boundary layers develop is widely varied, but some examples for external flows are swept–wings, axisymmetric cones at angle–of–attack, and elliptic cones. Crossflow instabilities can be categorized into stationary modes and traveling modes, each of which is excited in different ways and behaves differently.

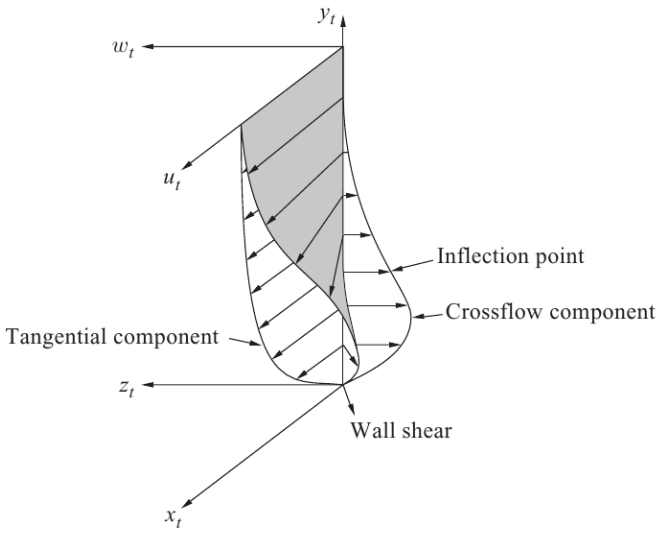

Figure 2.3: The velocity profile in a three–dimensional boundary layer decomposed into a component tangential to the edge vector and a crossflow component. From White 2005. [15]

Stationary crossflow modes are excited by wall roughness or any other steady forcing, and produce disturbances which are stationary on the geometry. The disturbances grow as they proceed downstream and can generate large streamwise vortices. These vortices are in turn susceptible to additional instabilities, referred to as *secondary* instabilities, which travel downstream along the vortices ultimately leading to a jagged transition front.

Traveling crossflow modes are excited by free stream noise and/or turbulence. These unsteady perturbations enter the boundary layer and cause vortical disturbances which travel along the geometry at bulk velocity. Traveling modes are theoretically more unstable than their stationary counterparts.

For any given case the existence of stationary and traveling modes is not mutually exclusive; in fact either can be present to varying degree and they can interact in complex ways. Müller and Bippes[16] suggested that there could be early nonlinear interaction between the two modes, and this interaction could cause either transition delay or advance. Experiments focusing on stationary crossflow modes commonly see an advance in the transition location when switching from quiet to noisy run conditions.

This suggests that excitation of the traveling modes either constructively interferes with stationary modes or that traveling modes dominate the transition process. Alternatively, Deyhle and Bippes[17] observed conditions in which a particular level of free stream turbulence excites traveling modes that inhibit the formation of stationary modes, but also grow slowly enough as to cause a transition delay. As a general rule, stationary modes can have larger initial amplitudes, but traveling modes are predicted by linear analysis to be more unstable.

For realistic flight environments and especially in Earth's upper atmosphere, the quiescent air lacks the free stream disturbances required to produce traveling crossflow instability. It is thus expected that stationary crossflow instability will dominate traveling modes under real flight conditions, and the distribution of attention in crossflow research reflects this. Work presented in this thesis will likewise focus on stationary crossflow instability.

2.2.2 Importance of Roughness

Flowfields that are dominated by stationary crossflow are very dependent on surface roughness. There are two primary types of roughness: isolated roughness, which consists of discrete elements (DREs), and distributed roughness, which includes sandpaper–like surfaces. Even finished or "smooth" surfaces have small variations which can be considered distributed roughness.

DREs are commonly used in computations and experiments because the effect of the roughness is more predictable. Elements can be placed at a particular spacing in an attempt to excite the wavenumber corresponding to that spacing. The wavenumber chosen could be selected from the most unstable wavenumber predicted by local stability theory. DREs used in this way generate disturbance patterns which are exceptionally clean in their spectral content; only the peak corresponding to the roughness–forced wavenumber is present. Figure 2.4 shows crossflow disturbances from the swept wing experiments of Reibert et al. 1996[18], and compares the effects of distributed roughness and DREs. When no artificial roughness is present (top of the figure), disturbances have varying amplitude and wavelength, with a dominant wavelength appearing more than others. When DRE's are spaced at this wavelength (bottom of figure), the disturbances become regular in amplitude and share the same roughness induced wavelength.

This example shows the qualitative difference between flowfields set up by isolated and distributed roughness.

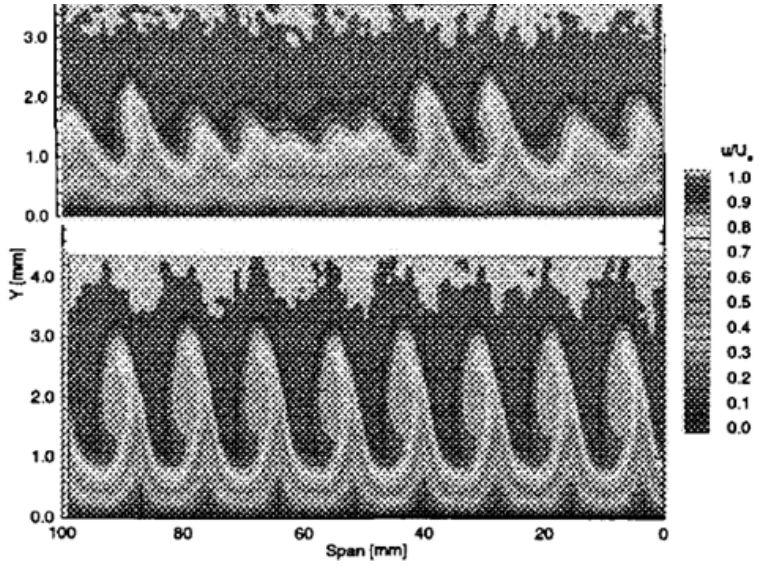

Figure 2.4: Reibert et al. 1996[18].Top: Contours of u/U_∞ in a streamwise–normal plane on a swept wing with no artificial roughness. Bottom: DREs are placed at a spacing corresponding to the most unstable wavenumber, and a single wavelength is present.

Saric et al.[19] demonstrated that DRE's could be spaced such that the resulting transition location is delayed relative to a case with no artificial roughness. This *sub-critical* roughness spacing was less than the wavelength of the naturally–selected most unstable wavenumber.

Experiments by Radeztsky et al. 1999[20] determined that roughness placed just upstream of the first neutral point produced the largest crossflow disturbances. Radeztsky et al. 1993[21] found that for swept wings, roughness near the attachment line has the largest effect on crossflow. The experiments also showed that when using isolated roughness elements, both roughness height and diameter directly affected on the transition location. The smallest diameter that was tested was 0.08 times the dominant stationary crossflow wavelength, and in this case the transition location was the same as with no artificial roughness. The transition location for this diameter remained unchanged even when the roughness height was increased from 6 to 18 μm. This suggests that isolated

roughness elements need to have a diameter larger than 8% of the dominant crossflow wavelength to be effective.

Choudhari [22] found that the dominant stationary crossflow wavelength correlated with the roughness spectrum. However, as the roughness diameter was decreased, the correlation between the roughness and the disturbance wavelength quickly decreased.

Stationary crossflow disturbances can still dominate the transition process when distributed roughness has extremely small amplitude, even for polished surfaces with roughness heights on the order of a micron. Dagenhart and Saric[23] and Bippes and Müller[24] both observed that transition patterns were fixed on their test articles regardless of changes to the experimental configuration, demonstrating that fine scale roughness was driving the pattern.

The effects of roughness on hypersonic transition problems are reviewed thoroughly by Schneider[25].

2.2.3 Nonlinear Effects and Secondary Instability

Stationary crossflow disturbances are initially small enough in amplitude that their interactions with each other are negligible, i.e., they are linear. However, the disturbances cause streamwise vorticity, which pulls low momentum fluid away from the wall into the upper high–speed portion of the boundary layer, while simultaneously depositing high momentum fluid closer to the wall. This can lead rapidly to large disturbances in the streamwise velocity, and these disturbances become large enough that non–linear interaction is then important. When disturbances reach the amplitude that non–linear effects are important, they cease to grow exponentially and instead grow algebraically. At this stage the disturbances are said to be *saturated*, and the flow can exist in this laminar state for significant periods before transition. The saturation amplitude is largely independent of roughness height.[26]

Once stationary crossflow disturbances are in the nonlinear regime, they are large enough to modify the basic state. This modified baseflow can be susceptible to additional instabilities which can grow rapidly "on top" of the crossflow vortices. These *secondary* instabilities are believed to be ultimately responsible for transition in stationary crossflow dominated flows.[27]

Secondary instability is generally broken down into three types, which are well described in Wasserman and Kloker[28], with Malik et al.[29] introducing the letter notation. These types are:

1. Type I or 'z' mode: A high frequency mode induced by the minimum in the spanwise gradient of the streamwise velocity component, originating on the updraft side of the baseflow vortex.

2. Type II or 'y' mode: A high frequency mode induced by the local maximum of the wall normal gradient of the streamwise velocity component, originating on the crest of the baseflow vortex.

3. Type III: A low frequency mode induced again by the spanwise gradient of the streamwise velocity component, originating underneath the baseflow vortex.

While the Type II instability is found to be the most unstable by linear stability analysis, Type I instabilities are generally observed in experiment. Secondary instability has been the focus of much research; some studies can be found in [15][30][31][32].

2.2.4 Use of Linear Analysis for Stationary Crossflow

The assumptions used in the stability analysis tools described in Section 2.1.3 are not ideal for the analysis of stationary crossflow instability for several reasons which are enumerated here:

1. Crossflow disturbances can grow quickly to the point where non–linear effects are important, and the assumption of LST that disturbances are linear becomes invalid.

2. Flowfields have growing boundary layers and are non–parallel. Local theory uses a parallel flow assumption.

3. Flowfields are three–dimensional. Stability tools may only have a two–dimensional implementation.

4. Stability tools can require input that is unknown and ad–hoc. Typically, temporal frequencies or spanwise wavenumbers must be selected. Solvers might sweep

through a range of these inputs, but this range must be selected by the user and can be problem dependent. Additionally, if an integration of amplification rates along some path is desired, then the evolution of these inputs must be prescribed which will also be problem dependent.

In addition to these reasons that are specific to crossflow instability, there are other complications with applying linear stability analysis. For instance, even though a baseflow may be grid converged, stability results may continue to converge with additional grid refinement. This is to say that stability results may have more stringent grid convergence requirements than the baseflow. Many of the above difficulties with applying modal analysis to crossflow are discussed by Reed and Saric[11] and Reed et al.[33]

2.2.5 History of Research

A vast majority of the early work on crossflow instability was centered around incompressible swept–wing flows. Several independent reviews exist for crossflow. Saric and Reed[34] review crossflow research from a perspective of laminar flow control. While a favorable pressure gradient stabilizes boundary layers, it is destabilizing for crossflow. Other flow control methods using roughness are also discussed. Bippes[35] reviews incompressible crossflow experiments.

Mack et al.[5] found a connection between attachment line instabilities and crossflow instabilities using global stability analysis on a swept parabolic body. This connection was first observed by Bertolotti[36] using a PSE approach.

Research of crossflow instability has shifted to compressible and hypersonic boundary layers, with older experiments using conventional (noisy) tunnel facilities. Kimmel et al.[37][38][39] investigated a Mach 8 flow over a sharp 2–to–1 elliptic cone in the von Karman Gas Dynamics' Tunnel B Facility, with corresponding linear stability analysis. Schmisseur et al.[40][41][42] used a 4–to–1 elliptic cone in the Mach 4 Purdue Quiet–flow Ludwieg Tube and perturbed the flow with laser induced thermal spots. Holden[43] summarizes work on elliptical cones at angle of attack between Mach 8—12 at Calspan University at Buffalo Research Center's LENS Facility. Stetson[44] observed transition locations for a Mach 6 flow over an 8° half angle cone at small angles of attack.

Recent work driving compressible crossflow research has featured a Mach 6 flow over

a 7° half angle slender cone at 6° angle of attack, and this geometry has been the primary focus for DNS in the field of crossflow instability. Balakumar and Owens[45] conducted a DNS on the slender cone using DREs in two configurations: in an azimuthal ring and along an axial ray on the windward side. The DREs were spaced according to the expected most unstable disturbance wavenumber computed by LST. Kuehl et al.[46] used the nonlinear parabolized stability equation (NPSE) solver JokHeR to compare to Balakumar and Owens, and found good agreement in disturbance growth rates for stationary crossflow. Gronvall et al.[47] conducted a DNS on the slender cone using a distributed roughness that was filtered to have a characteristic length scale close to the most unstable disturbance wavelength. The resulting disturbance pattern qualitatively matched very well with oil images from Swanson and Schneider[48]. Recent work by Craig and Saric[49] has used hot–wire anemometry to visualize stationary crossflow vortices on the slender cone.

2.2.6 Crossflow Disturbance Paths

Kuehl et al.[46] proposed a method for predicting the path of a crossflow disturbance using only the basic state. A path is extracted from the laminar baseflow by following the velocity vector which sits at the height of the inflection point in the crossflow profile. The physical basis for this method is that the inflection point is the source of disturbance energy, and so disturbances generated there will propagate with the local bulk velocity. They compared these extracted paths with the results of Balakumar and Owens' slender cone DNS[45] and found excellent agreement. This result was reproduced in the present work using US3D by following the velocity vector at the inflection point in the generalized momentum crossflow profile. The generalized momentum is the product of the density with the streamwise vorticity, and takes density gradients into account. Figure 2.5 uses results from the present work to recreate a plot from Kuehl et al. The figure compares DNS disturbance traces with several disturbance paths generated by following velocity vectors at different heights in the boundary layer. Previous work has used the edge streamlines as an approximation to crossflow disturbance paths, and the figure shows that it is indeed a crude approximation. On the other hand, paths extracted using the generalized momentum inflection clearly track the DNS disturbances. Extracted paths using the velocity inflection are more accurate than the edge paths, but

are still significantly different from the DNS. This indicates that the density gradient in the boundary layer plays an important role for the determination of the disturbance path.

This disturbance path prediction method is used in the present work to trace the DNS crossflow vortices on HIFiRE–5 and compute disturbance wavelengths and growth rates.

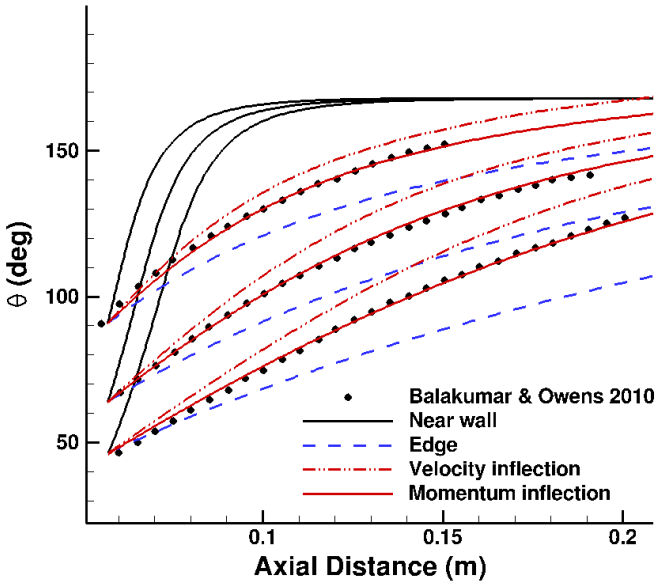

Figure 2.5: A re–creation of a plot by Kuehl et al.[46] using the US3D flow solver. Various extraction methods for predicting crossflow disturbance paths on a 7° half angle cone at 6° angle of attack in a Mach 6 flow are compared to the DNS of Balakumar and Owens[45]. Here, θ is the angle about the axis of revolution from the windward ray.

2.3 The HIFiRE–5 Geometry

The Hypersonic International Flight Research Experimentation flight 5 (HIFiRE–5)[50] program is a joint–effort between the U.S. Air Force Research Laboratories and the Australian Defense Science and Technology Organization. It is intended to research next generation hypersonic flight technologies with flight tests supported by ground tests and

computations. These flight tests feature a 2–to–1 ellipse cone forebody mounted on a sounding rocket comprising an S-30 initial stage[51] and Improved Orion[52] 2nd stage. The forebody is 0.861 m long and the minor–axis has a 7° half–angle, with a minor–axis nose radius of 2.4 mm. The vehicle flies a spin–stabilized parabolic trajectory with a maximum height of 266 km and a maximum Mach number of 7.4 upon reentry, spending a total time in–atmosphere of less than 80 seconds.

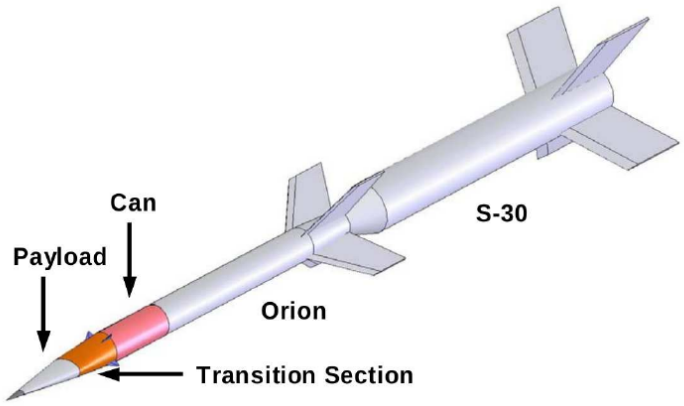

Figure 2.6: The HiFIRE–5 vehicle.

The ellipse–cone geometry was chosen for HIFiRE–5 to study transition in a three–dimensional boundary layer, with the expectation that the forebody could harbor attachment–line instabilities and crossflow instabilities, along with the more traditional first and second Mack modes. The flight trajectory provides a descent environment which sweeps through a range of Reynolds numbers of approximately $Re_L = 10^6$—1.5×10^7, and Mach numbers of approximately 6.5—7.5.

HIFiRE–5 has been the focus of much experimental and computational research. Choudhari et al.[53] details many of these efforts. Baseflows were computed using the LAURA[54], VULCAN[55], and US3D CFD codes, while stability analysis was done with the STABL[56] and LASTRAC[57] codes. Virtually all of the stability analysis assumed a linear modal disturbance form, with implementations of both LST and PSE being used. Choudhari readily explained the shortcomings of the modal approach, and elected to combine stability results with empirical correlation methods and experimental data to try to provide a high level understanding of transition on HIFiRE–5.

Numerical analysis was done for two Mach 7 flight conditions at zero angle of attack: altitudes of 18km and 33km, which correspond to Reynolds numbers of 18.47×10^6 /m and 1.65×10^6 /m, respectively. Results indicated that 2–D instability modes dominated along the minor axis ray (the centerline) and major axis ray (the attachment line), with crossflow instability dominating in the middle. Contours of N factor were generated by integrating stability results (presumably along the edge streamlines). N factors calculated for crossflow modes reached critical values extremely fast for the 18km condition. An N factor of 20 is first seen around $x/L = 0.7$, and N factors of about 12 are seen as far forward as $x/L = 0.35$. Previous research by Malik et al.[58] has suggested that transition occurs in stationary crossflow–dominated flows at N factors in the 7—12 range. N factors for the 33 km case did not surpass 5, suggesting that transition does not occur for this condition.

Stability analyses using STABL focused on the centerline and attachment line[59], where the assumptions intrinsic to 2–D linear methods should be the most valid. Results on the attachment line suggested that disturbance growth was dominated by the second mode, with the disturbance frequencies being strongly dependent on the Reynolds number. Frequencies were in the 1—3 MHz band for an altitude of 21 km, as opposed to frequencies in the range of 700—1750 kHz for the 33 km case. Disturbances for the centerline were also attributed to second mode, with encountered frequencies being much smaller (generally under 200 kHz) due to the thickened boundary layer.

In support of linear stability analysis, some traditional transition correlations were used to analyze the computed baseflows. The first is surface contours of Re_θ/M_e (where Re_θ is the Reynolds number based on the momentum thickness and M_e is the edge Mach number). The second is crossflow Reynolds number, defined as

$$Re_{cf} \equiv \frac{w_{max}\delta_{10}}{\nu_e}, \tag{2.5}$$

where w_{max} is the maximum value of the crossflow component, δ_{10} is the boundary layer thickness based on a location 10% higher than where w_{max} occurs, and ν_e is the edge kinematic viscosity. Both correlation parameters are qualitatively similar, showing high values suggesting transition near the aft of the forebody and in the midspan region for the low altitude condition. Transition correlations for hypersonic flows are discussed by

Lyttle and Reed[60].

Wind tunnel tests have focused on a 0.381 scale model at Mach 6. Visualizations of the surface heat flux are used to identify the transition front for different configurations. Tunnel data is from two facilities: The Boeing/AFOSR Mach 6 Quiet Tunnel at Purdue and the NASA 20–inch Mach 6 Tunnel at Langley Research Center (LaRC). The LaRC facility is a conventional wind tunnel which contains free stream noise levels that would cause traveling crossflow to dominate. The LaRC results are discussed by Berger et al.[61]. Results from the Purdue tunnel are discussed in Section 2.4.

Stability analysis from Choudhari et al. was run for the Purdue tunnel conditions at a unit Reynolds number of 9.84×10^6 /m. Computed N factors for stationary crossflow are shown in Figure 2.7, based on a local growth rate maximization over β. An N factor of 8 is seen as soon as $x/L = 0.65$ in the midspan region of the cone. This suggests that linear analysis predicts the flow could be transitioning near the end of the geometry for these conditions if the N factor range of 5—12 is correct.

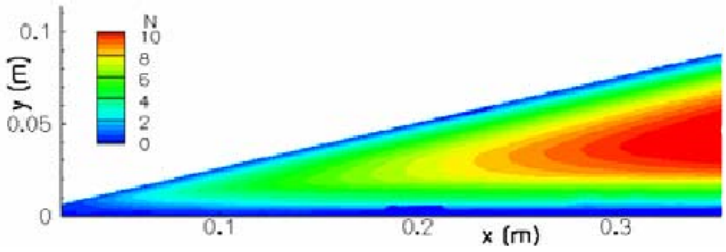

Figure 2.7: Stationary crossflow N factors from Choudhari et al. Here, y is the spanwise coordinate.

Paredes and Theofilis[62][63] have done recent work on HIFiRE–5 using BiGlobal stability analysis. Most of their work is focused on traveling crossflow and attachment line modes, and is not discussed here. Lakebrink and Borg[64] also uses linear stability analysis to study traveling crossflow on HIFiRE–5.

2.4 The Boeing/AFOSR Mach 6 Quiet Tunnel

The Boeing/AFOSR Mach 6 Quiet Tunnel Facility (BAM6QT)[65] is located at Purdue University and has been actively conducting wind tunnel experiments on HIFiRE–5 models for several years. An extremely important quality of the BAM6QT is its "quiet" nozzle, which limits the amount of noise generated due to turbulence on the nozzle walls. Free stream disturbances generated in this way provide additional energy to the receptivity process and can excite transition mechanisms which would not otherwise occur. Whereas quiet tunnels can effectively simulate a real flight environment, conventional tunnels can have noise levels an order of magnitude larger than flight [66]. The concept of quiet tunnel designs is relatively new, with the first active facility coming online in the early 1980's.[67][68]

The BAM6QT tunnel is a Ludwieg tube design[69](see Figure 2.8). A large vacuum chamber is separated from the upstream converging–diverging nozzle and test section by a diaphragm. High pressure gas is built up in the driver and nozzle. Upon the diaphragm rupturing, a shock wave propagates into the vacuum chamber while a corresponding expansion wave travels upstream. The expansion drives a subsonic flow through the nozzle, which in turn accelerates the flow to supersonic speeds. The expansion wave will continue to reflect inside the tunnel but the flow remains quiet, which allows test times of approximately 6 seconds with quasistatic pressure drop.

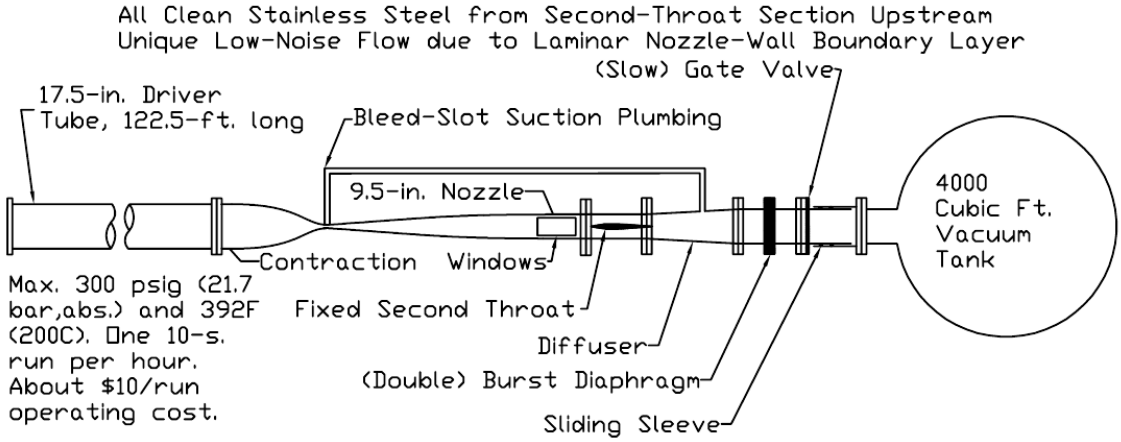

Figure 2.8: Schematic of the Boeing/AFOSR Mach 6 Quiet Tunnel.

There are many design considerations for wind tunnels that wish to achieve quiet flow. BAM6QT utilizes a nozzle with highly polished surfaces and bleed lines in front of the throat which extract the boundary layer fluid and create a new laminar boundary layer. The diverging section is very long to minimize curvature and discourage the formation of Görtler type instabilities. A 1 micron particle filter is used to remove dust and other particulates from the gas, and various screens and meshes are used to control noise generation. These controls mitigate noise levels to less than 0.05% of the freestream. The quiet run capability of the BAM6QT is critical for the study of stationary crossflow instability, as noisy tunnels can excite traveling crossflow which then dominates the transition process.

Experiments focus on a 28.1% scale model of the HIFiRE–5 forebody, which leads to a 32.8 cm long model with a 0.476 mm minor nose radius. Various models have been used, with older models utilizing temperature sensitive paint (TSP) for visualization, while a newer model is built out of polyether ether ketone (PEEK) to be used for IR thermography. The PEEK model has a stainless steel nosetip with a 0.508 μm rms roughness height that covers the first 45.8% of the geometry, and the PEEK frustum has a 2.159 μm rms roughness. A forward facing step exists at the steel/PEEK junction with a height of about 25 μm.

Many experimental configurations and parameters have been explored by varying Reynolds number, angle–of–attack and yaw angle, and noisy/quiet run conditions. Other setups have used discrete roughness elements or have offset the nosetip to create a backwards facing step. Detailed explanations of these experiments can be found in [70][71][72][73][74][75][76].

Figure 2.9 shows TSP images of quiet tunnel runs for the HIFiRE–5 model from Borg et al.[72] The images show the formation of stationary crossflow disturbances which cause a jagged pattern of high heat flux near the rear of the model, which looks qualitatively similar to transition fronts created by stationary crossflow on swept wings. Pressure spectra in this region show broadband fluctuations which suggest that the flow is turbulent. However, these streaks of high heating reach a maximum value and then the heating rate is lower downstream, which is a counterintuitive result for turbulent flow. Additionally, these streaks maintain their structure and are distinctly separate from each other even at the end of the viewing window. The present work provides

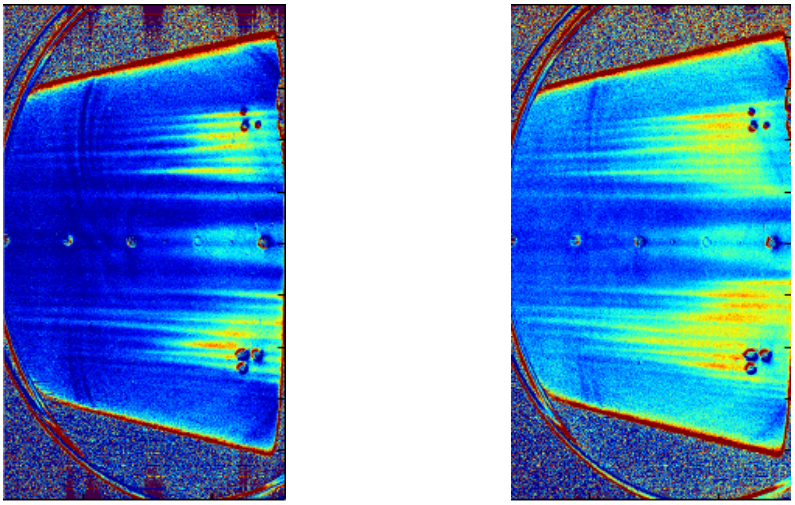

(a) $Re = 12.1 \times 10^6$ /m (b) $Re = 13.1 \times 10^6$ /m

Figure 2.9: TSP images of HIFiRE–5 model from quiet tunnel experiments of Borg et al.[72]

a steady mechanism for this phenomenon and demonstrates that the flow need not be fully turbulent to display these heating patterns.

Chapter 3

The Governing Equations

This chapter introduces the governing equations of fluid dynamics relevant to this work.

3.1 The Conservation Equations

For this work, the air being simulated behaves as a continuum fluid, and fluid flows obey the conservation laws of mass, momentum and energy. These conservation laws are the foundation for computational fluid dynamics, and are introduced here.

Several assumptions can be applied for the present work to simplify the form of the equations. The first assumption is that the fluid acts as an ideal gas, which means that molecules interact as non–reacting point particles. The second assumption is that the fluid is calorically perfect. A calorically perfect gas has a constant specific heat because all the internal energy of the molecules stays in the kinetic and rotational modes. These first two assumptions are appropriate for air at low temperatures (<1200 K). The third assumption is that body forces are negligible.

The conservation equations in divergence law form for a perfect gas are

$$\frac{\partial \rho}{\partial t} + \frac{\partial}{\partial x_j}(\rho u_j) = 0, \tag{3.1}$$

$$\frac{\partial \rho u_i}{\partial t} + \frac{\partial}{\partial x_j}(\rho u_i u_j + p\delta_{ij} - \tau_{ij}) = 0, \tag{3.2}$$

$$\frac{\partial E}{\partial t} + \frac{\partial}{\partial x_j}\left((E+p)u_j + q_j + \tau_{ij}u_i\right) = 0. \tag{3.3}$$

Equation 3.2 is the Navier–Stokes equation, while the set of Equations 3.1–3.3 is colloquially referred to as the Navier–Stokes equations. ρ is the fluid density, u_i is the bulk velocity vector, p is the pressure and E is the total energy per unit volume. τ_{ij} is the deviatoric shear stress tensor, and q_j is the heat flux vector.

3.2 Constitutive Relations

The above equations are solved together with an equation of state, which in this case is the ideal gas law,

$$p = \rho R T. \tag{3.4}$$

The total energy per unit volume for a perfect gas is

$$E = \rho c_v T + 1/2 \rho u_j u_j, \tag{3.5}$$

where c_v is the constant volume specific heat and T is the temperature.

For a newtonian fluid, the shear stress is defined as

$$\tau_{ij} = \mu\left(\frac{\partial u_i}{\partial x_j} + \frac{\partial u_j}{\partial x_i}\right) + \lambda\frac{\partial u_k}{\partial x_k} \tag{3.6}$$

where μ is the dynamic viscosity and λ is the second viscosity, typically given a value of $-2/3\mu$. The heat flux vector is defined using Fourier's Law,

$$q_j = -k\frac{\partial T}{\partial x_j} \tag{3.7}$$

where k is the thermal conductivity of the fluid. k can be related to the viscosity by the Prandtl number, $Pr = c_p\mu/k$.

The dynamic viscosity is a function of temperature set by Sutherland's Law,

$$\mu = \frac{AT^{3/2}}{B+T}, \tag{3.8}$$

where B is the Sutherland temperature and A is a property of the gas,

$$A = \frac{\mu_{ref}}{T_{ref}^{3/2}} \left(T_{ref} + B\right), \tag{3.9}$$

where μ_{ref} is the reference viscosity at the reference temperature T_{ref}.

3.3 The Finite Volume Formulation

The conservation equations (3.1–3.3) are in divergence law form and can be written in vector notation as

$$\frac{\partial U}{\partial t} + \nabla \cdot \vec{F} = 0, \tag{3.10}$$

where U is the vector of conserved variables

$$U = [\rho, \rho u, \rho v, \rho w, E]^T, \tag{3.11}$$

and $\vec{F}$ is the flux vector. If we integrate this equation over a volume V we have

$$\int_V \frac{\partial U}{\partial t} dv = -\int_V \nabla \cdot \vec{F} dv \tag{3.12}$$

Using the Divergence Theorem we obtain

$$\frac{\partial \bar{U}}{\partial t} = -\frac{1}{V} \oint_S \vec{F} \cdot \hat{n} ds \tag{3.13}$$

where $\bar{U}$ is the volume–averaged state vector.

For a finite volume cell made up of faces, this can be written in the partially discrete form

$$\frac{\partial \bar{U}}{\partial t} = -\frac{1}{V} \sum_{faces} \left(\vec{F} \cdot \hat{n}\right) S \tag{3.14}$$

where S is the area of the face and $\hat{n}$ is the outward–pointing unit normal vector associated with each face.

Chapter 4

Numerical Methods

This chapter discusses the numerical methods used in this work to solve the governing equations. The conservation equations in the form of Equation 3.14 can be solved given a method for computing the flux vector $\vec{F}$ and a time integration scheme. Methods for calculating the spatial fluxes will be discussed first.

$\vec{F}$ can be decomposed into an inviscid and viscous part:

$$\vec{F} = \vec{F}_{inv} + \vec{F}_{visc}. \tag{4.1}$$

In cartesian coordinates, The inviscid component of the flux is

$$\vec{F}_{inv} = F_{inv}\hat{i} + G_{inv}\hat{j} + H_{inv}\hat{k} \tag{4.2}$$

$$F_{inv} = \begin{bmatrix} \rho u \\ \rho uu + p \\ \rho uv \\ \rho uw \\ (E+p)u \end{bmatrix}, G_{inv} = \begin{bmatrix} \rho v \\ \rho uv \\ \rho vv + p \\ \rho vw \\ (E+p)v \end{bmatrix}, H_{inv} = \begin{bmatrix} \rho w \\ \rho uw \\ \rho vw \\ \rho ww + p \\ (E+p)w \end{bmatrix}. \tag{4.3}$$

The viscous component of the flux is

$$\vec{F}_{visc} = F_{visc}\hat{i} + G_{visc}\hat{j} + H_{visc}\hat{k} \tag{4.4}$$

$$F_{visc} = \begin{bmatrix} 0 \\ \tau_{xx} \\ \tau_{xy} \\ \tau_{xz} \\ \tau_{xx}u + \tau_{xy}v + \tau_{xz}w + q_x \end{bmatrix}, G_{visc} = \begin{bmatrix} 0 \\ \tau_{xy} \\ \tau_{yy} \\ \tau_{yz} \\ \tau_{xy}u + \tau_{yy}v + \tau_{yz}w + q_y \end{bmatrix}, \tag{4.5}$$

$$H_{visc} = \begin{bmatrix} 0 \\ \tau_{xz} \\ \tau_{yz} \\ \tau_{zz} \\ \tau_{xz}u + \tau_{yz}v + \tau_{zz}w + q_z \end{bmatrix}. \tag{4.6}$$

The inviscid and viscous components of the flux are evaluated separately using different methods. These methods are described in the following sections.

4.1 Inviscid Fluxes

The inviscid flux is entirely hyperbolic in that it propagates information along characteristics. The formulations used here leverage the method developed by Steger and Warming [77], who are credited with being the first to use a characteristic–based flux scheme to ensure stability. In this section, $\vec{F}$ refers to the inviscid component, where the subscript is dropped for presentability.

4.1.1 Steger–Warming Fluxes

The Steger–Warming method utilizes the fact that $\vec{F}$ is homogeneous with respect to the state vector, i.e.

$$\vec{F}(\lambda U) = \lambda \vec{F}(U), \tag{4.7}$$

which allows the flux to be defined exactly using a Jacobian with respect to the state vector:

$$\vec{F} = \frac{\partial \vec{F}}{\partial U} U = AU \tag{4.8}$$

A is the flux Jacobian, and the eigenvalues of A are the characteristics of the inviscid flux. Before calculating any eigenvalues, the inner product of $\vec{F}$ with the unit normal vector of the face is found, which is

$$\vec{F} \cdot \hat{n} = F' = \begin{bmatrix} \rho u' \ \rho u u' + P s'_x \\ \rho v u' + P s'_y \\ \rho w u' + P s'_z \\ (E+p) u' \end{bmatrix} \tag{4.9}$$

where $u' = u s'_x + v s'_y + w s'_z$ and the orthonormal face vector is $\hat{n} = s'_x \hat{i} + s'_y \hat{j} + s'_z \hat{k}$. The flux Jacobian for this flux is now A', and $F' = A'U$. The diagonalization of A' directly is difficult, so we instead use a change of variables which lends itself to diagonalization and then transform back. First we define the set of primitive variables

$$V = [\rho, u, v, w, T]^T. \tag{4.10}$$

A' is decomposed into $\frac{\partial F'}{\partial V}\frac{\partial V}{\partial U}$ and pre–multiplied by $\frac{\partial U}{\partial V}\frac{\partial V}{\partial U}$ (which is identity), yielding

$$A' = \frac{\partial U}{\partial V}\frac{\partial V}{\partial U}\frac{\partial F'}{\partial V}\frac{\partial V}{\partial U}. \tag{4.11}$$

This is a similarity transformation of A', and the similar matrix $\frac{\partial V}{\partial U}\frac{\partial F'}{\partial V}$ shares the same eigenvalues of A'. By construction, this matrix is much easier to compute and diagonalize. The eigenvalue decomposition is

$$\frac{\partial V}{\partial U}\frac{\partial F'}{\partial V} = C \Lambda C^{-1} \tag{4.12}$$

where Λ is a diagonal matrix which contains the eigenvalues, and C is the associated matrix which contains the eigenvectors as its columns. The eigenvalues are u' and $u' \pm a$, which represent the characteristic propagation speeds due to the bulk velocity

and acoustic waves, respectively. The inviscid flux can now be represented as

$$F' = \frac{\partial U}{\partial V} C \Lambda C^{-1} \frac{\partial V}{\partial U} U. \tag{4.13}$$

F' can be broken down into forward–moving and backward–moving parts, i.e.

$$F' = F'_+ + F'_-, \tag{4.14}$$

$$F'_\pm = \frac{\partial U}{\partial V} C \Lambda_\pm C^{-1} \frac{\partial V}{\partial U} U \tag{4.15}$$

where Λ_+ would be the matrix of only positive eigenvalues, $\frac{1}{2}(u' + |u'|)$ and $\frac{1}{2}(u' \pm a + |u' \pm a|)$. Consider the flux across a face between two elements designated by i and $i+1$, with the face being designated by $i + 1/2$. The flux can be evaluated as

$$F'_{i+1/2} = A_{+,i} U_i + A_{-,i+1} U_{i+1}. \tag{4.16}$$

This is the original flux vector–splitting scheme employed by Steger and Warming. The scheme is formally first order accurate and is very dissipative due to its upwind nature, but it makes intuitive sense in that forward moving information is evaluated using the cell behind it and vice–versa. A simple modification which reduces the numerical dissipation is to evaluate the flux Jacobians at the face. This is done by averaging the state vector of the elements on either side of the face. The resulting Modified Steger–Warming scheme is

$$F'_{i+1/2} = A_{+,i+1/2} U_i + A_{-,i+1/2} U_{i+1}, \tag{4.17}$$

$$A_{i+1/2} = A\left(\frac{1}{2}(U_i + U_{i+1})\right) \tag{4.18}$$

This flux scheme can have issues when eigenvalues are very nearly zero, particularly at the sonic line and in stagnation regions where numerical error can accumulate. The "sonic glitch correction" modifies the eigenvalues to prevent these problems. This correction is

$$\lambda'_\pm = \frac{1}{2}\left(\lambda_\pm \pm \sqrt{\lambda_\pm^2 + \epsilon^2}\right) \tag{4.19}$$

where ϵ is a small fraction of the speed of sound.

4.1.2 Higher Order Upwind Schemes

Higher order methods can be achieved by extrapolating the flux to the face. This is done by constructing a left and right state using a number of elements,

$$U^L_{i+1/2} = f\left(U_i, U_{i-1}, ...\right), \tag{4.20}$$

$$U^R_{i+1/2} = f\left(U_i, U_{i+1}, ...\right), \tag{4.21}$$

$$U_{i+1/2} = f\left(U^L_{i+1/2}, U^R_{i+1/2}\right). \tag{4.22}$$

Larger stencils are required for higher orders of accuracy. For the parts of this work which use Steger-Warming fluxes, a second order MUSCL [78] reconstruction is used. In regions of the flow with sharp discontinuities, a flux limiter must be used to force the scheme to revert to first order and limit dispersive error. The limiter is implemented as

$$F = F^{low} - \phi(r)\left(F^{low} - F^{high}\right) \tag{4.23}$$

where ϕ is the limiter, which is a function of the local rate of change in the gradient, evaluated by

$$r_i = \frac{U_i - U_{i-1}}{U_{i+1} - U_i}. \tag{4.24}$$

Therefore, in a region where r is 0, for instance when the gradient is zero or there is a sharp discontinuity, the flux is evaluated as F^{low}, the low accuracy flux scheme. In the case that the solution is smooth and $r = 0$, the flux is evaluated as F^{high}, a high accuracy scheme. For this work, the minmod limiter [79] is used:

$$\phi(r) = \max\left(0, \min(1, r)\right). \tag{4.25}$$

This limiter is as conservative as possible (it favors the dissipative flux) while still being total variation diminishing (TVD).

4.1.3 Central Schemes

While upwind schemes have the beneficial property of numerical stability, even high resolution upwind schemes contain a large amount of dissipation. It is thus advantageous to use a scheme which eliminates this source of dissipation unless it is needed. Looking again at the Modified Steger–Warming flux, it can be written as

$$F' = \left(\frac{\partial U}{\partial V} C \Lambda^{+} C^{-1} \frac{\partial V}{\partial U}\right) U_L + \left(\frac{\partial U}{\partial V} C \Lambda^{-} C^{-1} \frac{\partial V}{\partial U}\right) U_R. \tag{4.26}$$

This can be rewitten as

$$F' = \left(\frac{\partial U}{\partial V} C \frac{\Lambda + |\Lambda|}{2} C^{-1} \frac{\partial V}{\partial U}\right) U_L + \left(\frac{\partial U}{\partial V} C \frac{\Lambda - |\Lambda|}{2} C^{-1} \frac{\partial V}{\partial U}\right) U_R, \tag{4.27}$$

which can be rearranged into

$$F' = A' \left(\frac{U_L + U_R}{2}\right) + \frac{1}{2} |A'| \left(U_R - U_L\right). \tag{4.28}$$

The first and second terms on the right–hand side of Equation 4.28 are the central non–dissipative portion of the flux $F'_{central}$ and the upwinded dissipative portion of the flux F'_{diss}, respectively. These contributions can be calculated separately, with the central part being used as the flux evaluation, and the upwinded part only being added where numerical stability is needed. F'_{diss} is added in using a switch:

$$F' = F'_{central} + \alpha F'_{diss} \tag{4.29}$$

where α is a value between zero and one, and is set by some local flow quantity. The present work uses the Ducros switch [80], which is given by

$$\alpha = \frac{(\nabla \cdot \vec{u})^2}{(\nabla \cdot \vec{u})^2 + ||\vec{\omega}||^2}, \tag{4.30}$$

where $\vec{u}$ is the velocity vector and $||\vec{\omega}||$ is the magnitude of vorticity.

The central portion of the flux is evaluated using the kinetic energy–consistent (KEC) flux scheme developed by Subbareddy and Candler[81]. This flux scheme uses gradient reconstruction to produce sixth order accurate fluxes on a Cartesian mesh.

Meshes are generally not Cartesian, and so the KEC flux scheme is not formally sixth order in these cases, but the scheme is significantly less dissipative than Modified Steger–Warming.

4.2 Viscous Fluxes

Calculation of the viscous component of the flux is dependent on knowledge of the local gradients. The gradients are first computed at the cell centers and then these values are interpolated to the face. These two steps are explained in the following sections. Once the gradients are calculated at the face, the viscous fluxes are easily constructed using Equation 4.6.

4.2.1 Gradient Reconstruction

Gradients are computed at cell centers using a weighted least squares method. This method involves finding the minimum of a function evaluated for each cell,

$$f = \sum_{m=1}^{M} w_m r_m^2, \tag{4.31}$$

where the sum is over the M neighboring cells. r_m is a residual for the cell and w_m is the corresponding weight for the cell. The residual can be thought of as the difference between the actual cell–to–cell gradient and the estimated gradient. To define r_m, consider a scalar ϕ at a point i. The value of ϕ at a neighboring cell m can be estimated by the Taylor series

$$\phi_m = \phi_i + (\phi_x)_i \Delta x_{mi} + (\phi_y)_i \Delta y_{mi} + (\phi_z)_i \Delta z_{mi} + \text{T.E.} \tag{4.32}$$

where ϕ_x, ϕ_y, and ϕ_z are the partial derivatives in the x, y, and z directions, respectively, and $\Delta x_{mi} = x_m - x_i$, $\Delta y_{mi} = y_m - y_i$, and $\Delta z_{mi} = z_m - z_i$. Rearranging this equation, we have

$$\Delta\phi_{mi} = (\phi_x)_i \Delta x_{mi} + (\phi_y)_i \Delta y_{mi} + (\phi_z)_i \Delta z_{mi} + \text{T.E.} \tag{4.33}$$

where the actual change in the scalar is $\Delta\phi_{mi} = \phi_m - \phi_i$ and the estimated change is the sum of the terms on the right hand side. The residual is the difference between the two, and the function to minimize is

$$f = \sum_{m=1}^{M} w_m \left(\Delta\phi_{mi} - (\phi_x)_i \Delta x_{mi} - (\phi_y)_i \Delta y_{mi} - (\phi_z)_i \Delta z_{mi}\right)^2. \tag{4.34}$$

The minimization is done by taking the derivative of Equation 6.15 with respect to each partial derivative (e.g. $\frac{\partial}{\partial\phi_x}$) and setting to zero. This leaves a set of equations which can be solved for the desired partial derivatives. While a common selection for the weights is the inverse distance to the cell m, this work uses

$$w_m = \frac{1}{\sqrt[3]{\Delta x_{mi}^2 + \Delta y_{mi}^2 + \Delta z_{mi}^2}}, \tag{4.35}$$

which yields an approximation that is second order accurate.

4.2.2 Interpolation of Gradient to Face

Once the gradients are constructed at the cell centers, they must be interpolated to the face. A simple average between the adjacent cells is insufficient in that it is inaccurate and can cause other numerical issues. The flux is instead calculated using a deferred correction method. The viscous flux at the face can be decomposed into a component normal to the face and a component tangential to the face:

$$\nabla\phi_f = (\nabla\phi_f)_N + (\nabla\phi_f)_T \tag{4.36}$$

$$= (\nabla\phi_f \cdot \hat{n})\,\hat{n} + (\nabla\phi_f - (\nabla\phi_f \cdot \hat{n})\,\hat{n}). \tag{4.37}$$

The normal component is computed as a re–evaluation of the gradient between the two cells,

$$(\nabla\phi_f)_N \approx \left(\frac{\phi_{i+1} - \phi_i}{\Delta l}\hat{e} \cdot \hat{n}\right)\hat{n}, \tag{4.38}$$

where $\hat{e}$ is the unit vector pointing from the cell centroid at i to the cell centroid at

$i+1$, and Δl is the distance between the two centroids. The tangential component is calculated using simple averages of the gradients calculated at the cell centers and the second term on the right hand side of Equation 4.37:

$$(\nabla\phi_f)_T \approx \left(\frac{\nabla\phi_i + \nabla\phi_{i+1}}{2}\right) - \left(\frac{\nabla\phi_i + \nabla\phi_{i+1}}{2} \cdot \hat{h}\right)\hat{n}. \tag{4.39}$$

The sum of Equations 4.38 and 4.39 yields the deferred correction gradient at the face,

$$\nabla\phi_f = \frac{\nabla\phi_i + \nabla\phi_{i+1}}{2} + \left(\frac{\phi_{i+1} - \phi_i}{\Delta l}\hat{e} \cdot \hat{n} - \frac{\nabla\phi_i + \nabla\phi_{i+1}}{2} \cdot \hat{h}\right)\hat{n}. \tag{4.40}$$

4.3 Time Integration

With a scheme for the evaluation of the spatial fluxes, a method for advancing the solution in time is needed. The next sections will lay the foundation for discretizing the equations in time and applying an implicit second order accurate scheme for time integration.

4.3.1 Explicit Time Integration

Looking again at Equation 3.14, we need a discrete representation for the time derivative of the state vector. If we use a simple backwards difference, we have

$$\frac{\bar{U}^{n+1} - \bar{U}^n}{\Delta t} + \text{T.E.} = -\frac{1}{V}\sum_{faces} F'^n S \tag{4.41}$$

where n is the current time level, not to be confused with the face unit normal $\hat{n}$, and Δt is the timestep. This equation can be solved explicitly for $\bar{U}^{n+1}$ given the solution at the current time level, and is called the Explicit Euler method. It is first order accurate in time. For numerical stability, there is an upper limit on the timestep imposed by the local size of the grid. For the inviscid 1-D Euler equations, this limit is given by the CFL condition

$$\Delta t \leq \frac{\Delta x}{|u| + a}, \tag{4.42}$$

where a is the speed of sound. The reason this upper limit exists is because the numerical domain of dependence must include the physical domain of dependence. While a stability condition has not been proven to exist for the 3-D Navier–Stokes equations, one can be manufactured based on the stipulation of the previous sentence. This is given by

$$\Delta t \leq \frac{1}{\frac{|u|}{\Delta x} + \frac{|v|}{\Delta y} + \frac{|w|}{\Delta z} + a\sqrt{\frac{1}{\Delta x^2} + \frac{1}{\Delta y^2} + \frac{1}{\Delta z^2}}}. \tag{4.43}$$

The largest stable timestep is then inversely proportional to the size of the grid. If the grid must be refined to resolve the flow physics, then the stable timestep is correspondingly reduced. The computational cost is therefore increased due to both the larger grid size and the requirement of more timesteps to span the same amount of physical time. For many cases, including the present work, this computational overhead is far too great, and a method which can take larger timesteps must be used.

4.3.2 Implicit Time Integration

Implicit time integration schemes do not have the limitation on timesteps for numerical stability like explicit schemes do. An implicit representation of Equation 4.41 is

$$\delta U^n = -\frac{\Delta t}{V} \sum_{faces} F'^{n+1} S \tag{4.44}$$

where $\delta U^n = \bar{U}^{n+1} - \bar{U}^n$ and F' is now being evaluated at $n+1$. A method is needed for evaluating F'^{n+1}, and this is done by again considering the inviscid and viscous components separately.

4.3.3 Inviscid Fluxes

The inviscid flux at time level $n+1$ can be linearized about the vector of conserved variables as

$$F'^{n+1} = F'^{n} + \left.\frac{\partial F'}{\partial U}\right|_n \delta U^n + \mathcal{O}\left(\Delta t\right) \tag{4.45}$$

where $\left.\frac{\partial F'}{\partial U}\right|_n$ is recognized as the flux Jacobian A' at time level n. This flux linearization can be split in the same way the MSW fluxes are split. For instance, the flux at face

$i + 1/2$ would be

$$F_i'^{n+} = A'^n_{+,i+1/2} U^n_i + A'^n_{-,i+1/2} U^n_{i+1} + A'^n_{+,i+1/2} \delta U^n_i + A'^n_{-,i+1/2} \delta U^n_{i+1} \tag{4.46}$$

Substituting this linearization into Equation 4.44 and reorganizing yields

$$\delta U^n + \frac{\Delta t}{V} \sum_{faces} A'^n S \delta U^n_f = -\frac{\Delta t}{V} \sum_{faces} F'^n S \tag{4.47}$$

where δU^n_f represents the appropriate δU^n to use when evaluating the split fluxes. This equation is an implicit method for solving the inviscid governing equations (the Euler equations) with first order accuracy in time. It must be solved simultaneously for all grid cells. If δU^n is stacked into a long vector, then the problem looks like a matrix multiplying that vector which is equal to a right hand side. The matrix consists of seven block diagonals where the rest of the elements are zero, resulting in a very sparse form. The non–zero elements of the matrix operator consist of flux Jacobians at the current time level n, and the right hand side is equal to the update as evaluated using the explicit Euler method. The matrix system could be solved with a simple matrix inversion, but this would be computationally infeasible. A method which minimizes storage requirements and computational expense must be used.

A property of the flow physics is used to provide a better means of solving this system. The boundary layer contains fluid that is experiencing high shear, and thus gradients normal to the wall are much greater than gradients tangent to the wall. It follows that the fluxes in the wall–normal direction will then be much larger than wall–tangent fluxes. Grid cells near the wall also tend to have high aspect ratios, with the larger faces having a surface normal similar in direction to that of the wall. This means that the solution in this region has much stronger coupling in the wall normal direction. This can be taken advantage of when solving the system.

Consider a two–dimensional flow. For a grid with quadrilateral cells, Equation 4.47 at cell (i, j) looks like

$$\hat{A}_{i,j} \delta U^n_{i,j} + \hat{B}_{i,j} \delta U^n_{i,j+1} + \hat{C}_{i,j} \delta U^n_{i,j-1} + \hat{D}_{i,j} \delta U^n_{i+1,j} + \hat{E}_{i,j} \delta U^n_{i-1,j} = \Delta U^n_{i,j} \tag{4.48}$$

where $\Delta U^n_{i,j}$ is the explicit update to the cell, and

$$\hat{A}_{i,j} = I + \frac{\Delta t}{V_{i,j}} \left(A'_{+,i,j} S_{i+1/2,j} + A'_{+,i,j} S_{i,j+1/2} - A'_{-,i,j} S_{i-1/2,j} - A'_{-,i,j} S_{i,j-1/2} \right) \quad (4.49)$$

$$\hat{B}_{i,j} = \frac{\Delta t}{V_{i,j}} \left(A'_{-,i,j+1} S_{i,j+1/2} \right) \quad (4.50)$$

$$\hat{C}_{i,j} = -\frac{\Delta t}{V_{i,j}} \left(A'_{+,i,j-1} S_{i,j-1/2} \right) \quad (4.51)$$

$$\hat{D}_{i,j} = \frac{\Delta t}{V_{i,j}} \left(A'_{-,i+1,j} S_{i+1/2,j} \right) \quad (4.52)$$

$$\hat{E}_{i,j} = -\frac{\Delta t}{V_{i,j}} \left(A'_{+,i-1,j} S_{i+1/2,j} \right) \quad (4.53)$$

The implicit matrix system then looks like

$$\begin{bmatrix} & & & & & & & & & \\ \ddots & & \ddots & \ddots & \ddots & & \ddots & & & \\ & \hat{E}_{i,j} & & \hat{C}_{i,j} & \hat{A}_{i,j} & \hat{B}_{i,j} & & \hat{D}_{i,j} & & \\ & & \ddots & & \ddots & \ddots & \ddots & & \ddots & \\ & & & & & & & & & \end{bmatrix} \begin{bmatrix} \delta U_{1,1} \\ \vdots \\ \delta U_{i,j} \\ \vdots \\ \delta U_{N_i,N_j} \end{bmatrix}^n = \begin{bmatrix} \Delta U_{1,1} \\ \vdots \\ \Delta U_{i,j} \\ \vdots \\ \Delta U_{N_i,N_j} \end{bmatrix}^n \quad (4.54)$$

Here, the block diagonals are represented by dots while all other entries in the matrix are zero. N_i and N_j are the total number of cells in the i and j directions, respectively. If a line of cells growing out from the wall is at a constant value of i, then the coefficients $\hat{D}_{ij}$ and $\hat{E}_{ij}$ contain cell information lying outside of this line. Utilizing the physical coupling in the solution, these two terms are relaxed to the right hand side. This results in an easier system to solve, and an iterative procedure is used to add back in the effect of the relaxed terms. Each iteration k is solved for as

$$\hat{A}_{i,j} \delta U^{(k)}_{i,j} + \hat{B}_{i,j} \delta U^{(k)}_{i,j+1} + \hat{C}_{i,j} \delta U^{(k)}_{i,j-1} = \Delta U^n_{i,j} - \hat{D}_{i,j} \delta U^{(k-1)}_{i+1,j} - \hat{E}_{i,j} \delta U^{(k-1)}_{i-1,j}. \quad (4.55)$$

This is a block tridiagonal system, and can be solved relatively efficiently with an LU decomposition method. The initial value is set as $\delta U^{(0)} = 0$, and then the update is iterated until it is sufficiently converged. If the flow solution is steady, then the update

only needs to be converged enough to be numerically stable for time–stepping to the final solution. A common number to use is $kmax = 4$, although this may need to be changed on a case–to–case basis. Once $kmax$ is reached, the update is set to $\delta U^n = \delta U^{(kmax)}$.

The method described above is known as a line relaxation method. It is similar to a Jacobi method in that it only uses information from the previous iteration, which lends itself to parallel computing. A drawback of the method is that solving along lines tends to bias the solution in that direction. This can be a problem if the flow is unsteady and time accuracy is important, in which case care must be taken to quantify the amount of bias. The timestep or $kmax$ could be changed to limit this error. Alternatively, a point relaxation method can be used which relaxes all terms except the $\hat{A}_{i,j}$ term to the right hand side. This eliminates the line biasing, but it is less stable and takes longer to converge.

4.3.4 Viscous Fluxes

The viscous fluxes also require a linearization about the state vector, but we do not have the viscous Jacobians and so something else must be done. The form of the viscous flux can be simplified by neglecting derivatives that are not in the wall normal direction since their values are small. This allows the flux to be written as

$$F'_{visc} = M\frac{\partial}{\partial \eta}V, \tag{4.56}$$

where M is a function of the transport properties and grid metrics, V is the vector of primitive variables, and η is the wall normal direction. The change in the viscous flux due to a change in the state vector can then be written as

$$\delta F'_{visc} = M\frac{\partial}{\partial \eta}\left(\frac{\partial V}{\partial U}\delta U\right). \tag{4.57}$$

For a complete treatment of the viscous fluxes, see Nompelis[82].

4.3.5 Higher Order Methods

Various methods use additional time levels or slope approximations to achieve higher order temporal accuracy. This work uses a second order Crank–Nicolson scheme, which

can be thought of as the combination of the forward Euler and backward Euler time discretizations. The Crank–Nicolson scheme is

$$\delta U^n = -\frac{1}{2}\frac{\Delta t}{V}\left(\sum_{faces} F'^n S + \sum_{faces} F'^{n+1} S\right), \tag{4.58}$$

and is second order in time. This implicit scheme is solved using the line relaxation method described above. While the line biasing exists in this scheme, using Crank–Nicolson in this work is acceptable since the flowfields are steady where crossflow instability is important, and hence the biasing should play an insignificant role.

4.4 Boundary Conditions

In order to solve the governing equations in a computational domain, appropriate boundary conditions must be implemented. This is done in the finite volume method by adding an additional layer of cells around the boundaries, referred to as ghost cells, which are then set with the appropriate conserved variables to enforce the desired boundary conditions. First, the implementation of the boundary conditions is explained, followed by the method of including them in the implicit operator.

4.4.1 Explicit Boundary Conditions

The values in the ghost cells must be set considering the corresponding interior cell, such that the correct condition is imposed at the face between them (the boundary). The boundary conditions used in this work are enumerated below.

No–Slip Wall

A standard physical wall obeys the no–slip condition and is impermeable, which requires the flow velocity to be zero at the wall. If the flow velocity is decomposed into a component tangential to the wall u_t and a component normal to the wall u_n, then the appropriate values for the velocity of the ghost cell are

$$u_{t,ghost} = -u_{t,interior},$$
$$u_{n,ghost} = -u_{n,interior}.$$

Symmetry

A symmetry (or slip wall) boundary condition which is impermeable only requires that fluid does not penetrate the surface, i.e. u_n at the face is equal to zero, giving

$$u_{t,ghost} = u_{t,interior},$$
$$u_{n,ghost} = -u_{n,interior}.$$

Pressure

Pressure at no–slip walls or symmetry conditions are set as

$$p_{ghost} = p_{interior}.$$

Isothermal Wall

An isothermal wall has a constant temperature T_w, which is a Dirichlet boundary condition. This is applied as

$$T_{ghost} = 2T_w - T_{interior}.$$

Supersonic Inflow

For a supersonic inflow, no flow characteristics are pointing out of the domain, which means that the inflow conditions are not dependent on the interior. In this case, ghost cells only need be set to the appropriate free stream conditions.

Supersonic Outflow

For a supersonic outflow, no flow characteristics are pointing into the interior, which means that the interior solution should not depend on the boundary values. Hence, ghost cells are set to the exact values of the interior.

4.4.2 Implicit Boundary Conditions

When using an implicit time integration scheme, solving with an implicit operator that only depends on the interior and then updating the boundary values explicitly can cause numerical instability. The ghost cells must instead be added into the implicit operator and solved along with the interior. Let the update to the ghost cells be related to the

interior cells by

$$\delta U_{ghost} = E\delta U_{interior}. \tag{4.59}$$

The matrix E must be determined for each ghost cell. The boundary conditions detailed in Section 4.4.1 are imposed on the primitive variables, meaning they are in the form of

$$\delta V_{ghost} = R\delta V_{interior}. \tag{4.60}$$

where R is known. We can transform this equation using $\delta U = \frac{\partial U}{\partial V}\delta V$ to get

$$\delta U_{ghost} = \frac{\partial U}{\partial V} R \frac{\partial V}{\partial U}\delta U_{interior}, \tag{4.61}$$

$$= E\delta U_{interior}. \tag{4.62}$$

This can be used to modify the implicit operator and add in the ghost cells. For instance, in a 2–D case the term for $\delta U_{N_i+1,j}$ (which is outside the domain) would become

$$\hat{D}_{i,j}\delta U_{N_i+1,j} = \hat{D}_{i,j}E\delta U_{N_i,j}. \tag{4.63}$$

Chapter 5

Problem Approach

5.1 Grid Construction

The flow domain for these simulations must be discretized into volumes for which the governing equations will be solved. This work uses a combination of the GridPro and Pointwise software suites to construct block–structured grids of the flow around the HIFiRE–5 forebody. While the flow solver treats the grid as unstructured, the structured topology of hexahedral cells provides advantages for aligning the grid to shocks (a necessary requirement) and appropriately resolving boundary layers.

The computational domain consists of one quarter of the HIFiRE–5 forebody. This domain was chosen to reduce computational cost, and the simplification is justifiable because of the symmetries present in the geometry. A rounded lip was added to the end of the geometry to expand the flow and prevent any subsonic character from traveling upstream. The boundary conditions consist of a velocity inlet surface which is contoured to the shock, a supersonic outflow at the aft of the ellipse–cone, a no–slip isothermal wall, and symmetry conditions at the centerline and attachment line. The symmetry condition at the centerline prevents any fluid from crossing this boundary, whereas in the real case the boundary layer plume which forms there most likely has unsteady fluid exchange across this plane. This is believed to have a minimal affect on the mid–span region of interest where crossflow instability dominates, and thus a symmetry condition should be a reasonable assumption. Further discussion of the boundary conditions are presented in Section 4.4.

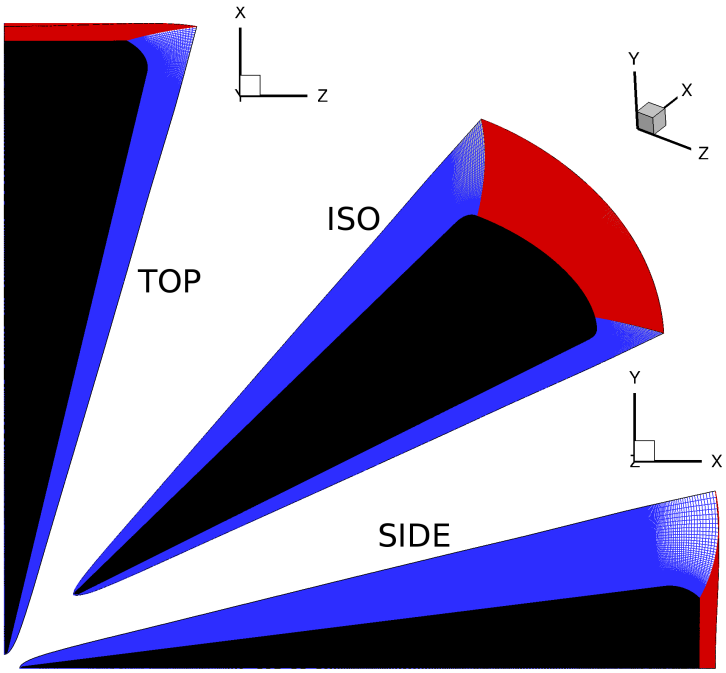

Figure 5.1: The computational flow domain.

The gridding process is started by creating a coarse grid which has boundaries sufficiently far from the geometry so as to include the bow shock in the domain. The shock envelope is an inviscid property and is purely a function of the geometry and Mach number of the flow. The shock surface is extracted from the coarse simulation by generating a point cloud from the points that contain a Mach number just under the free stream (in this case $M = 5.99$). This surface is then imported into CAD software, and a new inflow surface is constructed which is slightly offset from the shock. The new surface makes it easier to align the grid with the shock, which is done with a tailoring step during the simulation.

Next, a new grid topology is designed with the objective of creating a surface mesh which has relatively isotropic cell spacing and similar resolution across the majority of the forebody. Since the surface area of the cone increases with downstream distance, the topology requires singularities that allow the addition of grid cells in the streamwise direction. Singularities occur where a number of blocks other than eight meet at a grid node (a number other than four at a surface), and result in cell skewness which leads to

larger numerical error than a Cartesian grid. Initially, a topology was created with the singularities located along the attachment line. It was later found that these singularities were exciting crossflow disturbances, an unwanted result, therefore another topology was created with the singularities located close to the centerline. These topology approaches are shown in Figure 5.2. The effect of the location of the singularities is discussed in Appendix A.

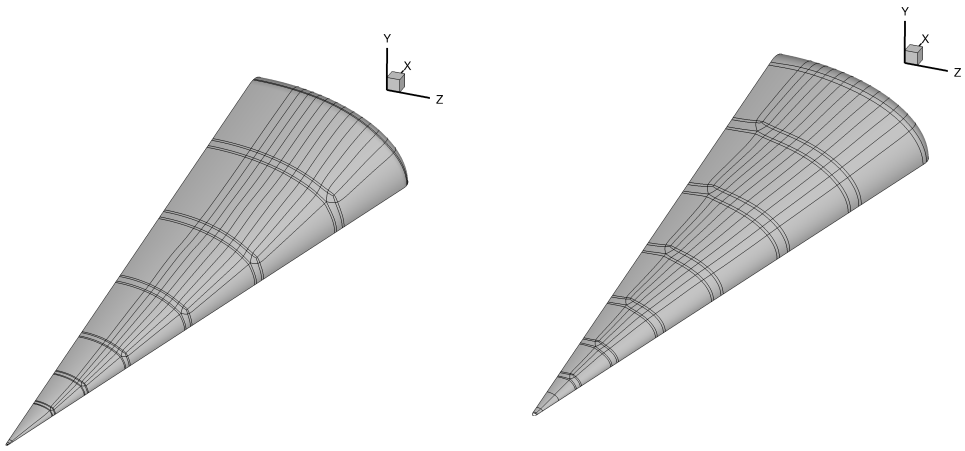

(a) The initial grid topology with singularities located near the attachment line.

(b) The final grid topology with singularities relocated to be near the centerline.

Figure 5.2: The DNS surface mesh topologies used to add cells in the streamwise direction.

Grid	**Total Cell Count**	**Size of Surface Mesh**	**Cells Wall–Normal**
Coarse	62,670,000	313,350	200
Medium	105,596,800	527,984	200
Fine	163,930,000	819,650	200

Table 5.1: Grid sizes and dimensions for each case.

Grids of several different sizes were generated to investigate convergence properties. Grid densities were only changed in the streamwise and azimuthal directions. Three grids were primarily used (referred to as coarse, medium, and fine) whose specifications are summarized in Table 5.1. The fine grid has approximately 15 cells per disturbance

wavelength.

Since the number of points in the wall–normal direction remained unchanged for all grids, care was taken to ensure adequate resolution in that direction. A total of 200 points were used in the wall–normal direction, with a vast majority of them located near the surface. The first cell height at the wall was set to 12 microns (excluding the nose region where it was necessarily smaller), which corresponds to a y^+ of roughly 0.1 for the low Reynolds number case and 0.2 for the high Reynolds number case. y^+ is a non–dimensional quantity defined as

$$y^+ = \frac{u_\tau y}{\nu}, \tag{5.1}$$

where y is the distance from the wall and ν is the kinematic viscosity. u_τ is the shear velocity, defined as

$$u_\tau = \sqrt{\frac{\tau_w}{\rho}}, \tag{5.2}$$

where τ_w is the wall shear stress. A common practice is to have y^+ less than one for proper resolution of the boundary layer.

Cell heights increase at a rate of 0.7% for the first 100 elements above the wall. This exceptionally small growth rate is used because a) the boundary layer is very thin near the attachment line and should be resolved by as many points as possible, and b) the small growth rate prevents grid waste outside of the area of interest close to the wall. This wall–normal spacing maximizes grid resolution in the areas of interest, and results in 90+ points in the boundary layer at mid–span, with cells at the boundary layer edge being roughly twice the height of the initial wall spacing.

Misalignment of the grid with shocks tends to create numerical error in those regions. Even though the initial grid is designed to follow the contour of the bow shock, further tailoring is needed to minimize this source of error. Grid tailoring is accomplished by moving a sheet of cell faces to lay tangent with the shock, so that locally the Rankine–Hugeniot relations describe the condition across each face. First, the flow solution is converged to the point that the bow shock has set up and is steady. The shock location is then detected by examining the density gradient magnitude near the inflow. A cell face is moved to this location, and a smoothing step is performed to ensure grid quality. Other faces must be moved accordingly so that the grid varies smoothly. Several options exist

in US3D to redistribute the faces from the wall to the shock by specifying a target y^+ or initial spacing, along with a hyperbolic tangent or geometric growth rate. However, extreme care was taken to design a wall–normal grid distribution for this particular case as described above, and so a redistribution is not desired. An additional option exists which simply scales the grid to move a face to the shock without redistributing. This method is used, but it requires knowledge of how much scaling is required so that the initial wall spacing can be set. The initial spacing must be set such that after the scaling is done, the new spacing is 12 microns as desired. This had to be done manually by trial and error.

5.2 Addition of Roughness

After a baseflow is computed on an initial grid, roughness is added to provide a forcing for disturbances. Past work has generally relied on discrete roughness elements (DREs) to trip the flow, using a spacing pattern which forces a particular wavenumber. While the DRE approach may be suitable for simulating the effects of specific features like bolts and rivets, it is less suitable for simulating smooth–body transition where the geometry is free of defects and has a fine finish. This is because a) DREs create a disturbance spectrum which is unrealistically clean, b) the forced wavenumber will dominate the disturbance field even if it is not the most unstable wavenumber, and c) disturbances are anchored behind the roughness elements and cannot move to where they would otherwise more naturally occur.

Gronvall et al.[47] used a technique of generating a distributed roughness patch which was then digitally filtered to contain a dominant wavelength which was close to the most unstable wavelength. The result was a more chaotic disturbance pattern which more closely resembled smooth–body transition.

The present work is intended to simulate the conditions of smooth–body transition by forcing the smallest wavenumber possible. This is done by perturbing each node on the wall by a small random distance, with the nodes above being perturbed by the same distance with a *tanh* fall–off. Different maximum roughness heights are used depending on the case, the very largest being 4μm. Conceptually, crossflow disturbances which are excited by this type of roughness should primarily contain the natural, flow–selected,

most unstable wavenumber.

There are several items to note about this roughness method.

1. The roughness is point–to–point on the computational grid. This means that the grid is forcing all wavenumbers up to the highest wavenumber possible, similar to a Nyquist frequency. It also means that the highest wavenumber being forced will depend on the density of the surface mesh. Grid cells are smaller at the nose and experience some stretching in the streamwise direction, therefore the forcing content of the roughness is dependent on the local grid and the forcing is not isotropic in general.

2. Roughness heights are determined by sampling from a uniform distribution, and the roughness is applied to the entire surface of the geometry.

3. Grid density changes from case to case for grid convergence studies. Increasing the grid density will then increase the highest forced wavenumber, and the forcing content will change when otherwise trying to converge the solution, an unwanted result.

4. The height of the roughness is much less than the height of the cell on the wall. The roughness is therefore not grid resolved in this direction. Rather, the roughness can be thought of as a perturbation of the face normals on the wall which produce small fluctuations in velocity that are orthogonal to the otherwise flat wall.

5. In consideration of Item 4, wall faces of different size which have their nodes displaced by the same amounts will have their face normals perturbed to different angles. Specifically, the smaller the cell is, the larger the angle between the original face normal and the perturbed normal will be. Hence, finer grids can have larger forcing for the same maximum roughness height.

6. Since the roughness is point–to–point and less than a grid cell tall at its maximum, the smallest fluid fluctuations associated with the roughness scales are not properly resolved by the DNS grid. In other words, the present work does not attempt to accurately capture the receptivity process.

7. Due to the previous three points, grid roughness of a certain height can not be expected to produce the same initial disturbances as physical roughnesses of the same height.

Some of these characteristics of the roughness, especially Item 3, could be considered limitations on the usefulness of this approach. Care must be taken to quantify these effects.

Figure 5.3 shows the smallest forced wavelength along the attachment line for each grid, λ_{grid}. This can also be thought of as twice the local cell width (λ_{grid} is calculated as the square root of the surface face area). The figure demonstrates that the smallest forced wavelength becomes larger due to grid stretching in the streamwise direction. The humps are present because of small variations in the grid density due to the topology around singularities. These humps would presumably disappear if the grids were smoothed for longer, but additional smoothing stretches the grid around the singularities unfavorably. These density variations are not visible to the naked eye and are not believed to have an effect on the solution.

For grid convergence purposes and to establish a baseline, a tool was created to interpolate the roughness of a coarse grid onto finer grids. This is shown conceptually in Figure 5.4. The roughness interpolation allows a grid convergence study while keeping the roughness as unchanged as possible. This ability proves extremely useful and helps convey several important results discussed in Chapter 6.

5.3 Flow Solver

The flow solver used for this work is US3D[83], an unstructured finite–volume Navier Stokes code developed at the University of Minnesota. The code is an implementation of the data–parallel line relaxation method, and was designed with scalability and parallel performance in mind, making it ideal for the present work. US3D has many other features, such as finite–rate thermochemistry, which are not used here.

Computations are run on ∼1000 cores for the larger cases with implicit timesteps resulting in convergence in 3—5 days. All calculations use sixth order accurate KEC fluxes and second order accurate Crank–Nicholson line relaxation unless otherwise noted. These numerics are discussed in Chapter 4.

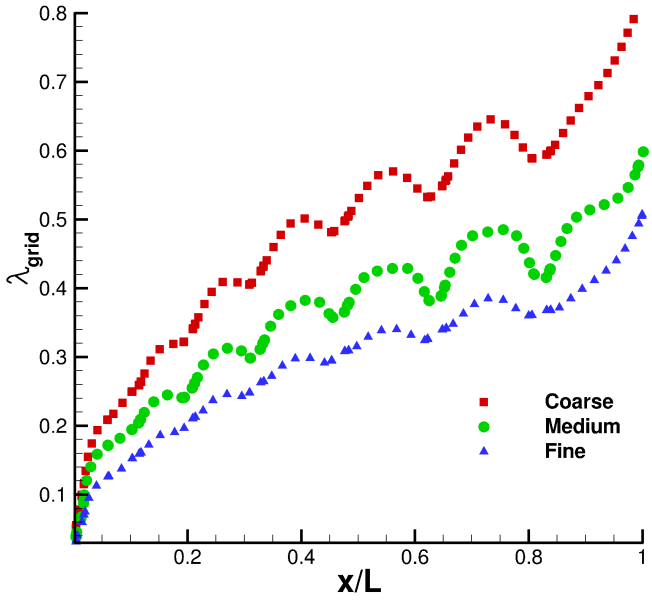

Figure 5.3: Smallest forced wavelength (in mm) along the attachment line for each grid. λ_{grid} is calculated as the square root of the surface face area.

5.4 Baseflow Computation

Fluid flowfields can be decomposed into an undisturbed laminar state and a disturbance field. The former is often referred to as a basic state or baseflow. Numerical calculation of the disturbance field requires the computation of both the disturbed flow and the baseflow, with the disturbance field being the difference between the two. Since analysis of disturbance character (shape, growth, etc.) is fundamental to this work, baseflow calculations are imperative. Due to the extreme sensitivity of crossflow instability, care must be taken to ensure that disturbances are not excited in the baseflow calculation. This can prove difficult if inappropriate grid topologies or numerics are used.

While a baseflow need not be the time–averaged flowfield, the laminar flow over the forebody of HIFiRE–5 is steady and so the baseflow and the mean flow are equivalent. For each flow case in this work a baseflow is first computed. This is done by running each nominal grid before roughness is added with second order Modified Steger-Warming fluxes and first order line relaxation for time integration. The dissipation of these

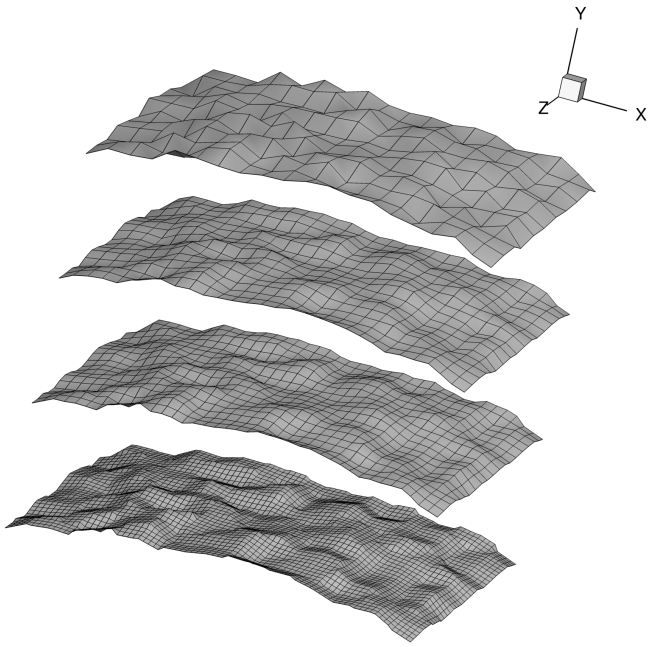

Figure 5.4: The verification case for the roughness interpolation, which shows how coarse roughness is interpolated onto finer grids.

numerics help suppress any disturbance growth and encourage a clean solution, while still properly resolving the boundary layer.

Condition	$\boldsymbol{Re}$	$\boldsymbol{U_\infty}$	$\boldsymbol{\rho_\infty}$	$\boldsymbol{T_\infty}$	$\boldsymbol{p_{stag}}$	$\boldsymbol{T_{stag}}$
High	11.8×10^6 /m	869.7 m/s	4.6×10^{-2} kg/m^3	52.3 K	1090 kPa	429 K
Low	8.1×10^6 /m	850.5 m/s	3.0×10^{-2} kg/m^3	50.0 K	688.9 kPa	410 K

Table 5.2: Mach 6 free stream conditions of the tunnel used for computations.

Chapter 6

Results

In this chapter, the salient results of this work are discussed. Additional results which discuss the development of this research and other intermediate results are provided in Appendix A. Note that several contour plots of surface quantities in this chapter are mirrored across the centerline only to provide intuition and to orient the reader. The terms "DNS solution" and "disturbed solution" refer to cases which include roughness, while the terms "baseflow" and "basic state" are interchangeable. All computational cases presented in this chapter are summarized in Table 6.1.

6.1 Baseflow Solutions

Baseflows were computed for the grid and Reynolds number of each case, which provide a description of the general flowfield of HIFiRE–5. The asymmetry of the geometry causes the resulting shock surface to have different oblique angles along the minor axis (the centerline) and the major axis (the attachment line). This asymmetry induces a pressure gradient which transports fluid from the attachment line towards the centerline, causing the boundary layer to become very thin at the attachment line. The boundary layer thickens towards the centerline, where the fluid plumes and a counter–rotating vortex pair forms.

Case	***Re***	**Grid**	**Roughness**	**Notes**
1	Low	Coarse	None	Baseflow calculation
2	Low	Medium	None	Baseflow calculation
3	Low	Fine	None	Baseflow calculation
4	High	Fine	None	Baseflow calculation
5	Low	Coarse	$2\mu m$ Coarse	
6	Low	Coarse	$2\mu m$ Coarse	Rerandomized roughness pattern
7	Low	Medium	$2\mu m$ Medium	
8	Low	Fine	$2\mu m$ Fine	
9	Low	Medium	$2\mu m$ Coarse	
10	Low	Fine	$2\mu m$ Coarse	
11	High	Fine	$2\mu m$ Coarse	
12	High	Fine	$1/2\mu m$ Coarse	
13	High	Fine	$4\mu m$ Coarse	
14	High	Medium	None	Baseflow, Sharp nose
15	High	Medium	$2\mu m$ Medium	Sharp nose

Table 6.1: List of cases presented in Chapter 6.

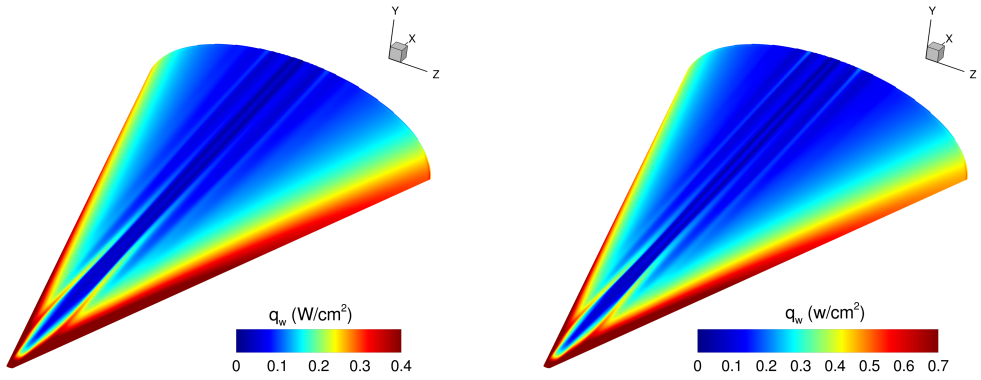

(a) Low *Re* (b) High *Re*

Figure 6.1: Baseflow surface heat flux.

Figure 6.1 shows contours of the baseflow wall heat flux. Heating is significantly higher near the attachment line where the boundary layer is thin, and a streak of high heating forms near the centerline corresponding roughly to the edge of the boundary layer plume and subsequent downstream vortex. Note that several surface contour plots in this section mirror the solution about the centerline to orient the reader and aid intuition. The boundary layer plume is depicted by streamwise crosscuts of density in Figure 6.2. Once the primary centerline vortex has sufficiently rolled up, the downward motion "pinches" the boundary layer and spawns another vortex, which can in turn lead to additional vortices by the same mechanism. The development of this centerline vortex system increases with Reynolds number or nose sharpness, and is a property of the basic state. These vortices should not be confused with those generated by crossflow instability, although the two can interact.

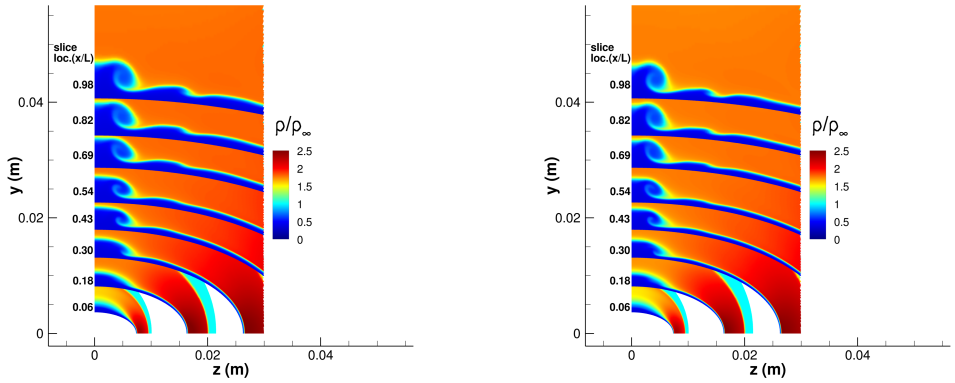

(a) Low Re (b) High Re

Figure 6.2: Streamwise baseflow crosscuts of density at several axial locations.

Figure 6.3 shows contours of the maximum in the crossflow velocity magnitude over the entire surface. A large swath in the midspan region of the geometry reaches approximately 8% of the free stream velocity, and this is the region where crossflow instability is expected to dominate. Crossflow magnitudes on HIFiRE–5 are similar to what is seen on the 7° half–angle cone at 6° angle of attack. While crossflow dominates the midspan region, second modes are expected to dominate at the centerline and attachment line.

Figure 6.4 shows density contours in different slices for the baseflow at both Reynolds

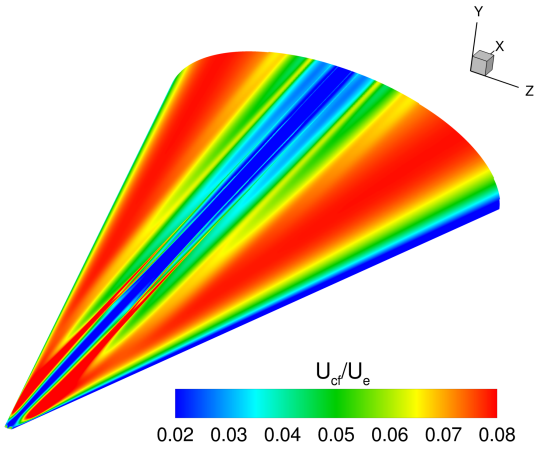

Figure 6.3: Crossflow velocity magnitude normalized by local edge conditions.

numbers. The figure displays the proximity of the inflow to the shock surface and demonstrates that the inflow closely follows the contour of the shock; this is the outcome of the grid tailoring process. The result is a very sharp shock surface, which is critical for minimizing numerical error in this region.

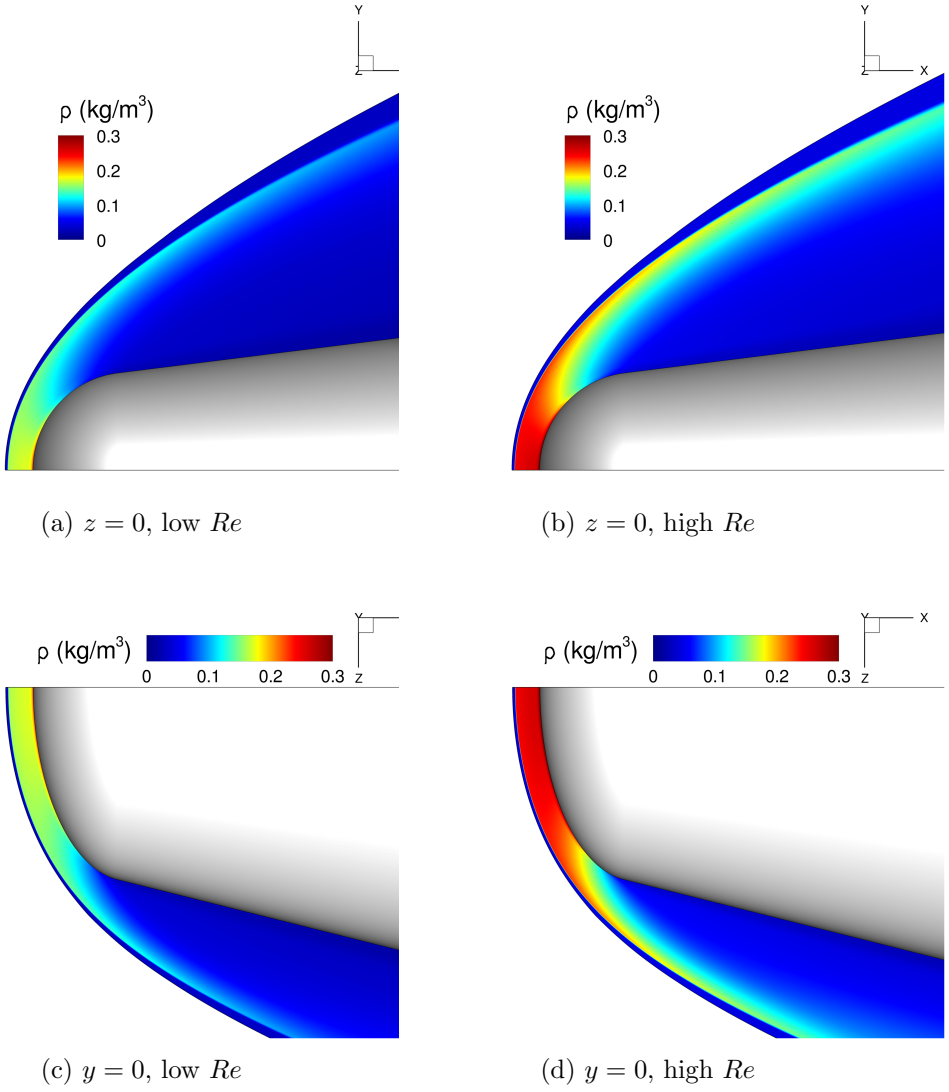

(a) $z = 0$, low Re

(b) $z = 0$, high Re

(c) $y = 0$, low Re

(d) $y = 0$, high Re

Figure 6.4: Density contours of baseflow near bowshock region.

6.2 Roughness Characterization

Several cases were run at the low Reynolds number condition to characterize how applying point–to–point roughness affects the resulting flowfield. A maximum roughness height of 2 microns is applied to the coarse, medium and fine grids, resulting in a coarse, medium, and fine roughness, respectively. While the wall heat flux is a good indicator for establishing the position of crossflow disturbances, at low Re the disturbances are small and the signatures in the total heat flux are weak, as shown by Figure 6.5.

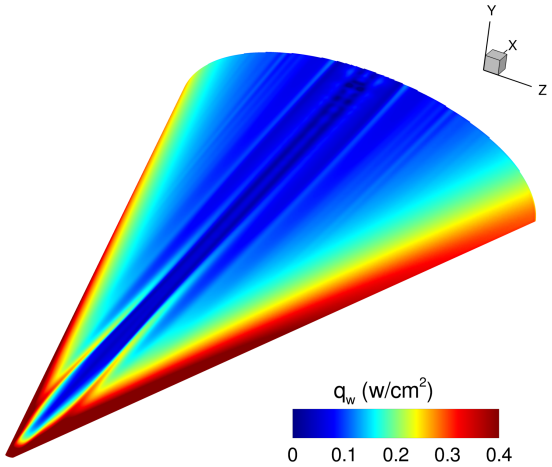

Figure 6.5: Surface heat flux contours for the low Re condition and 2 micron roughness.

The disturbance heat flux is calculated by subtracting the baseflow heat flux from the DNS solution, and is depicted for several cases in Figures 6.6 and 6.7. Visualization of the disturbance heat flux makes the presence of crossflow disturbances readily evident. Here, white streaks represent positive q'_w and dark streaks represent negative q'_w, and each disturbance is affiliated with a white–dark pair. Unsteady disturbances propagate downstream near the centerline in a corridor that is bounded by the large vortex that is second from the centerline, but outside of this corridor the flowfield is steady. Figure 6.6 shows that the disturbances of each roughness pattern have qualitative similarities, but the heating patterns are different; disturbances vary in position and strength from case to case. If the same coarse roughness is instead interpolated onto each grid, the

patterns become much more similar, as shown in Figure 6.7.

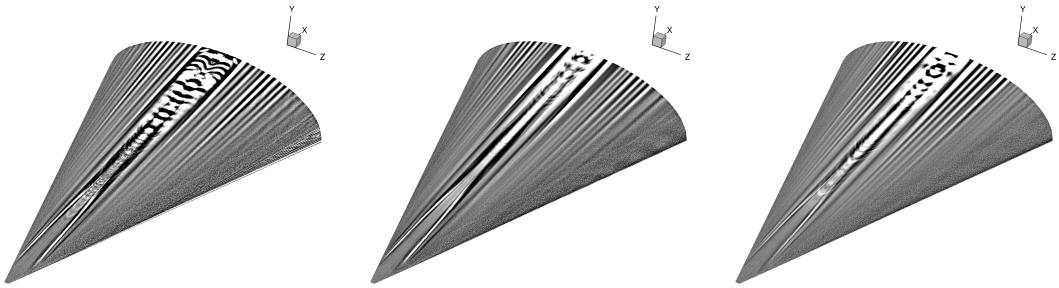

(a) Coarse–Coarse (b) Medium–Medium (c) Fine–Fine

Figure 6.6: Disturbance wall heat flux for each grid. Captions read as (Grid–Roughness).

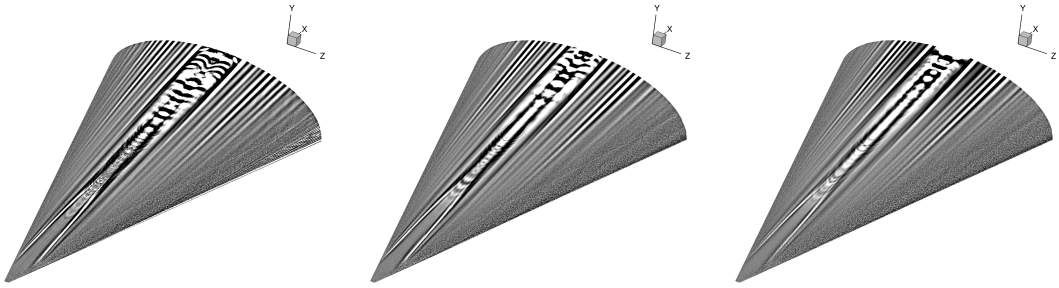

(a) Coarse–Coarse (b) Medium–Coarse (c) Fine–Coarse

Figure 6.7: Disturbance wall heat flux for each grid, with the coarse roughness interpolated onto each. Captions read as (Grid–Roughness).

Figure 6.8 compares wall heating vs. spanwise coordinate for each case at $x/L = 0.95$, and clearly demonstrates the importance of the initial conditions provided by the roughness. When the coarse, medium, and fine roughness are used as in Figure 6.8a, each case shares a peak just inward of $z = 2$ cm, which corresponds to a vortex that is part of the baseflow centerline vortex system. Outward of this peak however, the disturbances have similar amplitude and wavelength, but do not overlay each other. In other words, the roughness seems to be responsible for the phase of the disturbances, but not the spectral content. When the grids are interpolated to have the same roughness distribution, as in Figure 6.8b, the disturbances now overlay each other and show excellent

agreement. This demonstrates a level of grid convergence and also shows that the exact solution is very sensitive to the initial conditions provided by a particular roughness pattern. To further stress the importance of the roughness, Figure 6.8c compares two cases using the coarse grid, with one case using the original coarse roughness and a second case re–randomizing the roughness heights. We again see that while the amplitudes and wavenumbers of the disturbances are similar, the patterns do not overlap.

The extreme sensitivity to roughness in these simulations is also seen in experiment. Test articles with a fine finish exhibit repeatability from run to run in the resultant heating patterns. The patterns are jagged and differ from one side of the article to the other, and these differences are believed to come from the fine scale roughness. Due to this sensitivity, we cannot expect a computation to produce exactly the same solution as a tunnel experiment.

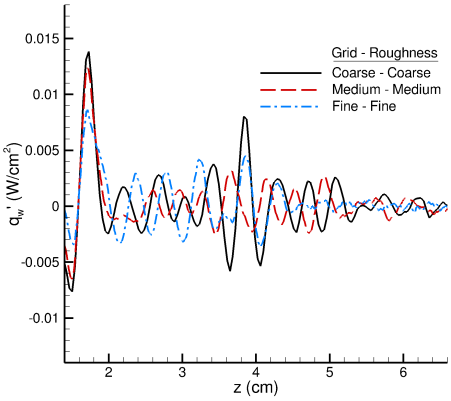

(a) All three grids with their respective roughnesses.

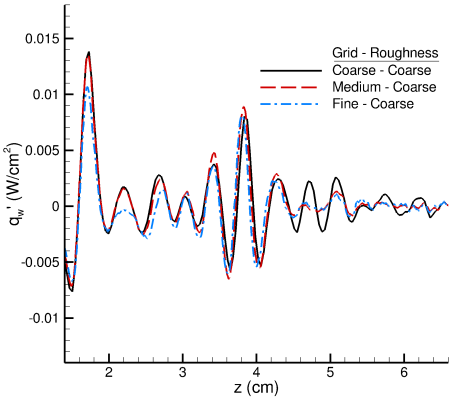

(b) All three grids with the coarse roughness interpolated onto each.

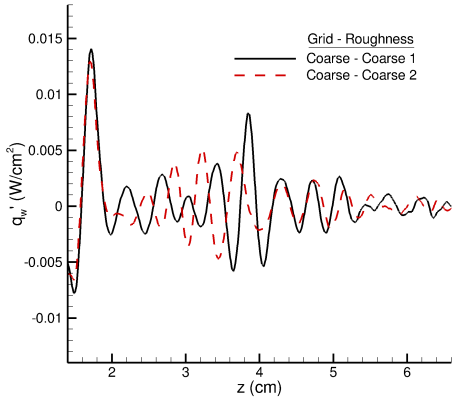

(c) Coarse grid–Coarse roughness, 2 different random roughness patterns.

Figure 6.8: Disturbance heat flux vs. spanwise coordinate at $x/L = 0.95$ for several cases.

6.3 Analysis of Disturbances at High Re

Increasing the Reynolds number leads to a dramatic change in the resulting heating pattern. Disturbances grow large enough that their heat flux signatures are easily visible. All results at the high Reynolds number condition use the fine grid with coarse roughness.

At this higher Reynolds number condition, the flow is more sensitive to acoustic disturbances. Low amplitude numerical noise generated in the subsonic region is amplified downstream and interferes with the formation of the stationary crossflow vortices. Using a second order KEC scheme instead of sixth order KEC for the high Re condition mitigates this numerical effect. Further discussion of this numerical noise can be found in Appendix A.

Figure 6.9 shows contours of wall heat flux for the case with 2 μm roughness. We can immediately see the similarities between the simulation and experiment; streamwise streaks appear which have a sharp increase in heat flux followed by lower values downstream. Experimental TSP images have a certain degree of hysteresis and hence cannot specifically rule out if this phenomenon has steady or unsteady causes, yet the present computations are still all very steady in the midspan region which points to a steady source.

Explanation of these streaks of high heat flux requires examination of the flowfield. To do this, data are extracted from several flow slices normal to the streamwise direction as shown in Figure 6.10a. Velocities in these planes are decomposed into streamwise (edge direction), wall–normal, and crossflow components, and disturbance quantities are calculated by subtracting the basic state. Finally, these quantities are overlaid onto the heat flux contours in Figure 6.10b. This allows us to directly compare the heat flux with the behavior of the corresponding disturbance above it.

Figure 6.10c displays the heat flux in the region of interest. Notice that each heat flux streak seems to disappear at some axial location, followed by the appearance of a new streak immediately behind it and to the right. Even though these streamwise pairs of streaks might suggest there is a pair of disturbances involved, Figure 6.10d overlays the streamwise velocity component from the slices and shows that only one large vortex sits above each pair. In fact, the high heating streaks are due to the large

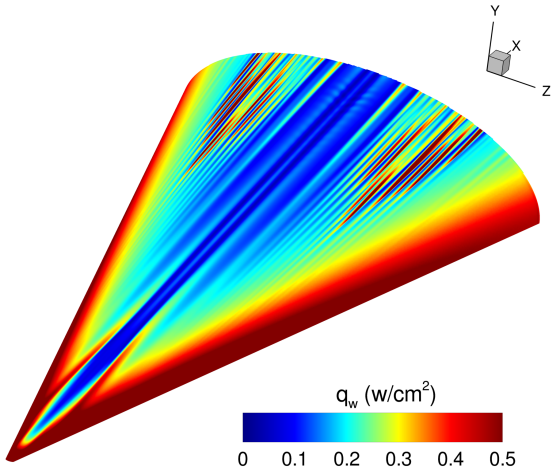

Figure 6.9: Wall heat flux for 2 μm roughness and high Re.

streamwise velocity disturbance that is generated by the vortical motion. The crossflow vortex brings low momentum fluid from deep in the boundary layer away from the wall on one side, and brings high momentum fluid closer to the wall on the other side. Figure 6.10e shows the evolution of this disturbance in streamwise velocity; initially, negative and positive disturbances alternating in the spanwise direction begin to grow at about the same height in the boundary layer (roughly 0.75 δ, which is where the generalized momentum inflection of the crossflow profile sits). Proceeding downstream, the disturbances grow to magnitudes as large as 60% of U_∞ as the positive disturbance is rotated toward the wall and the negative disturbance is rotated toward the top of the boundary layer in clockwise fashion. The sudden increase in wall heat flux corresponds with the large streamwise velocity disturbance impinging on the wall. The disturbance subsequently lifts off the wall as the vortex "turns over", resulting in a decrease in heat flux. Finally, the vortex reestablishes its presence in the heat flux as it continues to pull high speed fluid toward the wall. Figure 6.10f shows the wall–normal velocity component and the constant push–pull of each crossflow disturbance. This wall–normal component reaches maxima that are much smaller than the streamwise component, on the order 2–3%.

Slices of density are plotted for several axial locations in Figure 6.11, with the slices

flattened out so that it is simple to follow the evolution of each crossflow disturbance beginning at the bottom of the figure. Two disturbances near $z = 0.035$ m begin with higher initial amplitudes than the others, and consequently begin to roll up first. By $x/L = 0.81$, a high density core of fluid associated with the positive streamwise velocity disturbance is impinging on the wall. By $x/L = 0.87$, the core is moving away from the wall and the cresting vortex collapses on itself. Beyond $x/L = 0.92$, the disturbance regains its vortical shape and begins to roll up again.

This phenomenon of disturbance impingement on the wall does not appear to occur to the same degree for the 7° half–angle cone at 6° angle of attack. The DNS by Gronvall et al.[47] and the DNS using an azimuthal ray of DREs by Balakumar and Owens[45], both on the slender cone, do seem to contain streaks that have lower heating downstream, but the streaks are not as sharply contrasting as with HIFiRE–5 and so the phenomenon is not as obvious. One explanation for this difference is that disturbance paths on the slender cone contain significant streamwise curvature compared to HIFiRE–5, therefore vortices could be lifting off the wall far enough to mitigate the effects of the streamwise disturbance once it has rotated close enough to the wall. Regardless, it is reasonable to believe that this type of wall impingement can occur for a streamwise vortex generated in any manner.

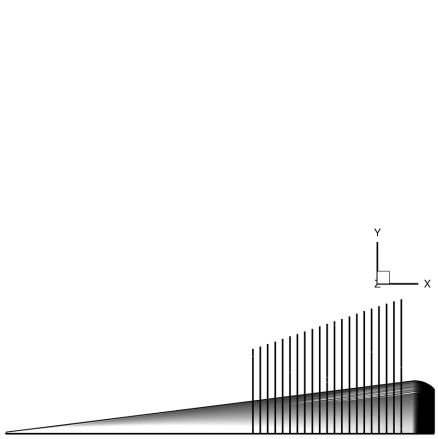

(a) Locations of streamwise crosscuts.

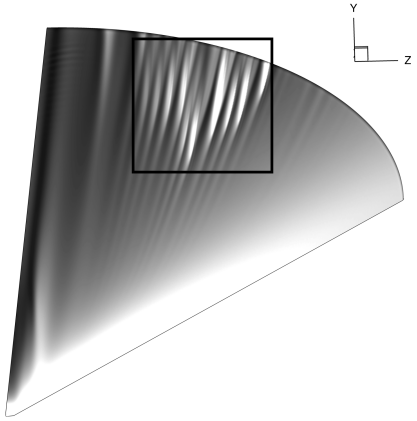

(b) Highlight of the plotting area.

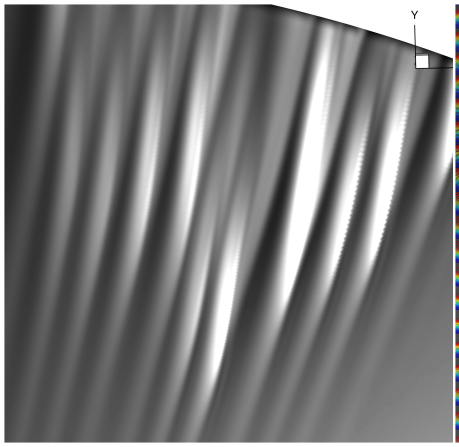

(c) Disturbance heat flux.

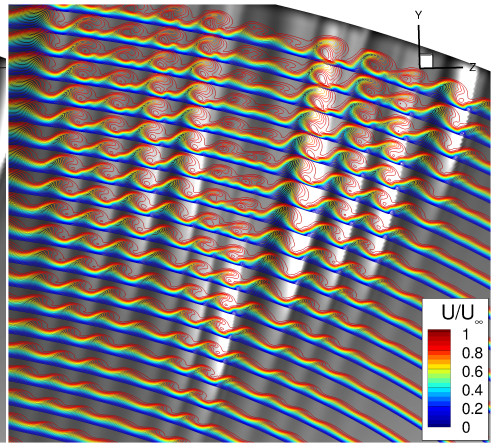

(d) Overlaid lines of streamwise velocity component.

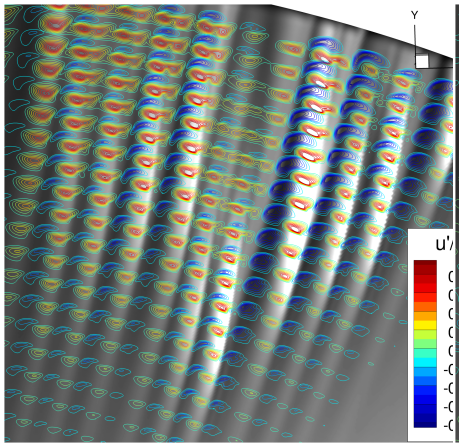

(e) Overlay of streamwise velocity disturbance.

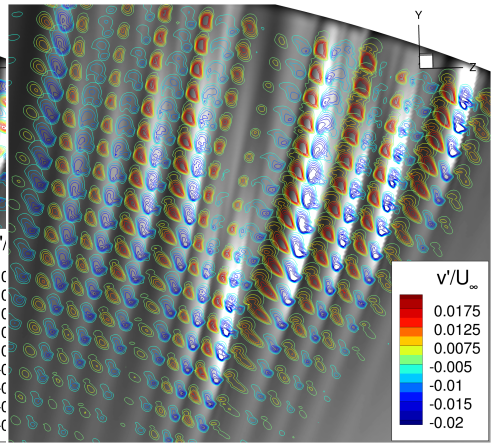

(f) Overlay of wall–normal velocity disturbance.

Figure 6.10: Quantities from streamwise crosscuts overlaid onto the surface heat flux.

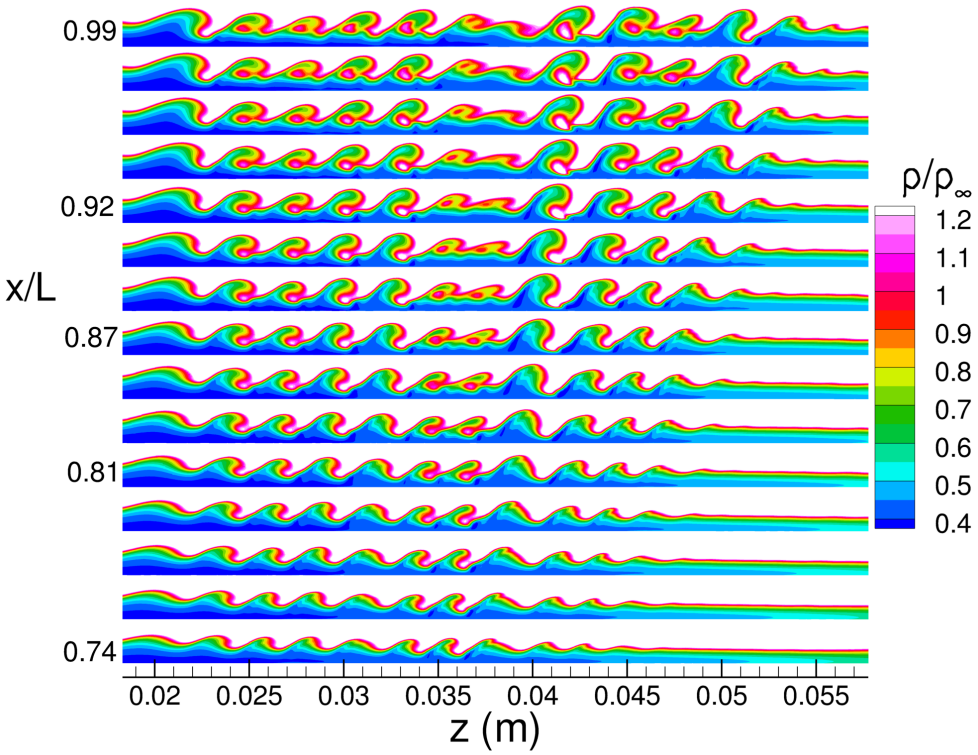

Figure 6.11: Contours of density from several axial locations unwrapped for the 2 μm case.

6.4 Effect of Roughness Height

For the high Reynolds number condition, two additional roughness heights were used to investigate the effect on the resulting disturbance amplitudes. Each roughness was generated by scaling the same roughness pattern, i.e., nodes were not re–randomized. This is important for isolating the effect of roughness height, considering the sensitivity to the roughness discussed in Section 6.2.

The two roughness heights that were run in addition to 2 μm were 0.5 and 4.0 μm. Figure 6.12 shows a close–up of the resulting heat flux patterns for each roughness from top down. We see immediately that the roughness height has a large impact on the resulting flow, with larger heights causing the heating pattern to move forward. Interestingly, the shape of the heating front caused by disturbance impingement changes drastically instead of just moving forward or backward on the geometry. The leading disturbance in the center of the midspan region only moves forward about 4 cm when changing the roughness from 0.5 to 4 μm, while some disturbances closer to the centerline move from near the end of the geometry to nearly flush with the leading disturbance, a jump of 10 cm. As the roughness height is increased, the shape of the heating front broadens as depicted in Figure 6.13. This shape change has a physical explanation which is discussed in Section 6.6.

While scaling the roughness height changes the shape of the heating front, it does not change the initial position of the disturbances. Figure 6.14 shows disturbance heat flux vs. spanwise coordinate for several axial locations. At $x/L = 0.72$ the disturbances from each roughness height perfectly overlap each other and only differ in magnitude. Proceeding downstream, as the disturbances impinge on the wall, the position of the disturbances shift and the heating pattern becomes incoherent. The maximum disturbance heat flux along each vortex is mostly independent of the roughness height.

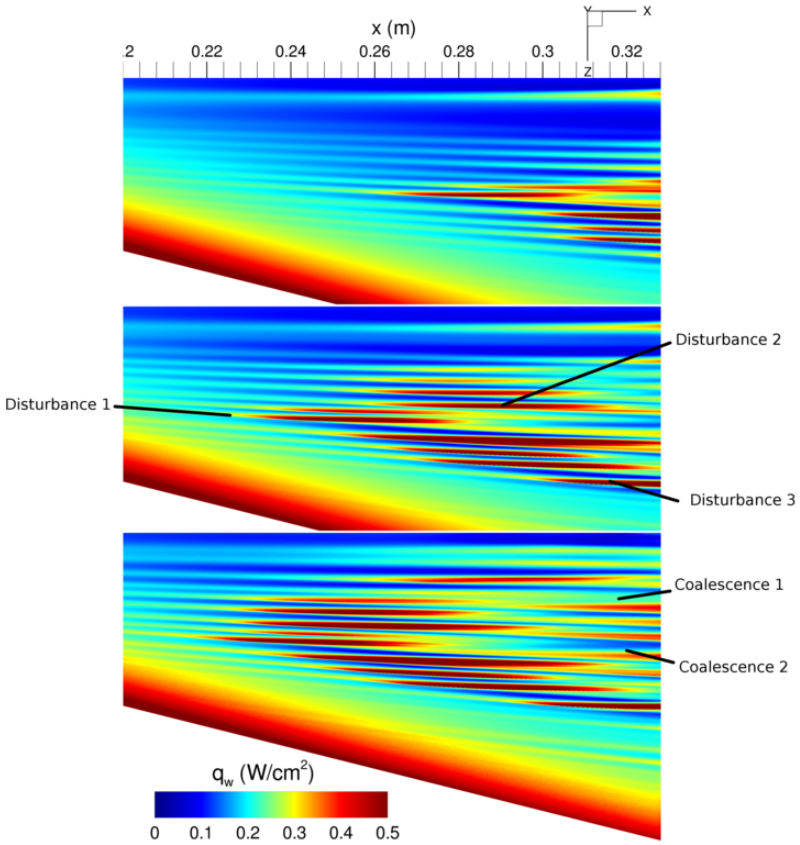

Figure 6.12: Wall heat flux contours for (from top to bottom) 0.5 μm, 2.0 μm, and 4.0 μm roughnesses.

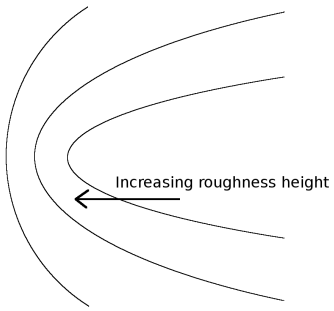

Figure 6.13: Illustration of change in heating front shape with roughness height.

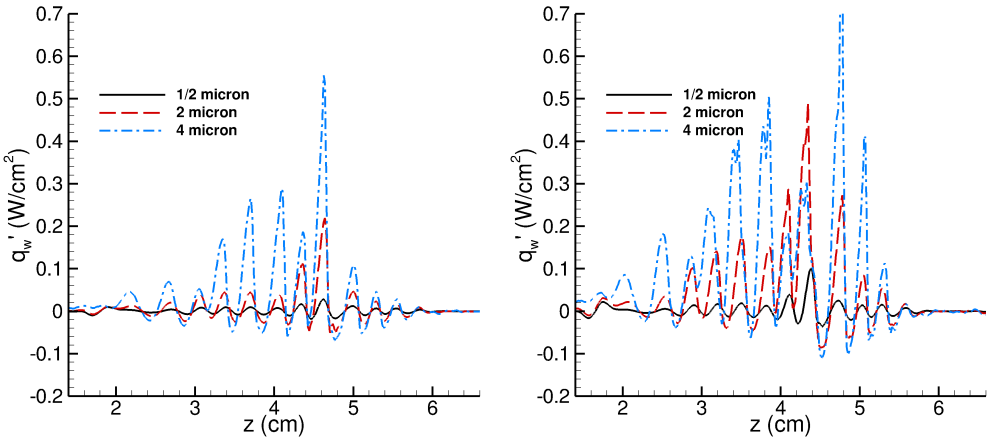

(a) $x/L = 0.72$

(b) $x/L = 0.79$

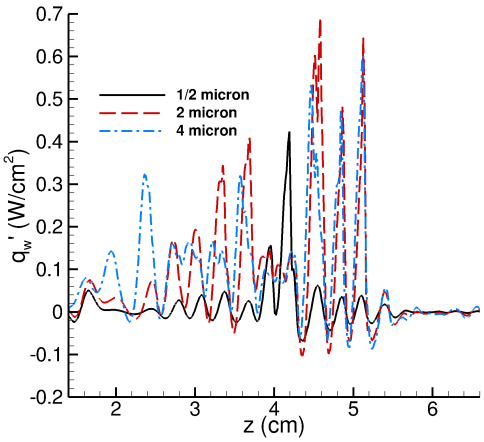

(c) $x/L = 0.87$

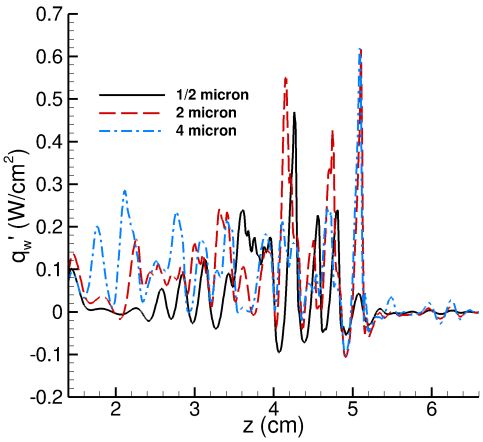

(d) $x/L = 0.95$

Figure 6.14: Disturbance heat flux vs. spanwise coordinate for different axial locations.

6.5 Evolution of Disturbance Wavelength

Disturbance wavelengths were computed for both Reynolds numbers and the different roughnesses used. Figure 6.15a shows an example of the disturbance paths extracted from the basic state overlaid onto the disturbance heat flux, showing excellent agreement. Local wavelengths are then found for every point along each path by finding the distance to its nearest neighbors. Figure 6.15b shows the disturbance wavelength vs. axial distance for nine traces from the coarse roughness case. Wavelengths evolve chaotically and a great deal of spreading occurs, with disturbances having a wavelength of less than 1 mm early on and growing to around 4 mm by the end of the geometry. It is important to note that ahead of $x/L = 0.2$, traces sit very near to the attachment line, and all of the traces occupy a small physical space. This overcrowding likely implies that crossflow disturbances have not actually been seeded at this point; nevertheless, disturbance paths can be extracted from the basic state and followed upstream ahead of where crossflow disturbances exist.

To get a sense of the flow behavior on the whole and to compare across cases, an average wavelength is computed. This is done by averaging the wavelengths of the five disturbances closest to the centerline (depicted by solid lines in Fig. 6.15b), and also by averaging the wavelength of every disturbance present, up to ten. These two averages are plotted for several cases in Figures 6.15c and 6.15d, respectively. Two averages are presented because a) the disturbances closer to the centerline are considerably stronger than those more outboard, b) the outboard disturbances have greater variation in wavelength and have perceived outliers, and c) the resulting average is sensitive to how and over which disturbances the average was taken.

Looking at Figures 6.15c and 6.15d, solid lines represent cases at the low Reynolds number condition with different roughnesses. For these cases, the resulting average wavelengths are very similar near the end of the geometry. In the instance of smooth body transition, we expect the resulting dominant disturbance wavelength to be independent of the roughness and instead a function of flowfield parameters (such as Reynolds number). It is difficult to ascertain the degree to which we have achieved this result here. A certain level of variability in the average wavelength is anticipated due to the random nature of the roughness, but it is uncertain how much variability

can be allowed before it must be attributed to a change in the characteristic forcing wavelength of the roughness. The two cases using coarse roughness (and hence the same characteristic forcing) but different randomized heights produce different heating patterns, yet their average wavelength is virtually the same. This seems to suggest that the medium and fine roughnesses are affecting the resulting disturbance wavelength, but we would intuitively expect finer roughness to produce smaller disturbance wavelengths, and this trend does not exist in the data. We conclude that at best, the variability in the average wavelength is due to random chance (therefore the flow–selected disturbance wavelength is appearing), and at worst the disturbance wavelength is weakly dependent on the forcing characteristics of the roughness. Nevertheless, Fourier spectra of oil flow intensity from experiment show peaks at 3.2 mm and 4.3 mm, and the wavelengths of these computations are in this regime.

The dotted line in Figures 6.15c and 6.15d represents the high Reynolds number case with coarse roughness. The resulting wavelength near the end of the geometry is much smaller than cases at low Re, demonstrating a clear dependence on Reynolds number which is much greater than any roughness dependence that is present. Experimental data show some shifting in the 3.2 mm and 4.3 mm peaks towards slightly smaller values for higher Reynolds number.

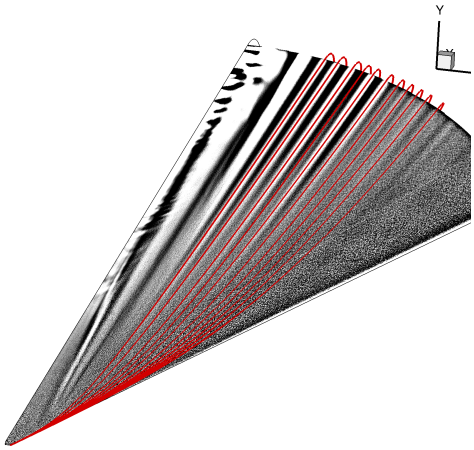

(a) An example of disturbance path extractions (in red) overlaid onto the disturbance wall heat flux.

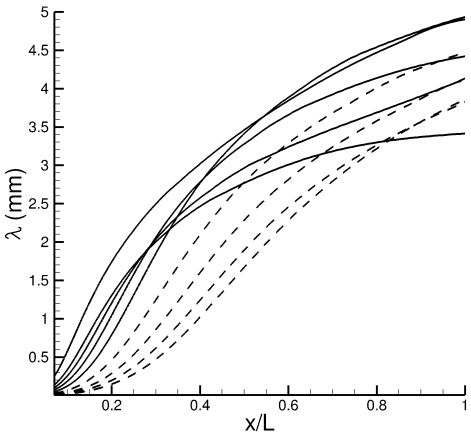

(b) Disturbance wavelengths vs. axial distance for nine traces extracted from a coarse roughness case.

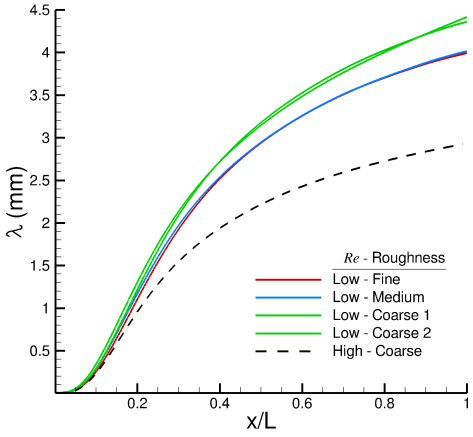

(c) Average disturbance wavelength vs. axial distance for several cases. Average is computed using only the disturbances close to the centerline, depicted as solid lines in Fig. 6.10d.

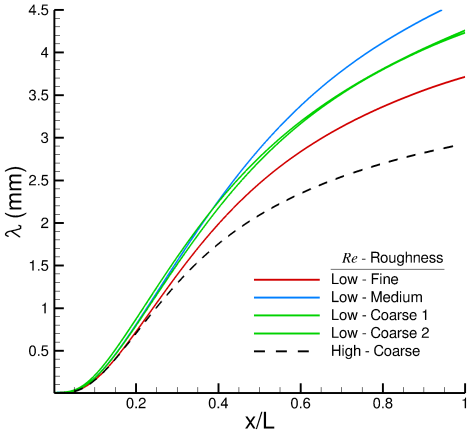

(d) Average disturbance wavelength vs. axial distance for several cases, with average computed using all of the disturbances depicted in Fig. 6.10d.

Figure 6.15: Wavelength evolutions computed with disturbance path extractions.

6.6 Disturbance Growth Rates

In order to learn about disturbance growth, the maximum streamwise velocity disturbance is extracted from the wall–normal direction in the boundary layer and plotted vs. axial distance for different crossflow disturbance paths. The maximum streamwise velocity disturbance is a good indicator of overall disturbance growth since it is much larger than disturbances in other quantities.

For each crossflow vortex, there is a positive streamwise disturbance which is being rotated downward toward the wall, and a negative streamwise disturbance which is being rotated away from the wall. These two disturbances evolve differently in space, and the growth of the positive streamwise disturbance is considered in Figure 6.16.

Figure 6.16a plots u'_{max} for three different disturbances at high Re with 2 μm roughness. The disturbances are designated Disturbance 1, 2, and 3, and are marked in Figure 6.12. Each disturbance experiences a long period of exponential growth as indicated by the constant slope on a logarithmic plot. At a certain axial location, non–linear effects become important and the disturbance saturates, ceasing to grow exponentially and instead growing algebraically. Saturation amplitudes occur somewhere between 40 and 50% of the free stream, and maximum amplitudes are about 56% for Disturbance 1 and 65% for Disturbance 2. These axial locations where saturation occurs roughly correspond with where sharp increases in wall heating are seen. Disturbance 1, which is the leading midspan disturbance, has the largest growth rate. Disturbance 3 saturates but does not reach its maximum amplitude by the end of the geometry.

Figure 6.16b compares disturbance amplitudes between the high and low Reynolds number conditions. We see that the growth rates are smaller for the low Reynolds number, an expected result. Amplitudes reached by the low Reynolds number case are about 10%, significantly below saturation amplitude.

Figures 6.16c and 6.16d compare disturbance amplitudes across roughness heights for Disturbance 1 and 2, respectively. Each disturbance has nearly the same growth rate across roughness heights and only the initial amplitude changes. Saturation amplitudes and maximum amplitudes remain relatively constant for each roughness, which is consistent with seeing the same maximum heat flux across roughnesses.

The exponential growth of disturbances explains the relationship of roughness height

to the shape of the heating front as described by Figure 6.13. When scaling the initial amplitude of disturbances by a certain factor, the location x_{crit} at which the disturbance reaches a given amplitude will scale by a factor that is inversely proportional to the exponential growth rate. Hence, changing the initial amplitude will affect the location of x_{crit} more greatly for disturbances with smaller growth rates. Disturbances will tend to have higher growth rates the closer they are to the center of the midspan region, where the crossflow magnitude is the largest (see Figures 6.16a and 6.12), and so the heating pattern broadens due to the disturbances outside of the center midspan region moving forward further.

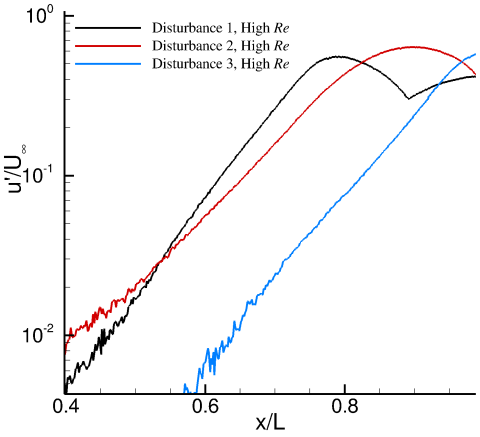

(a) High Re, 2 μm roughness

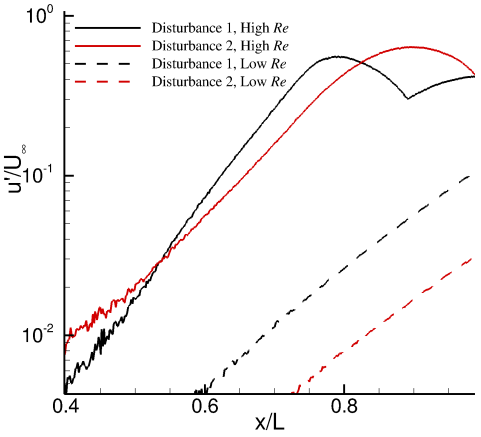

(b) High Re vs. low Re, 2 μm roughness

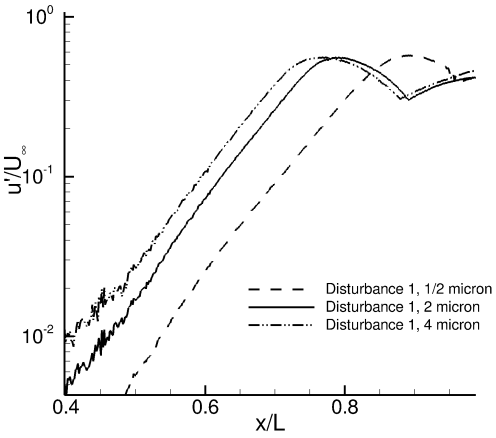

(c) Disturbance 1, high Re, all three roughness heights

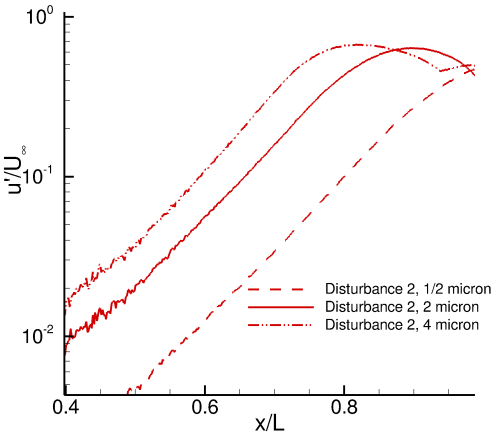

(d) Disturbance 2, high Re, all three roughness heights

Figure 6.16: Maximum streamwise velocity disturbances vs. axial distance for several cases.

Exponential fits can be applied to the curves in Figure 6.16a to approximate the growth rates of the disturbances in the linear regime. These growth rates can in turn be used to calculate N factors based on u'_{max} along each disturbance path. N factors are computed for Disturbances 1–3 and plotted on top of the linear stability analysis result at $Re = 9.84 \times 10^6$ from Choudhari et al.[53] for stationary crossflow in Figure 6.17. The plot shows reasonable agreement, with DNS reaching larger N factors than the linear stability analysis further from the centerline. Some of the discrepancy should be attributed to the difference in Reynolds number, and differences in integration path could also be a reason for disagreement.

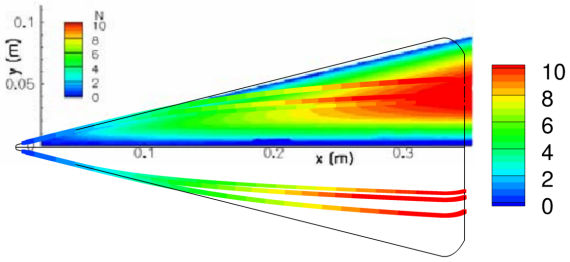

Figure 6.17: N factors from DNS (along lines) plotted on top of N factors from linear stability theory by Choudhari et al.[53]

6.7 Vortex Coalescence

The high Reynolds number case with the 4 μm roughness allows us to better understand the downstream evolution of disturbances than other cases. Again looking at the bottom of Figure 6.12, we can see the "turn over" of disturbances causing the disappearance and reappearance of streaks near the back of the geometry. However, in two instances a streak seems to disappear entirely, and this is attributed to the interaction of two vortical disturbances forming to become one, i.e., a coalescence. These two instances are marked on the figure.

Figure 6.18 shows unwrapped axial slices of density for the 4 μm case, and the coalescences begin with the disturbances located at $z = 0.025$ m and 0.035 m. Both locations show a vortex disturbance which crests and then collapses, with the vortex to the left then beginning to engulf the collapsed vortex. Figure 6.19, which shows streamwise velocity disturbance in the fashion of Figure 6.10, demonstrates that the disturbance at $z = 0.035$ m has coalesced unequivocally. Upstream, two distinct positive–negative disturbance pairs are present, and at the end of the geometry a single positive–negative pair prevails.

The evolution of the data in Figures 6.18 and 6.19 suggest that the physical cause of vortex coalescence is dependent on the relative states of the participating vortices. For both the coalescences that are observed here, the right (engulfed) vortex is further along in its development compared to its left neighbor, and is in a state that has been referred to in this paper as collapsed. The left vortex is cresting, and it seems reasonable this left vortex can engulf the right, due to the right's vortical structure being disorganized from impinging on the wall. If this is indeed the mechanism by which coalescence occurs, then it would require the condition that the engulfing vortex lags the engulfed vortex in terms of its evolved state. It follows that for these simulated cases of HIFiRE–5, coalescence would only likely occur between the leading disturbance in the midspan region and the centerline, which is where the condition would typically exist due to the shape of the heating front.

Despite the suggestive appearance of the wall heat flux at certain locations, it seems unlikely that flow conditions could arise for a vortex to bifurcate (i.e. split into two separate vortices).

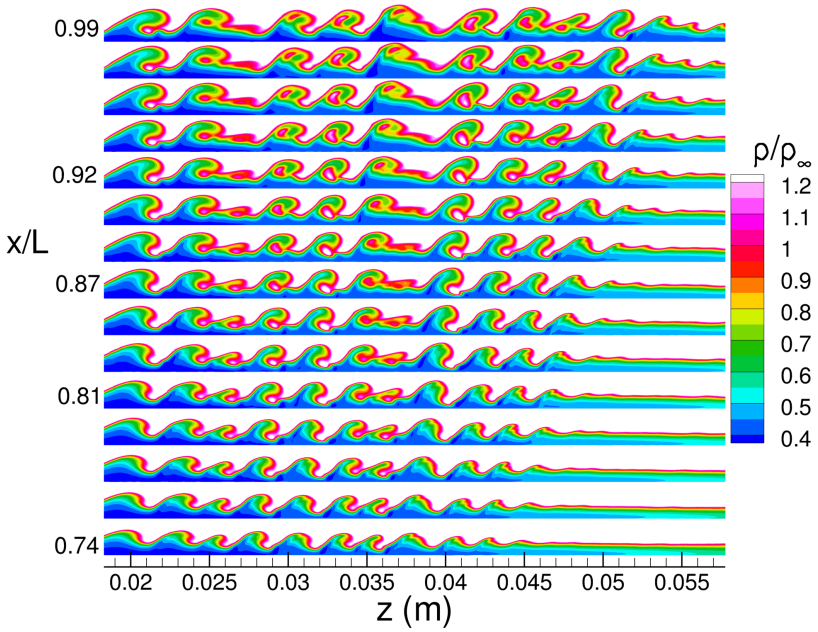

Figure 6.18: Contours of density from several axial locations unwrapped for the 4 μm case.

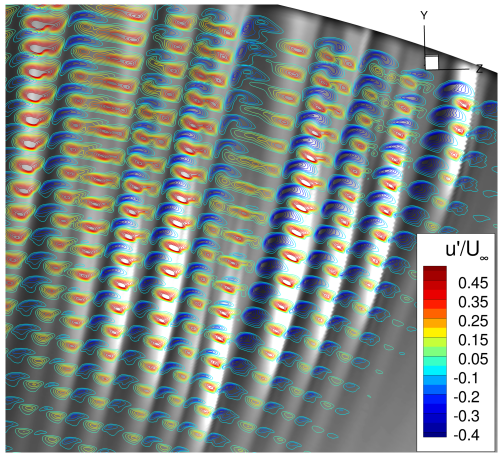

Figure 6.19: Overlay of streamwise velocity disturbance onto wall heat flux for 4 μm case, showing disturbance coalescence.

6.8 Vortex Doubling

Stationary crossflow vortices experience a long period of exponential growth and begin to roll up, as depicted in Figure 6.20a. Further downstream, nonlinear effects become apparent and a "hump" can form between the large vortices, as shown in Figure 6.20. This phenomenon is sometimes referred to as *vortex doubling*, and it can be seen in many of the results of the present work. The hump appears shortly after the disturbance has impinged upon the wall, and the trough on either side of the hump corresponds to the simultaneous presence of the streamwise pair of heat flux streaks described in Section 6.3.

Looking again at Figure 6.10b, we see the streamwise pairs of heat flux streaks underneath each vortex. Examining the upstream streaks, we see that on the downstream side, several of the streaks become split length wise by a small sliver of lower heat flux. This causes the upstream streaks to appear to have small tails. These tails are more discernible for the 4 μm case which can be seen in Figure 6.19. The source of this effect is a spot of locally high temperature which forms underneath the hump created during vortex doubling. It would likely be very difficult to observe this phenomenon if the flow contained unsteadiness from secondary instabilities.

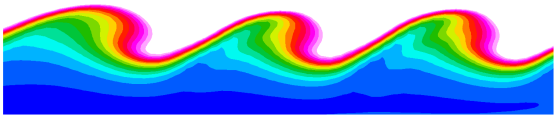

(a) Rolling up of vortices.

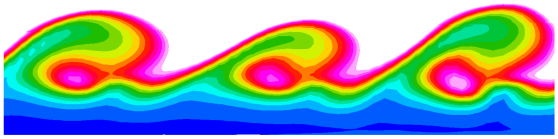

(b) Downstream, vortex doubling occurs.

Figure 6.20: Example of vortex doubling.

6.9 Comparison to Tunnel Results

Comparison of the present work to the BAM6QT results is somewhat limited to comparing surface quantities that can be measured in the tunnel. Examining the wall heat

flux, the high heating streaks in the computations just exceed 0.8 W/cm^2 at the high Re condition, which is very close to what is seen by Juliano et al.[84] using TSP. However, Borg and Kimmel[75] see values just above 0.6 W/cm^2 in the streaks using IR thermography on the PEEK model. It is unknown whether this discrepancy is due to differences in the observation technique or differences with the tunnel models, but the computations nonetheless show good agreement with experiment.

At the high Re condition, the location of the heating front in experiment is bounded by the locations of the heating fronts of the 1/2 micron and two micron DNS cases. While it is not expected for the computational roughness to produce the same disturbance amplitudes as physical roughness of similar height (for reasons explained in Section 5.2), the experimental heating front location is very similar to the 1/2 micron DNS case, occuring perhaps just a few cm forward. The PEEK model has rms roughness heights of about 1/2 micron for the first 45% of its surface, therefore the comparable 1/2 micron DNS case seems to be providing similar initial conditions since the heating front locations are also similar.

The simulations of the present work are dissimilar from the tunnel results in one key way which can be explained by the differences in the computational setup. Looking again at Figure 6.12, the heating streaks caused by the vortices in the DNS results remain separated even as the disturbances impinge on the wall, with regions in between the streaks having heat flux values close to the background heat flux of the baseflow. This is in contrast to experiment, where after disturbance impingement there is some spreading of each streak which results in the heating pattern blending together. The largest values of heat flux are still along each streak, and the streaks are still distinguishable from one another, but the heat flux in between the streaks is somewhat higher than the baseflow. This difference can be traced back to the lack of free stream acoustic disturbances in the DNS which are present in the tunnel. This free stream content provides excitation for secondary instabilities that are triggered by the large modification of the basic state due to the presence of the stationary crossflow vortices. The additional disturbance growth is most likely responsible for the blending of the heating pattern, and in fact the flow could be transitional in this region; this is supported by the observation of broadband pressure spectra near the back of the geometry in the experiments. Since the simulations do not contain free stream disturbances that excite secondary instabilities, the mechanism for

the blending does not exist.

6.10 Receptivity of Attachment Line

Looking again at Figure 6.15a, we see that virtually all of the disturbance paths originating at the nose stay very close to the attachment line for a significant portion of the geometry before being swept up towards the midspan region. It is expected that the disturbances are seeded at the point along these paths when they are swept away from the attachment line because a) the boundary layer is at its thinnest near the attachment line, and therefore the roughness is at its largest compared to the boundary layer height, and b) disturbances ahead of this point would "share" the same physical space and experience significant crowding effects, preventing their formation. Disturbance paths which occupy the midspan region where crossflow dominates are swept off the attachment line by approximately $x/L = 0.3$, while flow very near to the nose is swept up into the counter–rotating baseflow vortex near the centerline. It follows that HIFiRE–5 is likely most receptive to forcing in the region near the attachment line just downstream of the nose and before $x/L = 0.3$.

The explanation of the receptive region of HIFiRE–5 by the previous paragraph has implications on hypothetically using DREs to excite stationary crossflow on this geometry. Firstly, an azimuthal ring of DREs around the forebody at some axial location would probably be ineffective. The best DRE configuration would likely be in a ray along the attachment line. Secondly, if a particular disturbance wavenumber was being targeted to appear near the back of the geometry, then one would have to account for the large amount of spreading, and also for the fact that the disturbance wavelength would be different then the distance between DREs at the attachment line. This difference exists because the locations of where two disturbances originate (at the DREs) are further apart than the disturbance path lines once they have been swept off of the attachment line.

6.11 Nose Radius Effects

A simulation of the HIFiRE–5 geometry with a nose radius of half the original was conducted, which provides insight on the effect of nose sharpness on the resulting flowfield. The simulation used the medium size grid topology, the high Reynolds number conditions, and a unique random roughness pattern was applied.

Figure 6.21 compares the baseflow solutions for the blunt and sharp case. The sharp nose causes the centerline vortex heating streak to be much smaller compared to the nominal case, and the resulting centerline vortex system is more developed, which can be seen in the wall heat flux. This can be thought of as an effective increase in the Reynolds number of the flow.

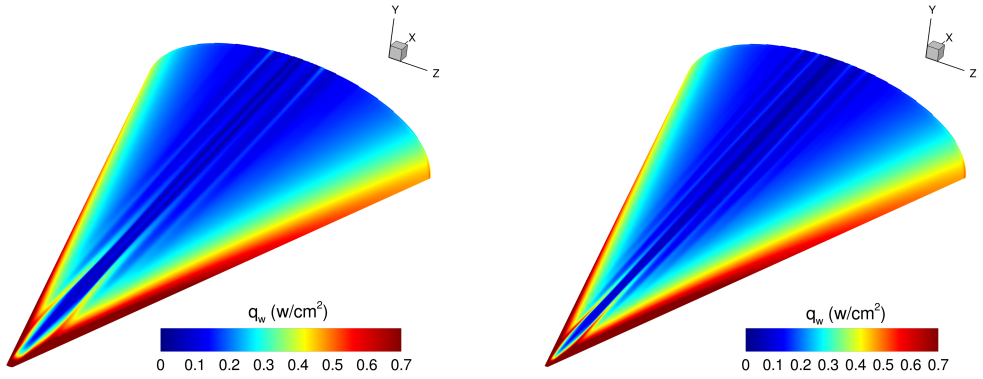

(a) Blunt (b) Sharp

Figure 6.21: Baseflow surface heat flux at high Re for the blunt and sharp cases.

The disturbed solution for the sharp nose case is significantly different from the blunt cases. The heating pattern is much further forward, with disturbances impinging as early as $x/L = 0.51$, and the shape of the pattern has also changed, as shown in Figure 6.22. Disturbance impingement is further forward closer to the centerline, giving the front a more triangular shape. Clearly, nose sharpness is a destabilizing effect for stationary crossflow. Even though decreasing the nose radius has similar effects on disturbance growth as increasing the Reynolds number, the decrease in nose radius did not seem to affect the spanwise disturbance wavenumber like increasing the Reynolds

number does. Figure 6.23 shows that the wavelength (and hence wavenumber) evolution is very similar for both the blunt and sharp nose cases at high Re. This is likely because the disturbance wavelength is driven by the boundary layer height, which is similar for both cases away from the nose region.

One possible explanation for the change in the shape of the heating front is how changing the nose radius could affect the most receptive region of the flow (this region is described in Section 6.10). Reducing the nose radius results in a flow that is self–similar to the larger nose radius case near the nose region, and this results in the receptive region moving forward on the geometry. The first crossflow disturbance path that is swept away from the attachment line is thus further forward on the geometry, and therefore resides closer to the centerline once it proceeds downstream. This would mean that the leading disturbance (the first disturbance to impinge) would move closer to the centerline with increasing nose sharpness.

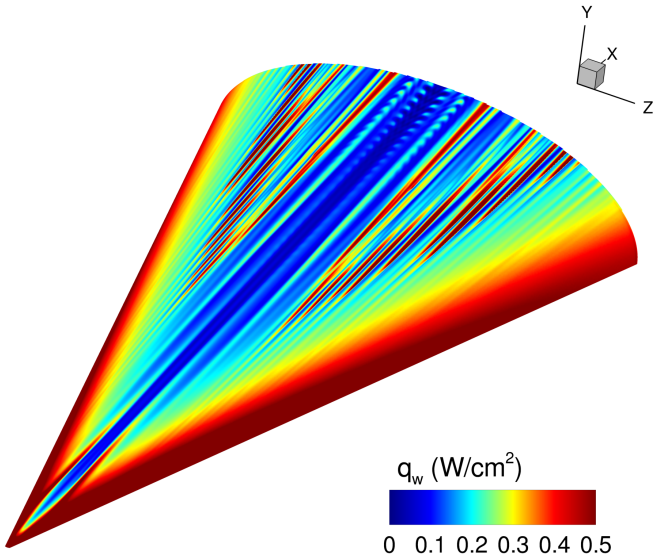

Figure 6.22: Wall heat flux for the sharp case.

Figure 6.24 plots crosscuts of density for the sharp case in the style of previous figures, but shows more of the flowfield. Several vortices belonging to the centerline

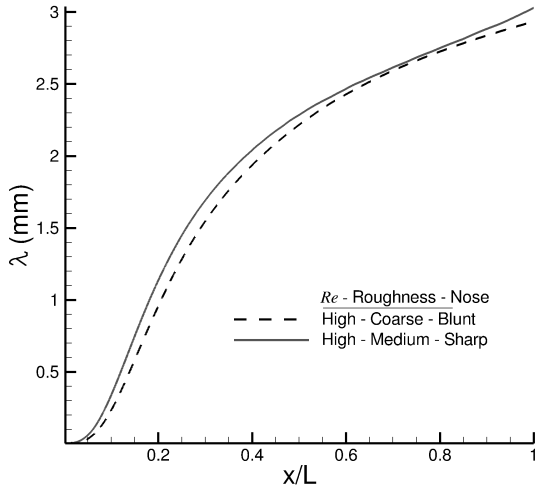

Figure 6.23: Comparison of spanwise disturbance wavelength evolution for blunt and sharp cases.

vortex system can be seen on the left. The sharp nose allows us to see even further downstream of initial disturbance impingement than the 4 μm roughness blunt case, and the resulting flowfield is extremely complex. A trio of vortices just outboard of $z = 2$ cm lift very far off the wall, resulting in a large section of relatively low heat flux beneath them. Meanwhile, the vortex just inboard of $z = 2$ cm is impinging by $x/L = 0.6$, and then it collapses and begins to roll up again by $x/L = 0.8$. Beyond this location, the vortex does not re–impinge; this could be because the vortex is not being "fed" additional fluid or disturbance energy, since the boundary layer is extremely warped. If this is true, then it would imply that crossflow vortices are unlikely to impinge on the wall more than once.

Interestingly, despite the extremely evolved states of the disturbances, no stationary vortices seem to be coalescing. This supports the physical mechanism for coalescence described in Section 6.7, because the described condition does not exist in this flow. That is, for any adjacent pair of vortices in Figure 6.24, the outboard vortices are never in a more evolved state than their inboard neighbors. This trend can also be seen in the heating pattern in Figure 6.22.

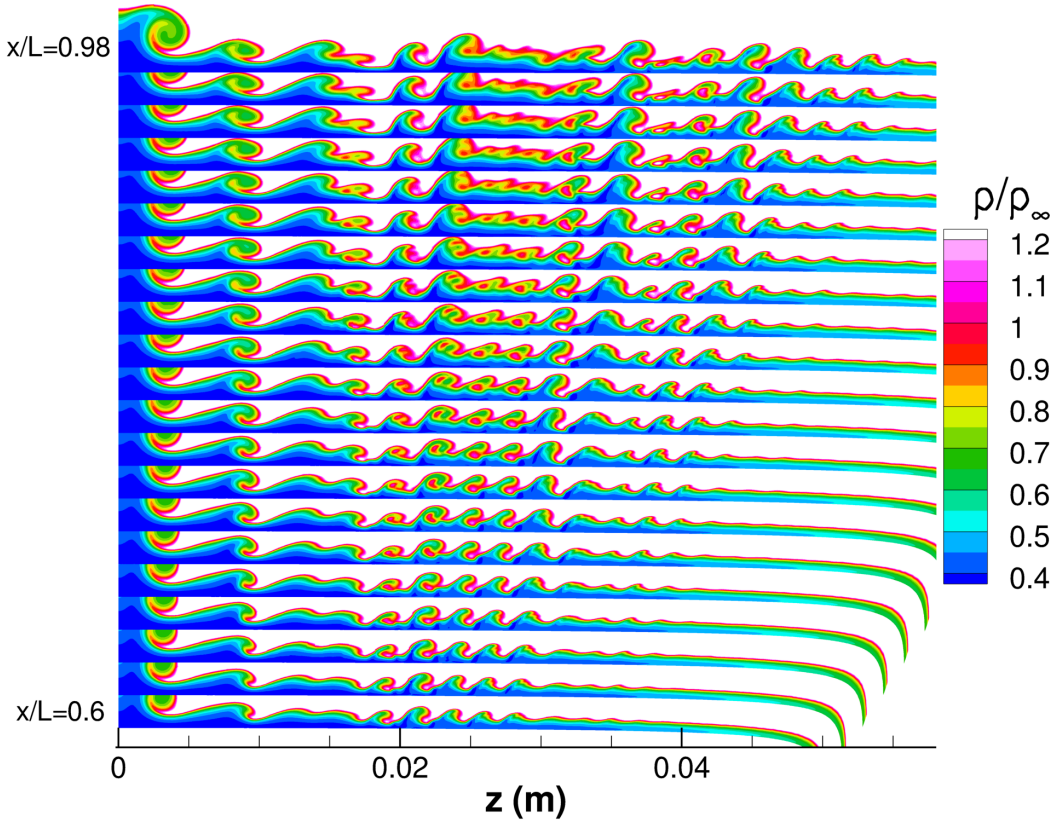

Figure 6.24: Crosscuts of density plotted for the sharp nose case at several axial locations.

Chapter 7

Conclusion

Direct numerical simulations of HIFiRE–5 were conducted using a distributed roughness method to emulate smooth–body transition.

It was found that the particular configuration of crossflow disturbances in each case was very sensitive to the initial conditions provided by the roughness, although on average the wavelengths and amplitudes of the disturbances were very similar. Interpolating the same roughness pattern onto finer grids resulted in a converged solution. Wavelengths near the end of the geometry were similar to those seen in experiment, with values of 3–4 mm. There was a clear dependence of the wavelength on Reynolds number, and a large amount of spreading occurs due to the disturbances initially having wavelengths of less than 1 mm.

Disturbances experienced a long period of exponential growth and were seen to saturate around 40–50% of the free stream velocity, with maximum amplitudes as large as 65%. Increasing the roughness heights brought the heating pattern forward without changing the growth rates. The shape of the heating front changed significantly, but in a manner consistent with disturbances experiencing exponential growth.

Streaks of high heating followed by subsequent lower heating downstream that was seen in experiment was also observed in these computations at the high Reynolds number condition. This phenomenon in the computations was caused by the large streamwise velocity disturbance impinging on the wall. This is a steady physical mechanism that demonstrates the flow need not be turbulent to display these types of heating patterns. The mechanism could also explain similar phenomena seen on other geometries that

experience streamwise vortices, regardless of the cause of the vortices themselves. The slender cone at an angle of attack may be less susceptible to this phenomenon because the convex curvature of the disturbance paths causes the vortices to lift away from the wall.

For the high Reynolds number condition and 4 μm roughness, in certain instances two vortices were observed to coalesce. This could be caused when one vortex is cresting while the other is in a collapsed state due to having impinged on the wall, which suggests that the relative states of two vortices are important for determining if coalescence will occur.

Future Work

Insight into these crossflow phenomena provided by the present work demonstrates the utility of direct numerical simulation, and continued application in the area of crossflow instability would be very useful for better understanding of underlying flow physics. There are a variety of avenues for future work in applying DNS to HIFiRE–5 or other three–dimensional transition problems:

- Adding free stream acoustic waves to the computational inflow could provide excitation for secondary instabilities to more closely resemble tunnel conditions; this could cause better agreement with experiment and would allow for additional analysis.
- A study could be conducted by adding DREs to the model surface along with the computational distributed roughness to explore interaction between the forced DRE wavenumber and the flow–selected modes.
- DRE spacings could be selected to attempt to suppress the most unstable mode and hence delay transition. As computational resources become cheaper, larger calculations would allow for finer and better resolved distributed roughness to confirm that the appearing wavelengths are flow–selected.
- The area over which the distributed roughness is applied could be reduced to determine where it is most effective.

References

[1] Osborne Reynolds. An experimental investigation of the circumstances which determine whether the motion of water shall be direct or sinuous, and of the law of resistance in parallel channels. *Proceedings of the royal society of London*, 35(224-226):84–99, 1883.

[2] Peter J Schmid and Dan S Henningson. *Stability and transition in shear flows*, volume 142. Springer Science & Business Media, 2012.

[3] Patrick Huerre and Peter A Monkewitz. Local and global instabilities in spatially developing flows. *Annual review of fluid mechanics*, 22(1):473–537, 1990.

[4] MV Morkovin, E Reshotko, and Th Herbert. Transition in open flow systems-a reassessment. *Bull. Am. Phys. Soc*, 39(9), 1994.

[5] Christoph J Mack, Peter J Schmid, and Joern L Sesterhenn. Global stability of swept flow around a parabolic body: connecting attachment-line and crossflow modes. *Journal of Fluid Mechanics*, 611:205–214, 2008.

[6] LM Mack. Boundary layer stability theory. jpl rep. 900-277. *Jet Propulsion Lab., California Institute of Technology, Pasadena, CA, USA*, 1969.

[7] Alexander Fedorov. Transition and stability of high-speed boundary layers. *Annual Review of Fluid Mechanics*, 43:79–95, 2011.

[8] JL Van Ingen. A suggested semi-empirical method for the calculation of the boundary layer transition region. Technical report, Delft University of Technology, 1956.

[9] JL Van Ingen. The en method for transition prediction. historical review of work at tu delft. In *38th Fluid Dynamics Conference and Exhibit*, pages 23–26, 2008.

[10] Jean-Marc Chomaz. Global instabilities in spatially developing flows: non-normality and nonlinearity. *Annu. Rev. Fluid Mech.*, 37:357–392, 2005.

[11] Helen L Reed, William S Saric, and Daniel Arnal. Linear stability theory applied to boundary layers. *Annual review of fluid mechanics*, 28(1):389–428, 1996.

[12] Thorwald Herbert. Parabolized stability equations. *Annual Review of Fluid Mechanics*, 29(1):245–283, 1997.

[13] Leslie M Mack. Boundary-layer linear stability theory. Technical report, DTIC Document, 1984.

[14] WE Gray. *The effect of wing sweep on laminar flow*. Royal Aircraft Establishment, 1952.

[15] Edward B White and William S Saric. Secondary instability of crossflow vortices. *Journal of Fluid Mechanics*, 525:275–308, 2005.

[16] B Mueller and H Bippes. Experimental study of instability modes in a three-dimensional boundary layer. In *In AGARD, Fluid Dynamics of Three-Dimensional Turbulent Shear Flows and Transition 15 p (SEE N90-10356 01-34)*, volume 1, 1989.

[17] H Deyhle and H Bippes. Disturbance growth in an unstable three-dimensional boundary layer and its dependence on environmental conditions. *Journal of Fluid Mechanics*, 316(73):114, 1996.

[18] Mark S Reibert, William S Saric, RB Carrillo Jr, and KL Chapman. Experiments in nonlinear saturation of stationary crossflow vortices in a swept-wing boundary layer. *AIAA paper*, 1996.

[19] William S Saric, Ruben B Carrillo, and Mark S Reibert. Nonlinear stability and transition in 3-d boundary layers. *Meccanica*, 33(5):469–487, 1998.

[20] Ronald H Radeztsky, Mark S Reibert, and William S Saric. Effect of isolated micron-sized roughness on transition in swept-wing flows. *AIAA journal*, 37(11):1370–1377, 1999.

[21] Ronald Radeztsky. Effect of micron-sized roughness on transition in swept-wing flows. In *AIAA, Aerospace Sciences Meeting and Exhibit, 31 st, Reno, NV*, 1993.

[22] Meelan Choudhari. Roughness-induced generation of crossflow vortices in three-dimensional boundary layers. *Theoretical and Computational Fluid Dynamics*, 6(1):1–30, 1994.

[23] J Ray Dagenhart and William S Saric. *Crossflow stability and transition experiments in a swept-wing flow*, volume 209344. Citeseer, 1999.

[24] H Bippes and B Müller. Disturbance growth in an unstable three-dimensional boundary layer. In *Numerical and Physical Aspects of Aerodynamic Flows IV*, pages 345–358. Springer, 1990.

[25] Steven P Schneider. Effects of roughness on hypersonic boundary-layer transition. *Journal of Spacecraft and Rockets*, 45(2):193–209, 2008.

[26] William S Saric, Helen L Reed, and Edward B White. Stability and transition of three-dimensional boundary layers. *Annual Review of Fluid Mechanics*, 35(1):413–440, 2003.

[27] Yasuaki Kohama, Williams Saric, and Jona Hoos. A high-frequency, secondary instability of crossflow vortices that leads to transition. *Boundary layer transition and control*, page 4, 1991.

[28] Peter Wassermann and Markus Kloker. Mechanisms and passive control of crossflow-vortex-induced transition in a three-dimensional boundary layer. *Journal of Fluid Mechanics*, 456:49–84, 2002.

[29] Mujeeb R Malik, Fei Li, Meelan M Choudhari, and Chau-Lyan Chang. Secondary instability of crossflow vortices and swept-wing boundary-layer transition. *Journal of Fluid Mechanics*, 399:85–115, 1999.

[30] Lian L Ng and Gordon Erlebacher. Secondary instabilities in compressible boundary layers. *Physics of Fluids A: Fluid Dynamics (1989-1993)*, 4(4):710–726, 1992.

[31] Erik Janke and Ponnampalam Balakumar. On the secondary instability of three-dimensional boundary layers. *Theoretical and Computational Fluid Dynamics*, 14(3):167–194, 2000.

[32] MR Malik, F Li, and C-L Chang. Nonlinear crossflow disturbances and secondary instabilities in swept-wing boundary layers. In *IUTAM Symposium on Nonlinear Instability and Transition in Three-Dimensional Boundary Layers*, pages 257–266. Springer, 1996.

[33] Helen L Reed, Eduardo Perez, Joseph Kuehl, Travis Kocian, and Nicholas Oliviero. Verification and validation issues in hypersonic stability and transition prediction. *Journal of Spacecraft and Rockets*, 52(1):29–37, 2014.

[34] William S Saric and Helen L Reed. Crossflow instabilities–theory & technology. *AIAA paper*, 2003.

[35] H Bippes. Basic experiments on transition in three-dimensional boundary layers dominated by crossflow instability. *Progress in aerospace sciences*, 35(4):363–412, 1999.

[36] Fabio P Bertolotti. On the connection between cross-flow vortices and attachment-line instabilities. In *Laminar-Turbulent Transition*, pages 625–630. Springer, 2000.

[37] Roger L Kimmel, Jonathan Poggie, and Stephen N Schwoerke. Laminar-turbulent transition in a Mach 8 elliptic cone flow. *AIAA journal*, 37(9):1080–1087, 1999.

[38] Roger L Kimmel and J Poggie. Transition on an elliptic cone at Mach 8. *American Society of Mechanical Engineers ASME FEDSM97-3111*, 1997.

[39] Roger L Kimmel and J Poggie. Three-dimensional hypersonic boundary layer stability and transition. Technical report, DTIC Document, 1997.

[40] John David Schmisseur. Receptivity of the boundary layer on a Mach-4 elliptic cone to laser-generated localized freestream perturbations. 1997.

[41] JD Schmisseur, Steven P Schneider, and Steven H Collicott. Receptivity of the Mach-4 boundary layer on an elliptic cone to laser-generated localized freestream perturbations. In *AIAA, Aerospace Sciences Meeting & Exhibit, 36 th, Reno, NV*, 1998.

[42] JD Schmisseur, Steven P Schneider, and Steven H Collicott. Response of the Mach-4 boundary layer on an elliptic cone to laser-generated freestream perturbations. In *AIAA, Aerospace Sciences Meeting and Exhibit, 37 th, Reno, NV*, 1999.

[43] Michael S Holden. Experimental studies of laminar, transitional, and turbulent hypersonic flows over elliptic cones at angles of attack. Technical report, DTIC Document, 1998.

[44] Kenneth F Stetson. Mach 6 experiments of transition on a cone at angle of attack. *Journal of Spacecraft and Rockets*, 19(5):397–403, 1982.

[45] Ponnampalam Balakumar and Lewis R Owens. Stability of hypersonic boundary layers on a cone at an angle of attack. *AIAA Paper*, 2010.

[46] Joseph Kuehl, Eduardo Perez, and Helen L Reed. Jokher: Npse simulations of hypersonic crossflow instability. *AIAA Paper*, 2012.

[47] Joel E Gronvall, Heath B Johnson, and Graham V Candler. Hypersonic three-dimensional boundary layer transition on a cone at angle of attack. *AIAA Paper*, 2011.

[48] Erick O Swanson and Steven P Schneider. Boundary-layer transition on cones at angle of attack in a Mach-6 quiet tunnel. In *48th AIAA Aerospace Sciences Meeting Including the New Horizons Forum and Aerospace Exposition*, 2008.

[49] Stuart Craig and William Saric. Experimental study of crossflow instability on a Mach 6 yawed cone. *Bulletin of the American Physical Society*, 59, 2014.

[50] Roger L Kimmel, David Adamczak, Karen Berger, and Meelan Choudhari. HIFiRE–5 flight vehicle design. *AIAA paper*, 2010.

[51] Ariovaldo Felix Palmerio, José Pedro Claro Peres da Silva, Peter Turner, and Wolfgang Jung. The development of the VSB–30 sounding rocket vehicle. In *European*

Rocket and Balloon Programmes and Related Research, volume 530, pages 137–140, 2003.

[52] *NASA Sounding Rocket Program Handbook*. 2005.

[53] Meelan Choudhari, Chau-Lyan Chang, Thomas Jentink, Fei Li, Karen Berger, Graham Candler, and Roger Kimmel. Transition analysis for the HIFiRE–5 vehicle. *AIAA paper*, 2009.

[54] F McNeil Cheatwood and Peter A Gnoffo. *User's manual for the Langley aerothermodynamic upwind relaxation algorithm (LAURA)*. National Aeronautics and Space Administration, Langley Research Center, 1996.

[55] White JA and Morrison JH. A psuedo-temporal multi-grid relaxation scheme for solving the parabolized navier-stokes equations. 1999.

[56] Heath B Johnson and Graham V Candler. Hypersonic boundary layer stability analysis using PSE-Chem. *AIAA paper*, 2005.

[57] Chau-Lyan Chang. Lastrac. 3d: Transition prediction in 3d boundary layers. *AIAA Paper*, 2004.

[58] Mujeeb R Malik, Fei Li, and Meelan Choudhari. Analysis of crossflow transition flight experiment aboard the pegasus launch vehicle. *AIAA paper*, 2007.

[59] Ryan Gosse, Roger Kimmel, and Heath B Johnson. Study of boundary-layer transition on hypersonic international flight research experimentation 5. *Journal of Spacecraft and Rockets*, 51(1):151–162, 2013.

[60] Ian J Lyttle and Helen L Reed. Use of transition correlations for three-dimensional boundary layers within hypersonic flows. *AIAA Paper*, 1995.

[61] Karen Berger, Shann Rufer, Roger Kimmel, and David Adamczak. Aerothermodynamic characteristics of boundary layer transition and trip effectiveness of the HIFiRE flight 5 vehicle. *AIAA paper*, 2009.

[62] P Paredes and V Theofilis. Spatial linear global instability analysis of the HIFiRE–5 elliptic cone model flow. *AIAA-Paper*, 2013.

[63] P Paredes and V Theofilis. Traveling global instabilities on the HIFiRE–5 elliptic cone model flow. *AIAA Paper*, 75, 2014.

[64] Matthew T Lakebrink and Matthew P Borg. Traveling crossflow wave predictions on the HIFiRE-5 at Mach 6: Stability analysis vs. quiet tunnel data. In *54th AIAA Aerospace Sciences Meeting*, 2016.

[65] Steven P Schneider, Craig Skoch, Shann Rufer, and Erick Swanson. Hypersonic transition research in the Boeing/AFOSR Mach-6 quiet tunnel. *AIAA paper*, 2003.

[66] Steven P Schneider. Effects of high-speed tunnel noise on laminar-turbulent transition. *Journal of Spacecraft and Rockets*, 38(3):323–333, 2001.

[67] Ivan E Beckwith, Theodore R Creel Jr, Fang-Jenq Chen, and James M Kendall. Free-stream noise and transition measurements on a cone in a Mach 3.5 pilot low-disturbance tunnel. *NASA STI/Recon Technical Report N*, 83, 1983.

[68] IE Beckwith and CG Miller III. Aerothermodynamics and transition in high-speed wind tunnels at NASA Langley. *Annual Review of Fluid Mechanics*, 22(1):419–439, 1990.

[69] Steven P Schneider and Christine E Haven. Quiet–flow Ludwieg tube for high-speed transition research. *AIAA journal*, 33(4):688–693, 1995.

[70] Thomas J Juliano and Steven P Schneider. *Instability and transition on the HIFiRE–5 in a Mach-6 quiet tunnel*. Defense Technical Information Center, 2010.

[71] Matthew P Borg, Roger Kimmel, and Scott Stanfield. HIFiRE–5 attachment-line and crossflow instability in a quiet hypersonic wind tunnel. *AIAA Paper*, 2011.

[72] Matthew P Borg, Roger L Kimmel, and Scott Stanfield. Crossflow instability for HIFiRE–5 in a quiet hypersonic wind tunnel. *AIAA paper*, 2012.

[73] Matthew P Borg, Roger L Kimmel, and Scott Stanfield. Traveling crossflow instability for HIFiRE–5 in a quiet hypersonic wind tunnel. *AIAA Paper*, 2013.

[74] Thomas J Juliano, David Adamczak, and Roger L Kimmel. HIFiRE–5 flight test heating analysis. *AIAA Paper*, 76, 2014.

[75] Matthew P Borg and Roger L Kimmel. Simultaneous infrared and pressure measurements of crossflow instability modes for HIFiRE–5. 2016.

[76] Thomas J Juliano, Laura Paquin, and Matthew P Borg. Measurement of HIFiRE–5 boundary-layer transition in a Mach-6 quiet tunnel with infrared thermography. In *54th AIAA Aerospace Sciences Meeting*, 2016.

[77] Joseph L Steger and RF Warming. Flux vector splitting of the inviscid gasdynamic equations with application to finite-difference methods. *Journal of computational physics*, 40(2):263–293, 1981.

[78] Bram Van Leer. Towards the ultimate conservative difference scheme. v. a second-order sequel to godunov's method. *Journal of computational Physics*, 32(1):101–136, 1979.

[79] PL Roe. Characteristic-based schemes for the euler equations. *Annual review of fluid mechanics*, 18(1):337–365, 1986.

[80] F Ducros, V Ferrand, Franck Nicoud, C Weber, D Darracq, C Gacherieu, and Thierry Poinsot. Large-eddy simulation of the shock/turbulence interaction. *Journal of Computational Physics*, 152(2):517–549, 1999.

[81] Pramod K Subbareddy and Graham V Candler. A fully discrete, kinetic energy consistent finite-volume scheme for compressible flows. *Journal of Computational Physics*, 228(5):1347–1364, 2009.

[82] Ioannis Nompelis. *Computational study of hypersonic double-cone experiments for code validation*. 2004.

[83] GV Candler, HB Johnson, I Nompelis, VM Gidzak, PK Subbareddy, and M Barnhardt. Development of the US3D code for advanced compressible and reacting flow simulations. *AIAA Paper*, 2015-1893, 2015.

[84] Thomas J Juliano, Matthew P Borg, and Steven P Schneider. Quiet tunnel measurements of HIFiRE–5 boundary-layer transition. *AIAA Journal*, 53(4):832–846, 2015.

Appendix A

Selected Cases

This appendix includes selected computations that were run to produce intermediate results or address particular problems during the course of the work. These cases did not contribute to the salient results but were nonetheless important to the progress of the research.

A.1 Roughness proof of concept

A proof of concept for the roughness technique used in this work was executed by using a 2 micron roughness height and second order MSW fluxes on the coarse grid. Figure A.1 shows the clear excitation of crossflow disturbances in the wall heat flux; this demonstrated that the roughness was sufficient to generate crossflow vortices in the flow. Decreasing the roughness height to a half micron caused the disturbance heating rates to decrease, however the pattern stayed the same and the streaks did not change position.

The dissipative MSW scheme produced a very regular heating pattern, with much smaller amplitudes than the DNS cases with KEC fluxes. This same effect was seen when running with MSW fluxes on the fine grid. MSW is thus insufficient for capturing the real flow physics, as expected.

The presence of the roughness was necessary for generating a physical solution. Figure A.2 shows the wall heat flux for a calculation on the smooth (no roughness) fine grid with sixth order KEC fluxes. There is a small amount of stationary crossflow present

that is being introduced by the discrete nature of the grid itself. This uneven pattern of crossflow is much smaller in amplitude than what is seen in experiment, and the initial conditions of the disturbances are completely uncontrolled. Adding roughness overcomes this background influence and produces a result that is qualitatively very similar to the tunnel results. This smooth case also demonstrates that KEC fluxes cannot be used to compute a baseflow due to the scheme's ability to resolve the very small disturbances on the smooth grid. Finally, unsteadiness caused by the sixth order KEC scheme can also be seen in Figure A.2.

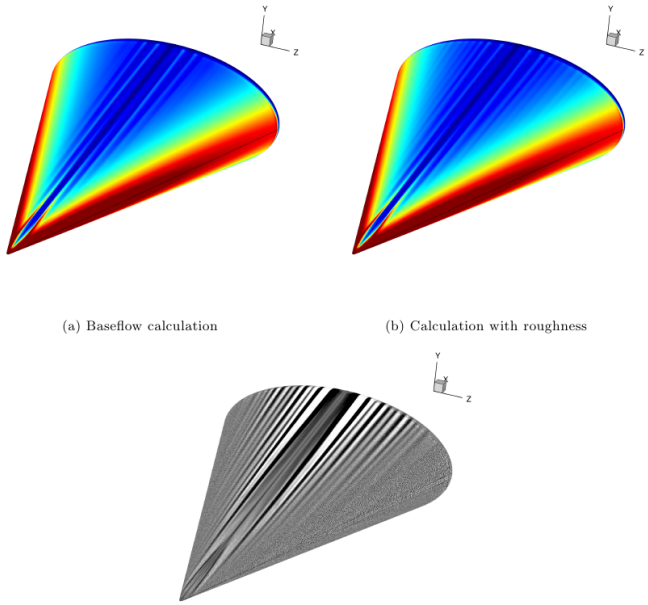

(a) Baseflow calculation

(b) Calculation with roughness

(c) Disturbance heat flux

Figure A.1: Proof of concept case for point–to–point roughness.

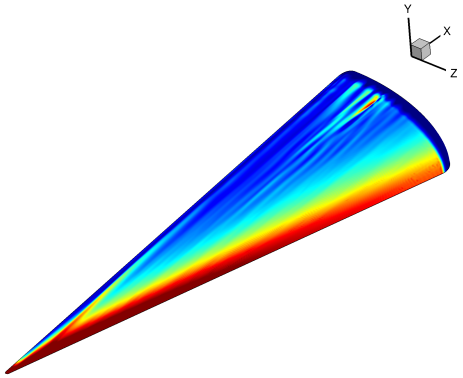

Figure A.2: Wall heat flux for smooth (no roughness) grid and sixth order KEC fluxes.

A.2 Cases with grid singularities near attachment line

The first grid topology design for this work placed the singularities near the attachment line. This design had the advantages of keeping grid cells aligned with the x–direction (the primarily downstream direction), and keeping the singularities far from the midspan region where crossflow vortices set up. However, the singularities produce numerical error that when introduced near the attachment line (where the flow is most receptive), the flow is destabilized enough to produce stationary crossflow disturbances even when using the dissipative MSW scheme. This made it impossible to compute a baseflow that was not polluted by crossflow disturbances. The grid topology was redesigned to locate the singularities near the centerline, which eliminated the source of numerical excitation at the attachment line at the expense of somewhat misaligning the grid with crossflow vortex paths.

It was initially unclear what was responsible for stationary crossflow growth in the baseflow calculations, and several attempts were made to eliminate crossflow disturbances with the first topology. Figure A.3 shows several different "baseflow" computations using the initial topology. Refining or coarsening the grid did not eliminate the crossflow disturbances, but did change the number of heating streaks that were present. This was a misleading trend, since each grid had the same number of singularities, suggesting that the singularities were not responsible for exciting the crossflow disturbances. Figure A.3c shows a case using first order MSW fluxes, which did eliminate the disturbance generation but also unacceptably altered the boundary layer profiles due to excessive dissipation. An intermediate approach was taken by using first order MSW only near the attachment line and second order MSW everywhere else, which produced a cleaner solution but still generated a single streak behind each 5–point/3–point singularity pair, finally revealing the influence of the singularities on the solution. This demonstrated that small grid irregularities could have a profound effect on the overall solution, and led to the idea of the distributed roughness method used for the body of this work. Moreover, using an improper grid topology to compute a baseflow is difficult to overcome.

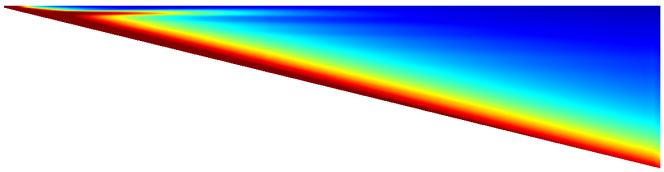

(a) 8 million elements, 2nd order inviscid fluxes

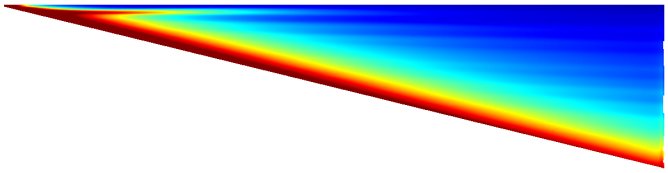

(b) 20 million elements, 2nd order inviscid fluxes

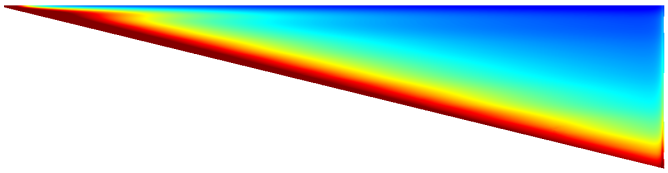

(c) 55 million elements, 1st order inviscid fluxes

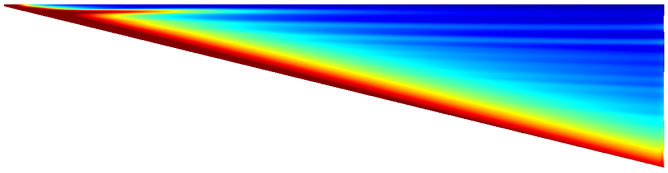

(d) 55 million elements, 2nd order inviscid fluxes

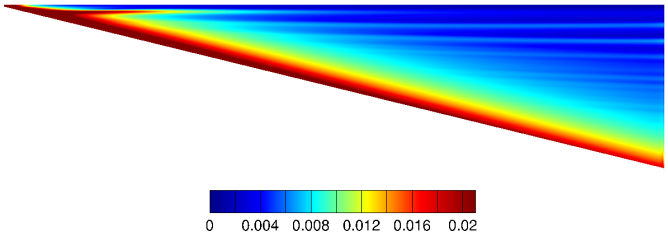

(e) 216 million elements, 2nd order inviscid fluxes

Figure A.3: Contours of wall heat flux $q_w/q_{w,max}$ for 5 different cases using the initial grid topology. The same value of $q_{w,max}$ is used to nondimensionalize each case.

A.3 Exploration of numerically generated noise

Computations at the high Reynolds number condition suffered from noise being generated at the nose when the KEC flux scheme was used. The noise then propagated downstream and caused the otherwise steady flowfield to become unsteady, and interfered with the formation of crossflow disturbances. While this noise did not have a considerable influence on the flowfield using second order KEC, the effect was exacerbated by increasing the order of accuracy of the scheme. Several cases were run to explore the cause of the noise and attempt to mitigate its effects, and these cases are presented here. Ultimately, the noise could not be eliminated for fourth or sixth order KEC and the high Re cases in the Results therefore use second order KEC.

Figure A.4a shows contours of the residual generated by the numerical noise in the attachment line and centerline planes near the nose. This residual propagates downstream and pollutes the solution with unsteady content, as shown in Figure A.4b. The noise interferes with the formation of the stationary crossflow vortices, indicated by the instantaneous wall heat flux in Figure A.4c.

The test cases exploring the numerical noise are enumerated here.

1. It was thought that the Ducros switch could be responsible for the noise. Cases using a Mach number based switch as well as a switch combining the Ducros and Mach switch did not eliminate the noise.

2. A switch flickering on and off in the subsonic region could be the culprit, so a case was run with the Ducros switch fully on in this region (dissipative flux is then added) and then blending back to normal downstream. However, unsteadiness was produced in the blending region and did not eliminate the problem.

3. The idea occurred to simply freeze the solution near the nose by zeroing the solution update once the bow shock was set up, but noise was again generated just downstream of where the solution was frozen.

4. The noise was present regardless of whether a point implicit or line implicit time integration scheme was used, and reducing the CFL number to one did not fix the problem.

5. Reducing the KEC scheme to fourth order resulted in less noise, but the stationary vortices were still greatly affected.

While using second order KEC instead of sixth order will have an effect on the solution, it is believed that the effect is minimal and the resolved flow contains the same relevant physics that a steady sixth order solution would.

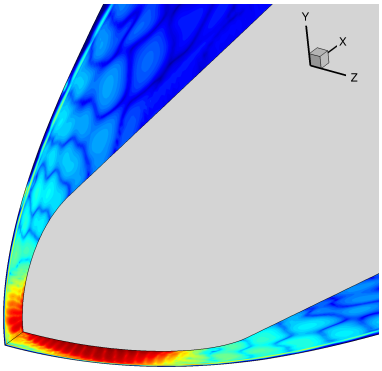

(a) Residual in the nose region generated by numerical noise

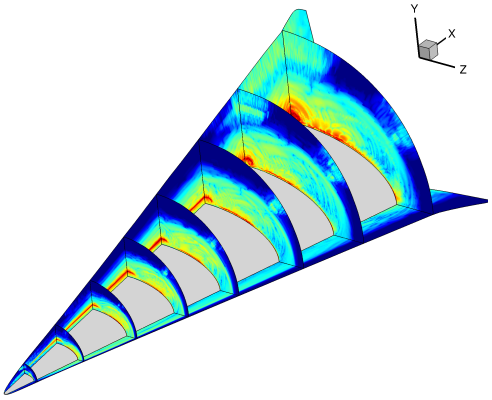

(b) Effect on residual throughout flowfield

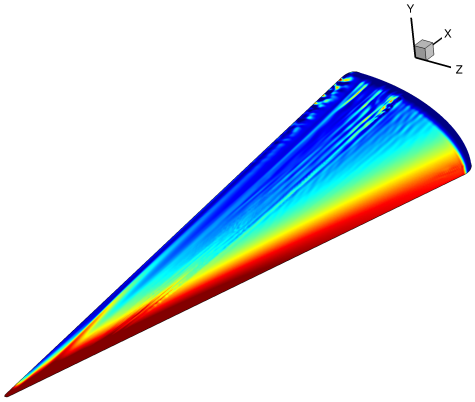

(c) Wall heat flux

Figure A.4: Effects of numerical noise generated at the nose, using sixth order KEC.

Appendix B

Supplementary Plots

This appendix provides supplementary results that do not warrant thorough discussion but may be valuable to the reader.

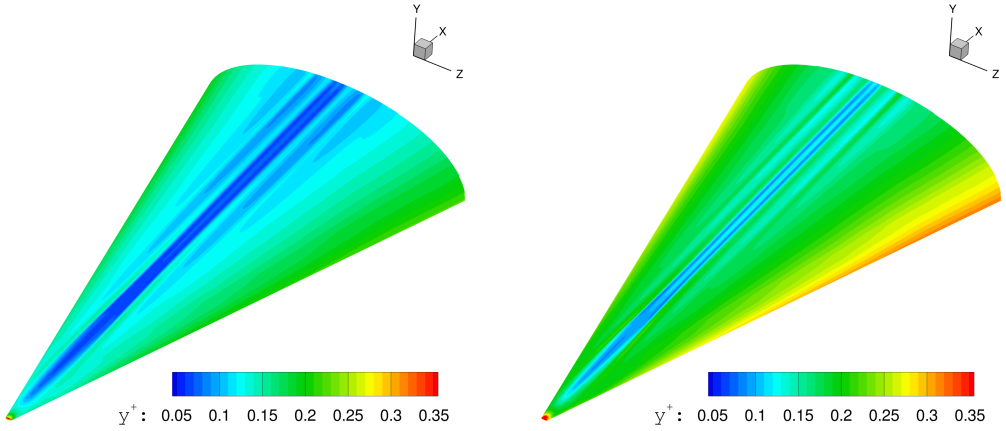

(a) Low Re (b) High Re

Figure B.1: Values of y^+ on the surface for both Reynolds numbers.

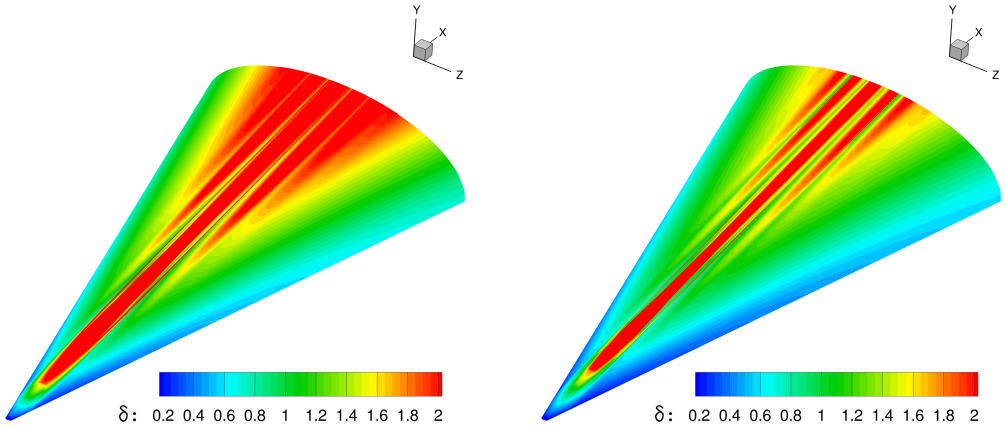

(a) Low Re (b) High Re

Figure B.2: Boundary layer height δ in mm over the surface for both Reynolds numbers. δ was calculated using the "return from enthalpy overshoot" method.

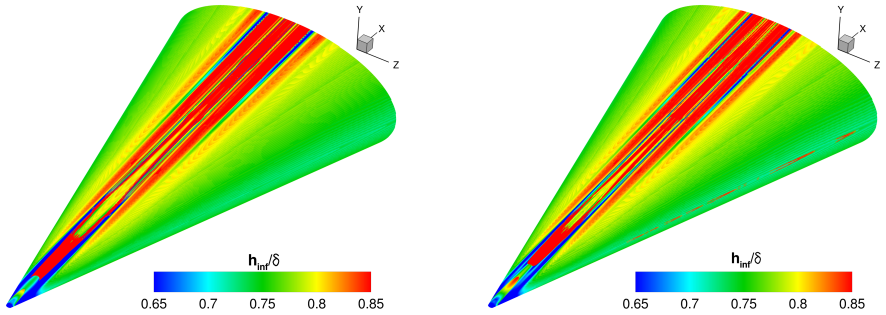

(a) Low Re (b) High Re

Figure B.3: Height of the generalized momentum inflection of the crossflow profile normalized by boundary layer height, plotted on the surface for both Reynolds numbers.

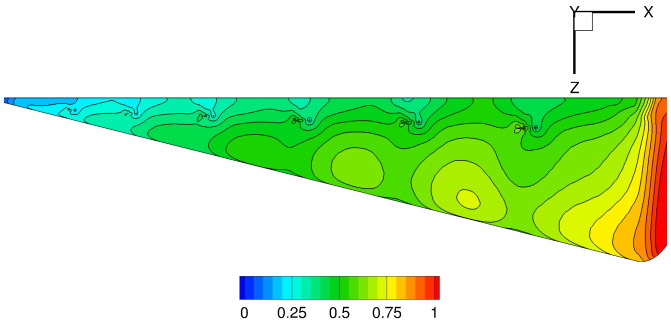

(a) Coarse grid

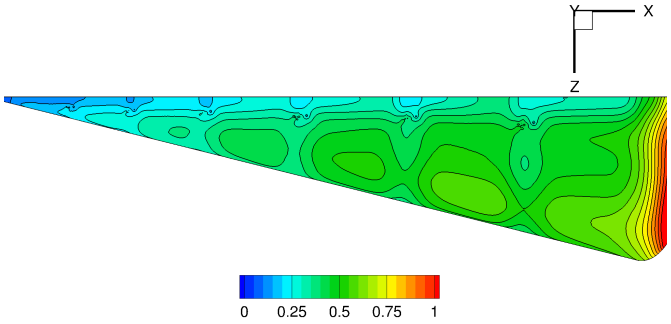

(b) Medium grid

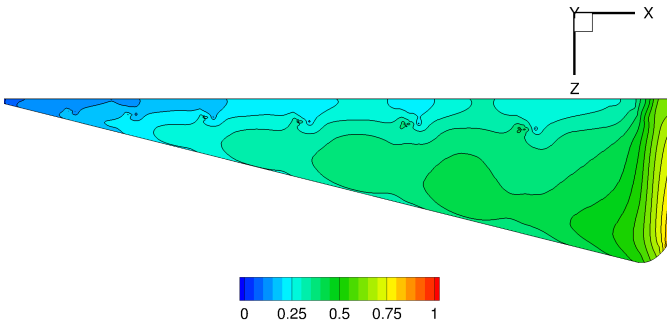

(c) Fine grid

Figure B.4: Characteristic grid wavelength over the surface for each mesh. This can be thought of as twice the local cell width, and scrutinizes the grid quality and effect of singularities.

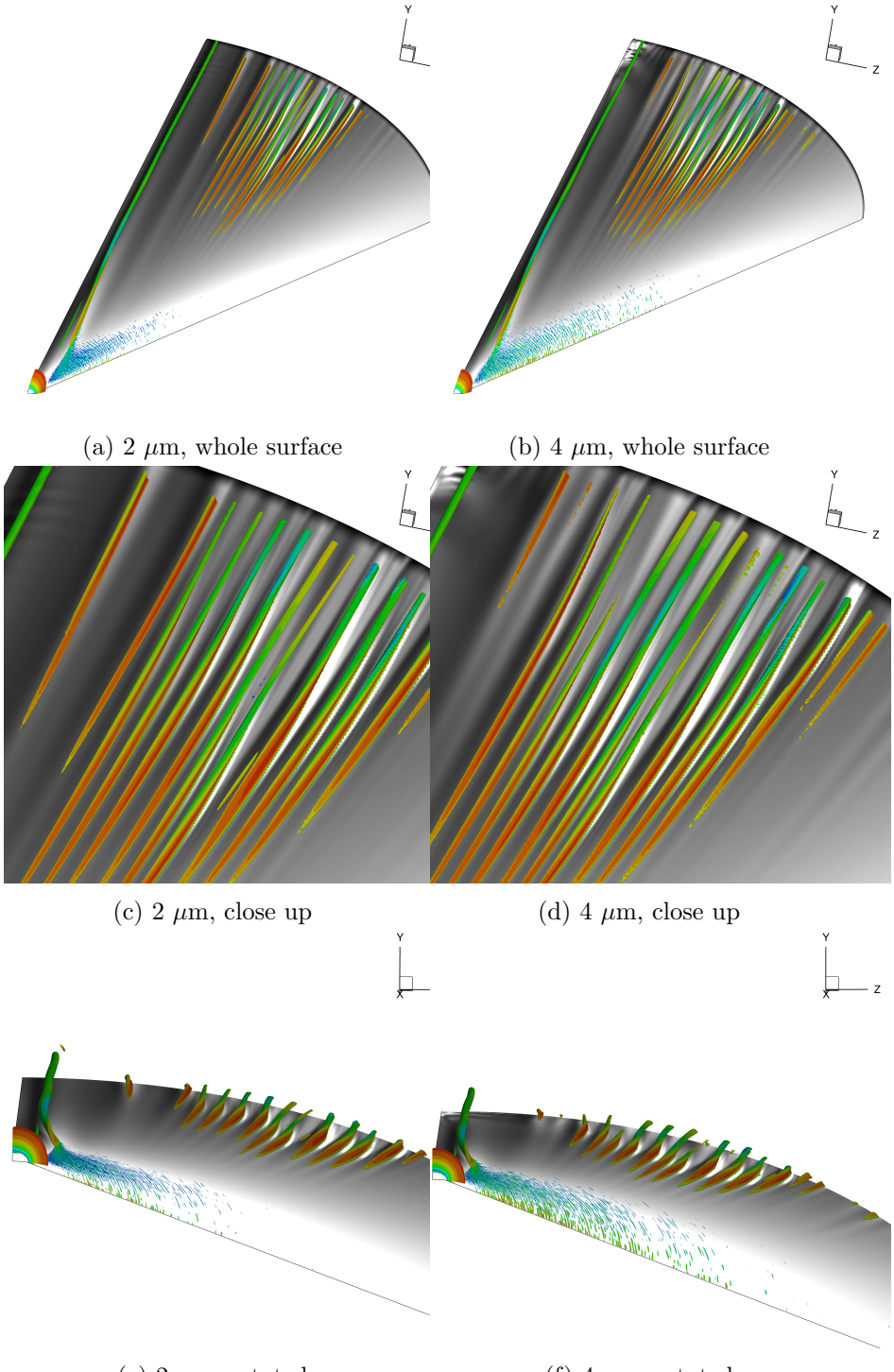

(a) 2 μm, whole surface

(b) 4 μm, whole surface

(c) 2 μm, close up

(d) 4 μm, close up

(e) 2 μm, rotated

(f) 4 μm, rotated

Figure B.5: Isosurfaces of Q–criterion colored by streamwise velocity component overlaid onto surface heat flux for 2 μm and 4 μm cases.

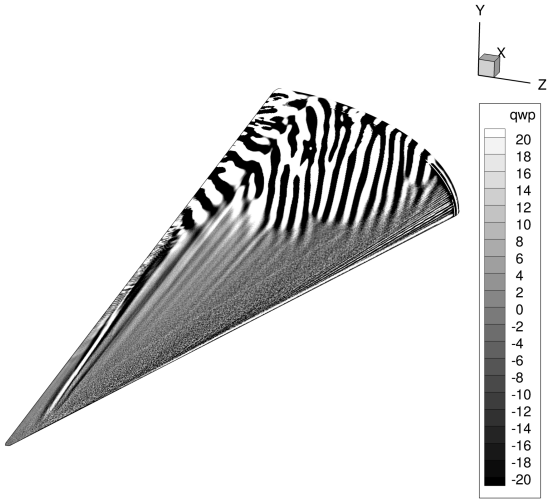

(a) Low Re

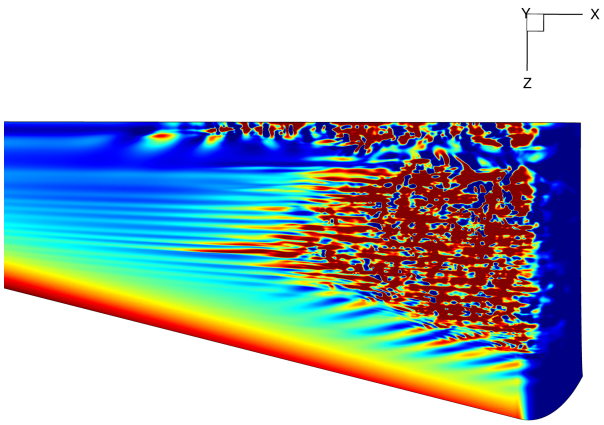

(b) High Re

Figure B.6: Examples of start–up transients while converging to steady state.

Appendix C

Baseflow Comparison of US3D and BCFD at Low Re

In this appendix, low Re baseflow computations of HIFiRE–5 using US3D and Boeing CFD (BCFD) are compared. The US3D computation from this work uses the 105M element (Medium) grid. The BCFD computation was done by Matthew Lakebrink at Purdue University[64], and uses a 141 million element grid of triangular prisms and a Roe flux scheme. Despite the differences in grid and scheme, the computations agree excellently. Only minor differences can be seen near the centerline at the back of the geometry, due to the boundary plume extending up and out of the region of interest for the US3D grid, and perhaps due to edge effects near the back of the domain (the US3D grid has a lip at the back and the BCFD grid does not). It should also be noted that slices from the US3D solution were interpolated to planes that were constant in x, and so the solution is misrepresented far away from the body where the cells are very coarse. The effect of the interpolation is to make the shock appear dissipated, where in the the actual solution this is not the case.

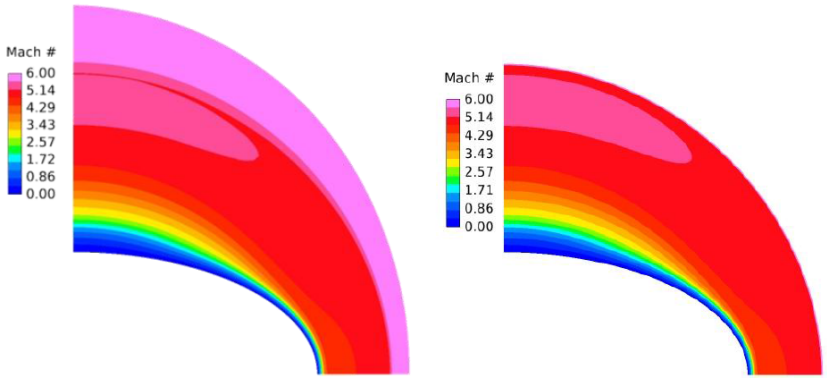

Figure C.1: Mach contours at $x/L = 0.07$, US3D left, BCFD right.

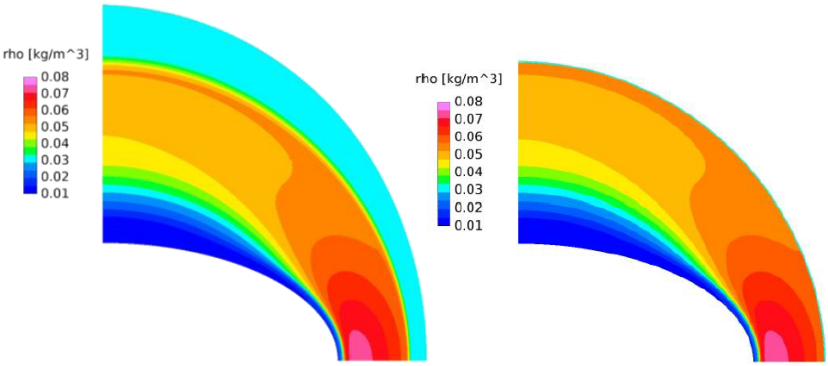

Figure C.2: Density contours at $x/L = 0.07$, US3D left, BCFD right.

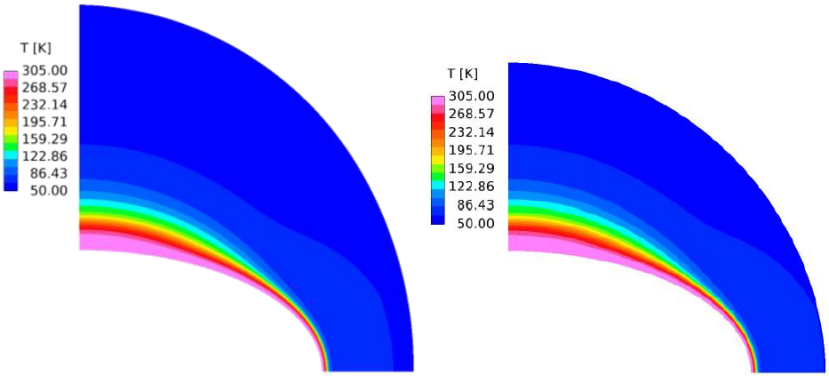

Figure C.3: Temperature contours at $x/L = 0.07$, US3D left, BCFD right.

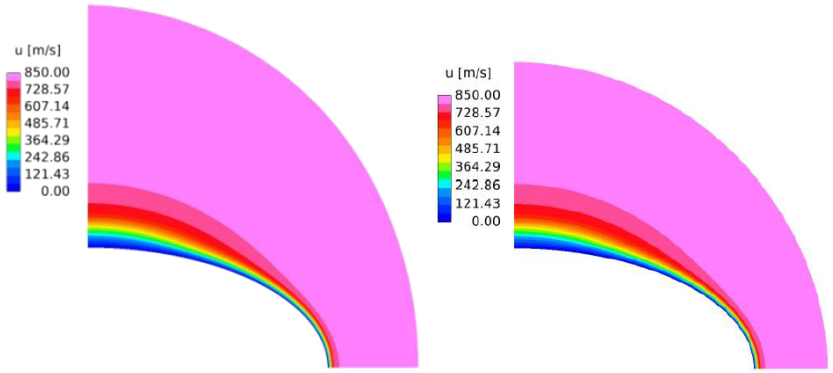

Figure C.4: u contours at $x/L = 0.07$, US3D left, BCFD right.

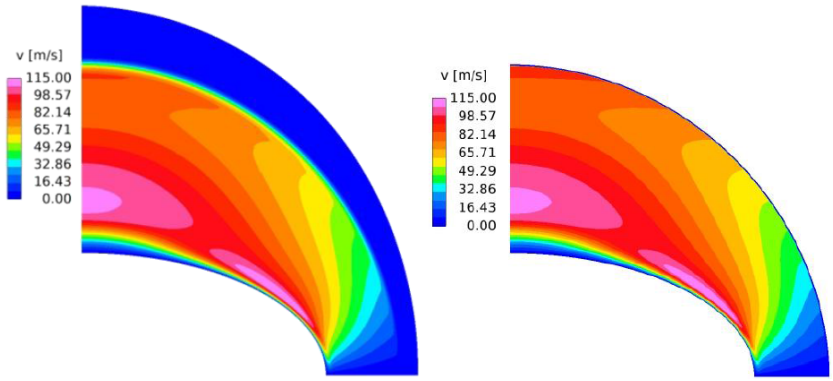

Figure C.5: v contours at $x/L = 0.07$, US3D left, BCFD right.

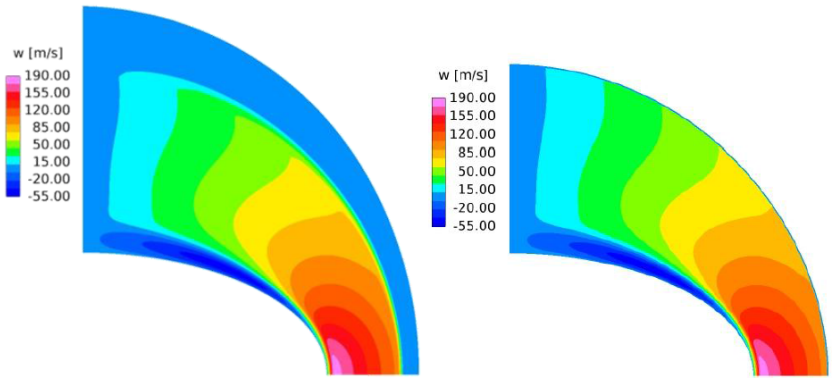

Figure C.6: w contours at $x/L = 0.07$, US3D left, BCFD right.

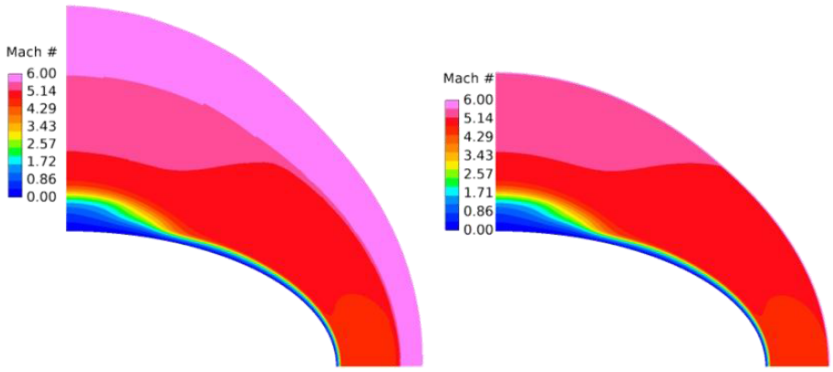

Figure C.7: Mach contours at $x/L = 0.18$, US3D left, BCFD right.

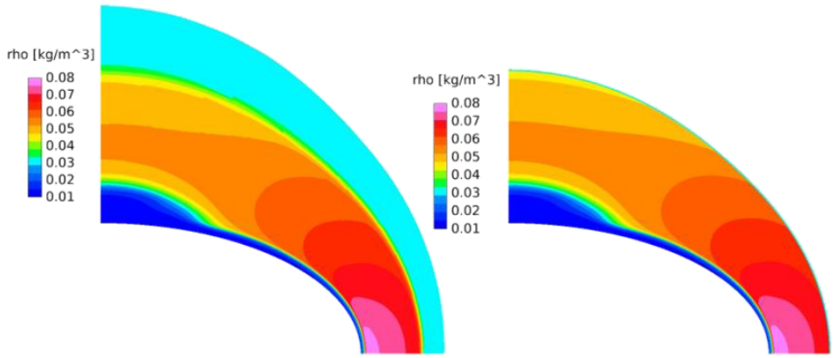

Figure C.8: Density contours at $x/L = 0.18$, US3D left, BCFD right.

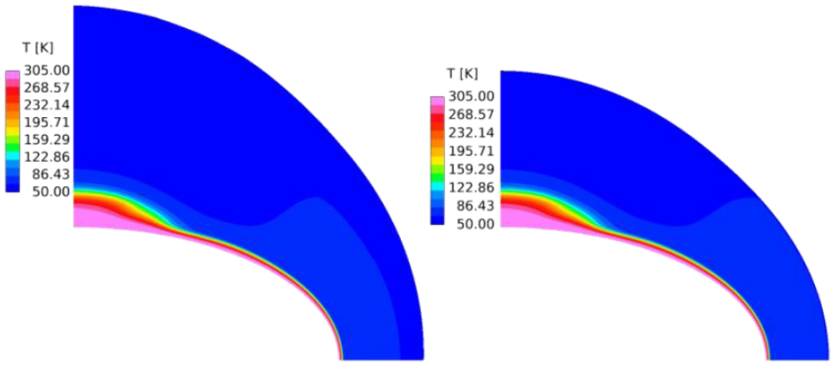

Figure C.9: Temperature contours at $x/L = 0.18$, US3D left, BCFD right.

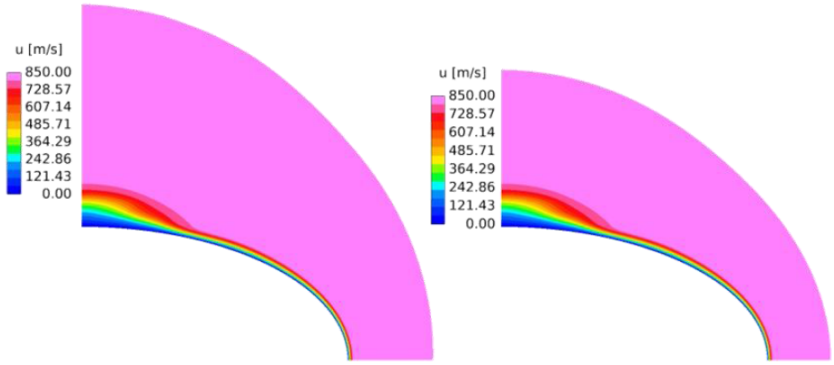

Figure C.10: u contours at $x/L = 0.18$, US3D left, BCFD right.

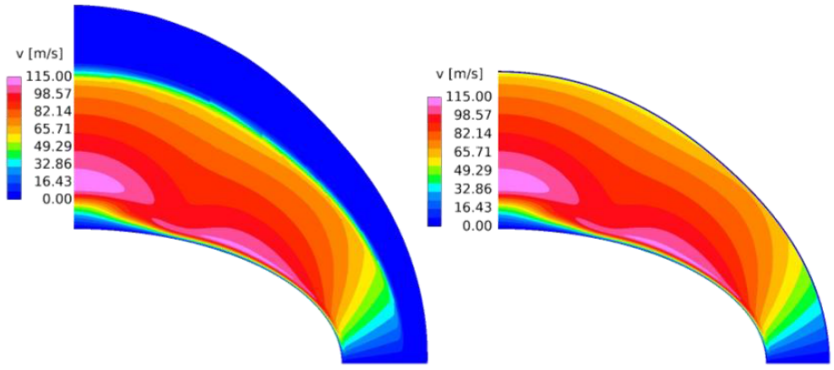

Figure C.11: v contours at $x/L = 0.18$, US3D left, BCFD right.

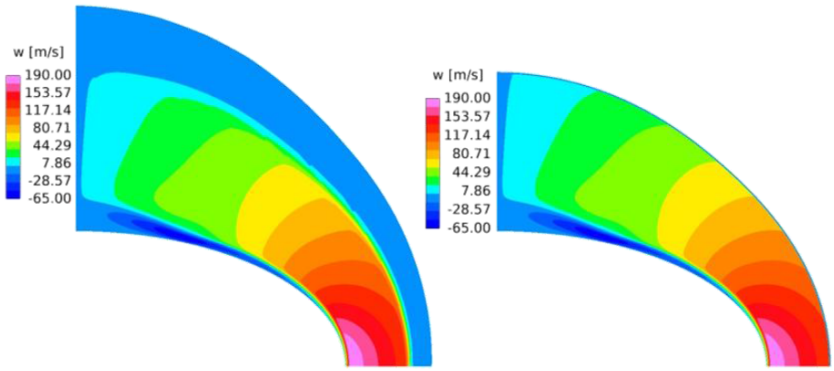

Figure C.12: w contours at $x/L = 0.18$, US3D left, BCFD right.

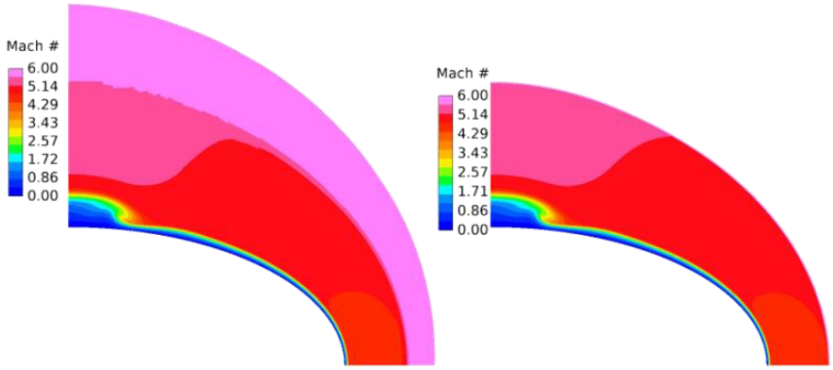

Figure C.13: Mach contours at $x/L = 0.3$, US3D left, BCFD right.

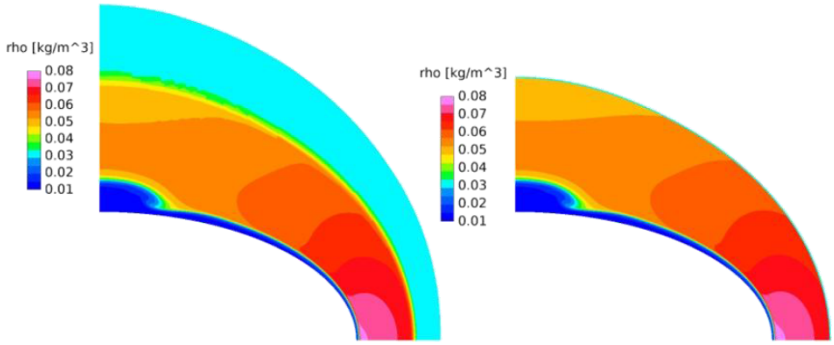

Figure C.14: Density contours at $x/L = 0.3$, US3D left, BCFD right.

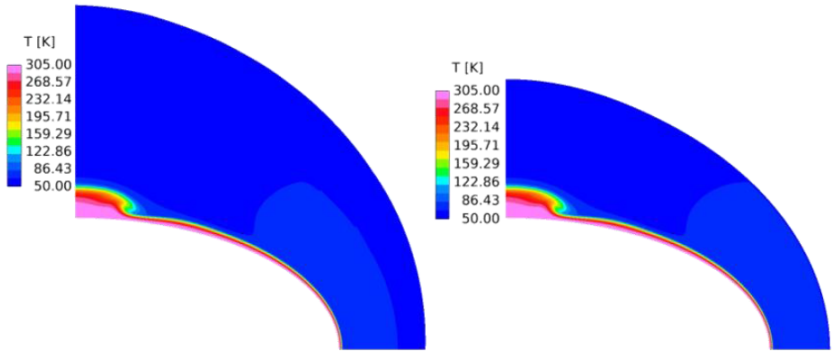

Figure C.15: Temperature contours at $x/L = 0.3$, US3D left, BCFD right.

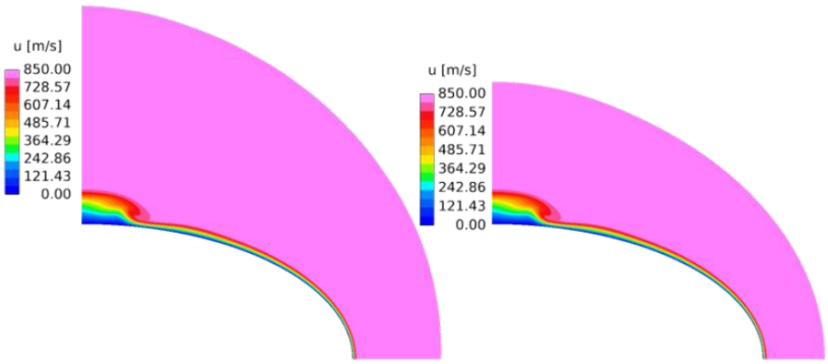

Figure C.16: u contours at $x/L = 0.3$, US3D left, BCFD right.

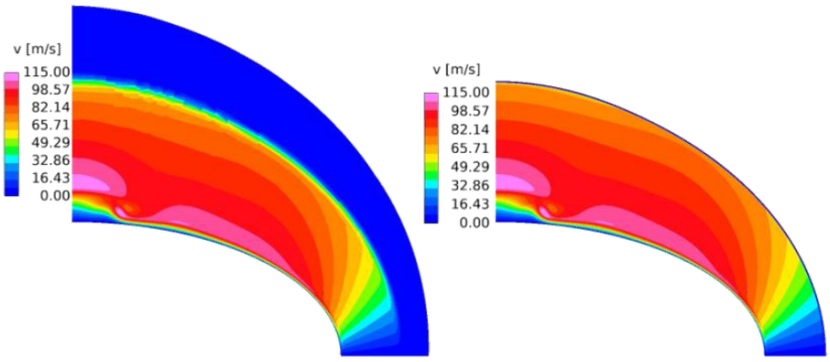

Figure C.17: v contours at $x/L = 0.3$, US3D left, BCFD right.

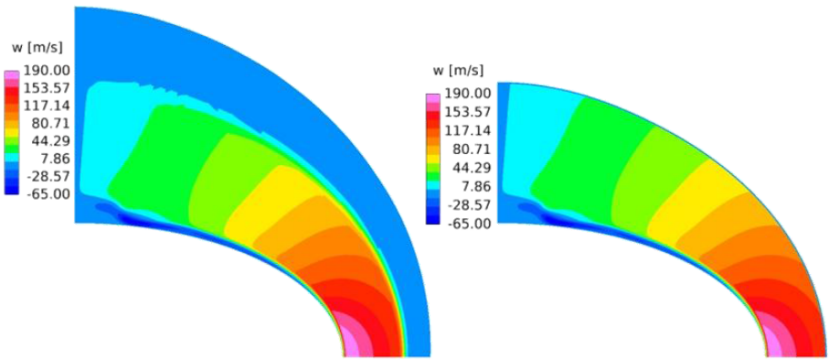

Figure C.18: w contours at $x/L = 0.3$, US3D left, BCFD right.

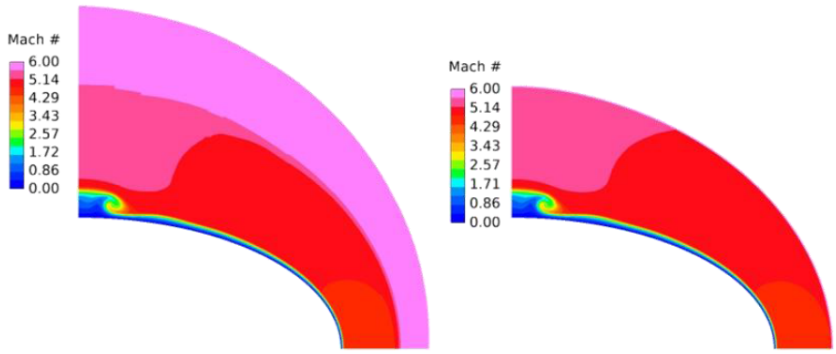

Figure C.19: Mach contours at $x/L = 0.42$, US3D left, BCFD right.

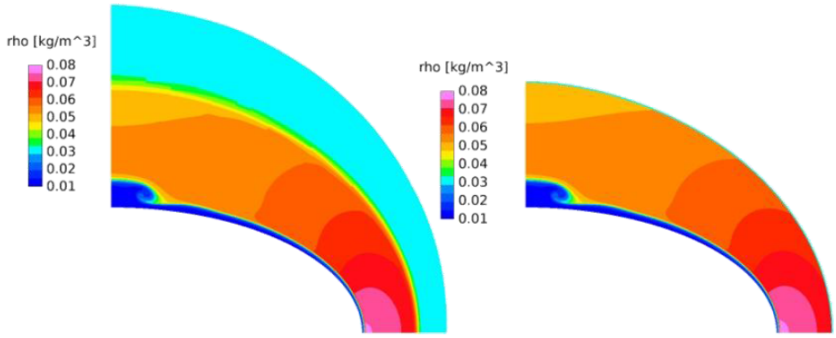

Figure C.20: Density contours at $x/L = 0.42$, US3D left, BCFD right.

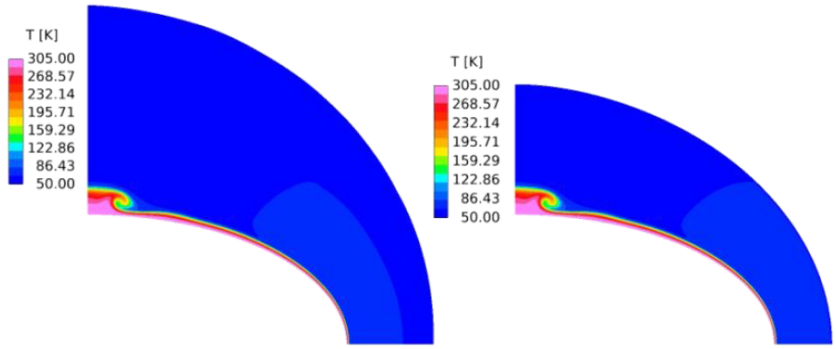

Figure C.21: Temperature contours at $x/L = 0.42$, US3D left, BCFD right.

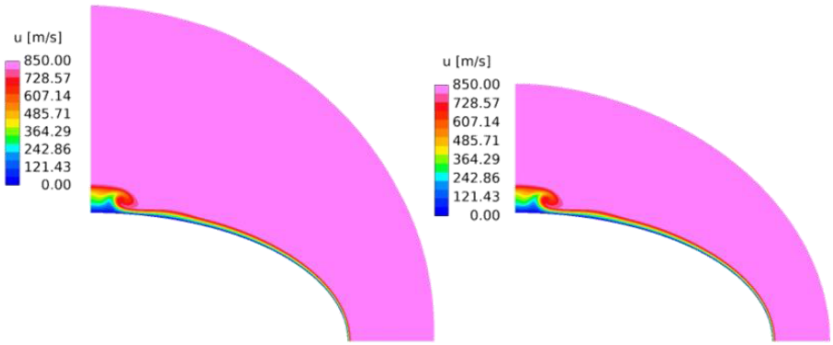

Figure C.22: u contours at $x/L = 0.42$, US3D left, BCFD right.

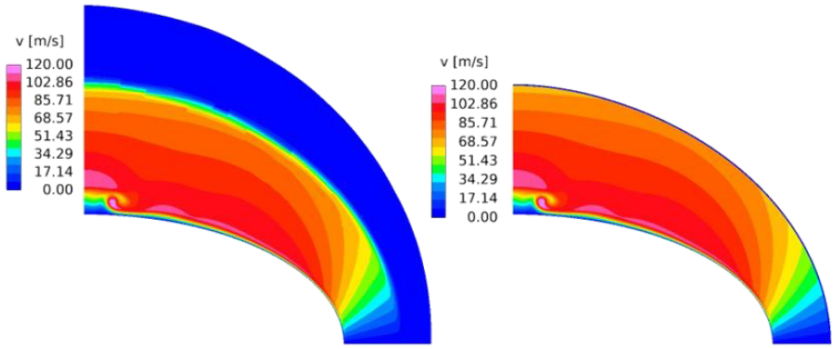

Figure C.23: v contours at $x/L = 0.42$, US3D left, BCFD right.

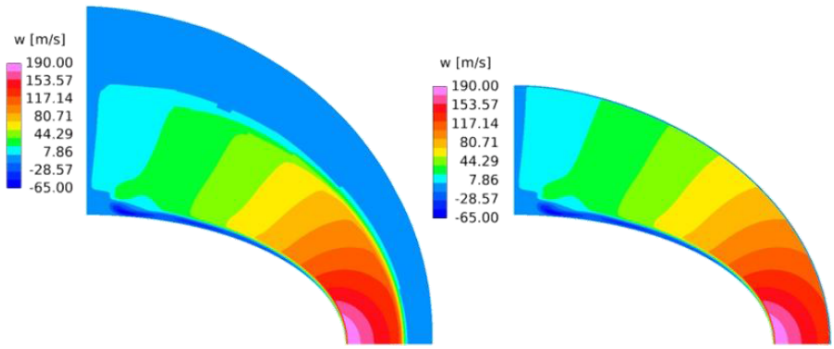

Figure C.24: w contours at $x/L = 0.42$, US3D left, BCFD right.

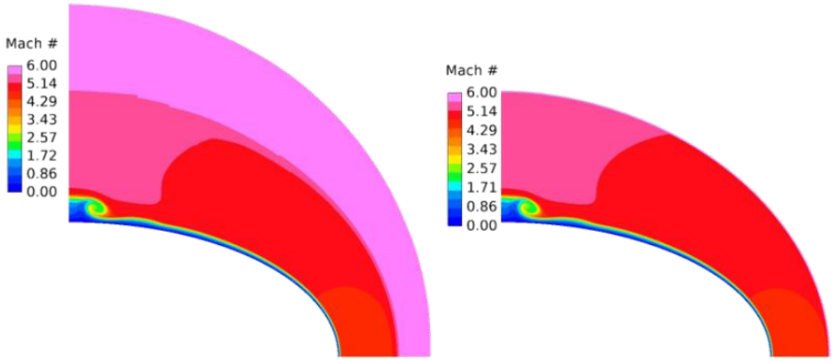

Figure C.25: Mach contours at $x/L = 0.54$, US3D left, BCFD right.

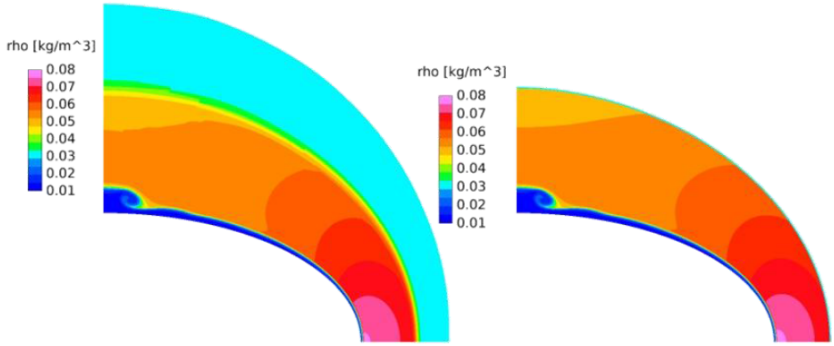

Figure C.26: Density contours at $x/L = 0.54$, US3D left, BCFD right.

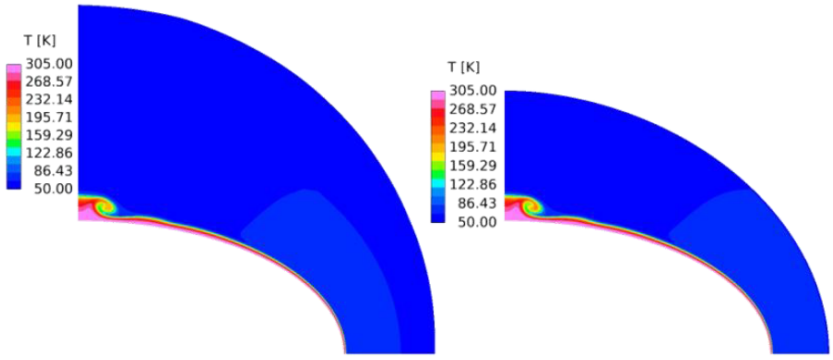

Figure C.27: Temperature contours at $x/L = 0.54$, US3D left, BCFD right.

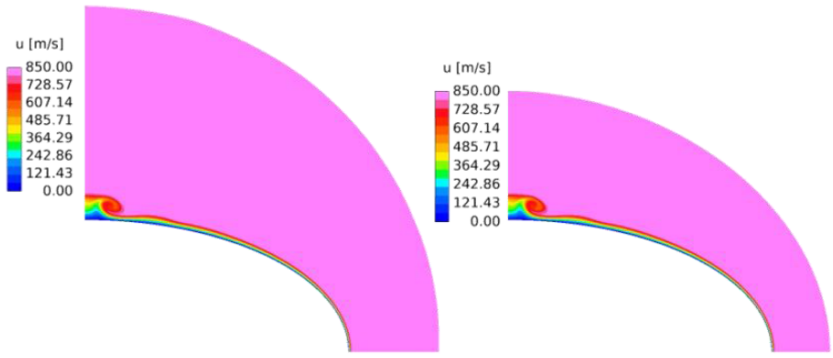

Figure C.28: u contours at $x/L = 0.54$, US3D left, BCFD right.

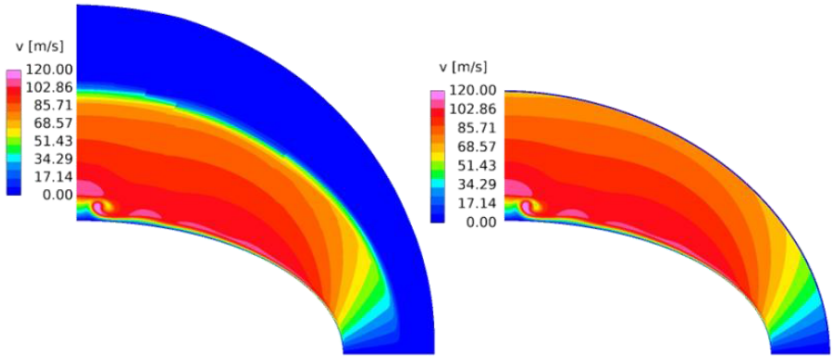

Figure C.29: v contours at $x/L = 0.54$, US3D left, BCFD right.

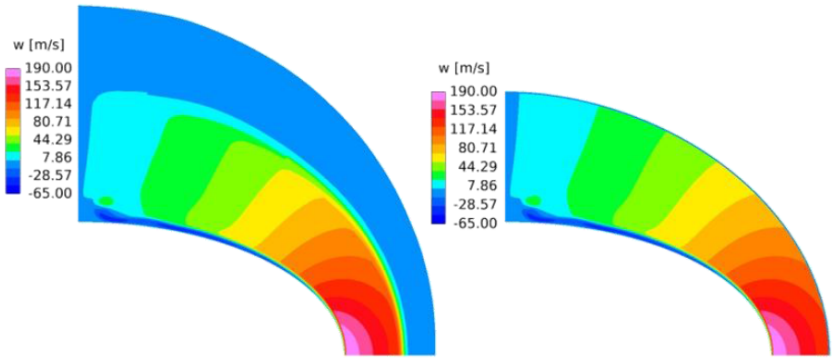

Figure C.30: w contours at $x/L = 0.54$, US3D left, BCFD right.

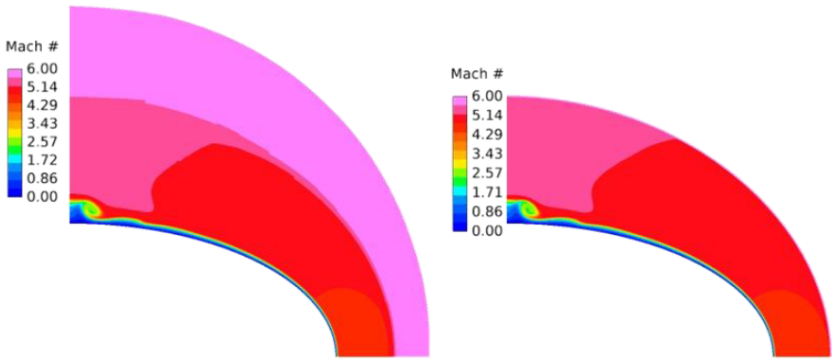

Figure C.31: Mach contours at $x/L = 0.69$, US3D left, BCFD right.

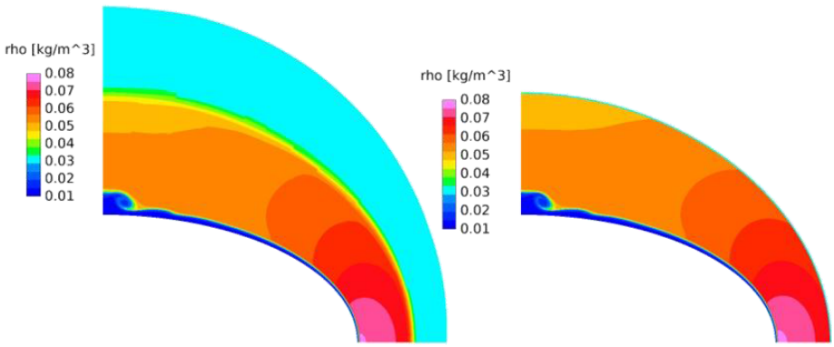

Figure C.32: Density contours at $x/L = 0.69$, US3D left, BCFD right.

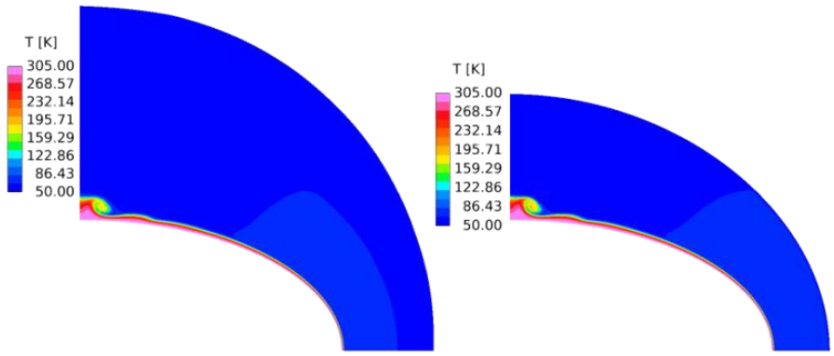

Figure C.33: Temperature contours at $x/L = 0.69$, US3D left, BCFD right.

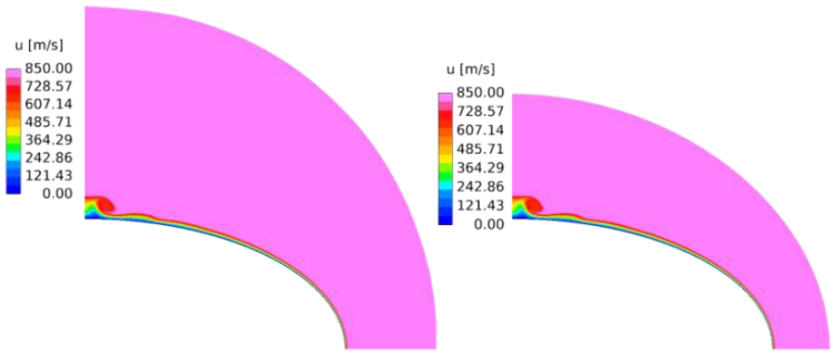

Figure C.34: u contours at $x/L = 0.69$, US3D left, BCFD right.

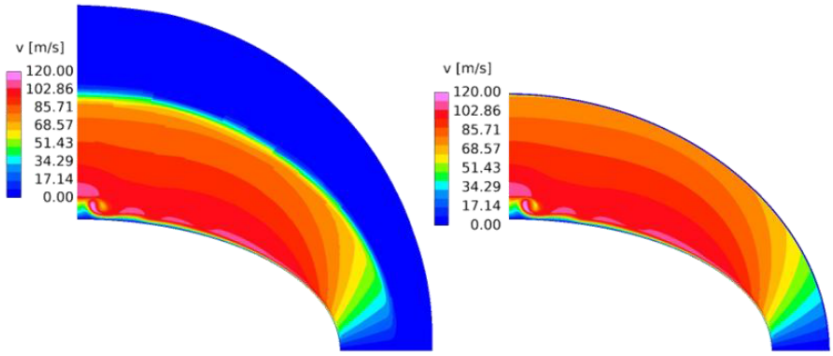

Figure C.35: v contours at $x/L = 0.69$, US3D left, BCFD right.

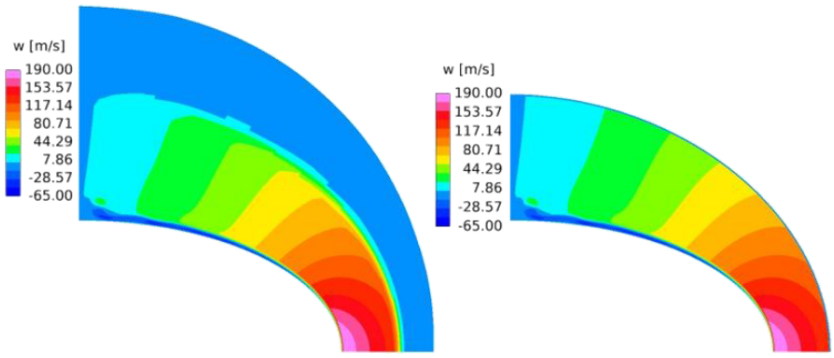

Figure C.36: w contours at $x/L = 0.69$, US3D left, BCFD right.

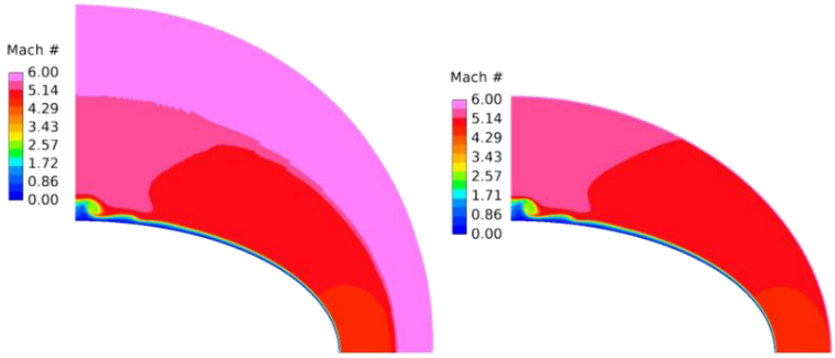

Figure C.37: Mach contours at $x/L = 0.83$, US3D left, BCFD right.

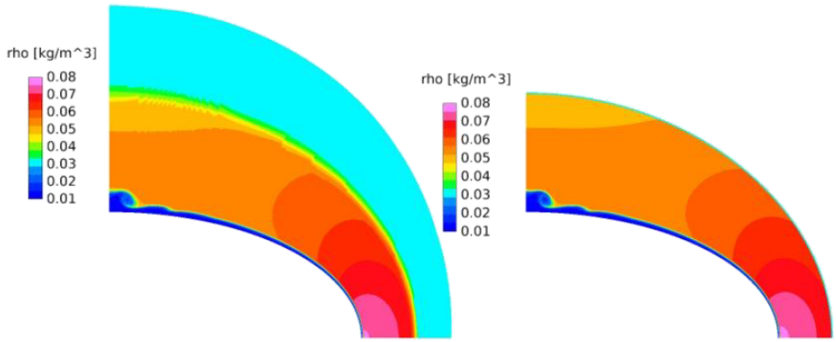

Figure C.38: Density contours at $x/L = 0.83$, US3D left, BCFD right.

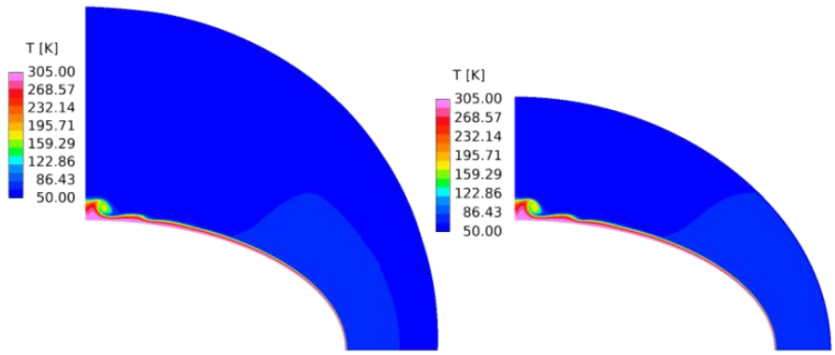

Figure C.39: Temperature contours at $x/L = 0.83$, US3D left, BCFD right.

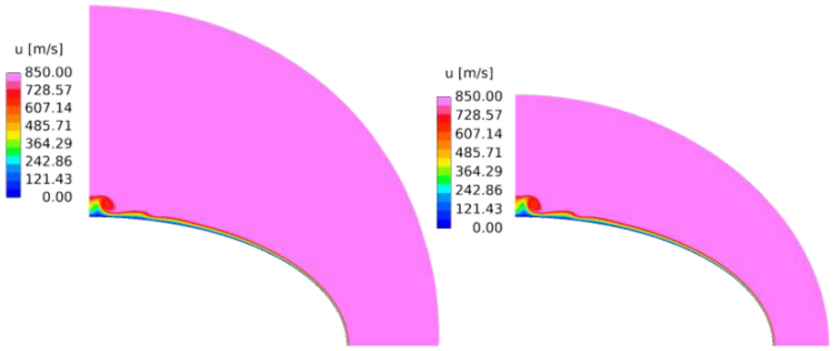

Figure C.40: u contours at $x/L = 0.83$, US3D left, BCFD right.

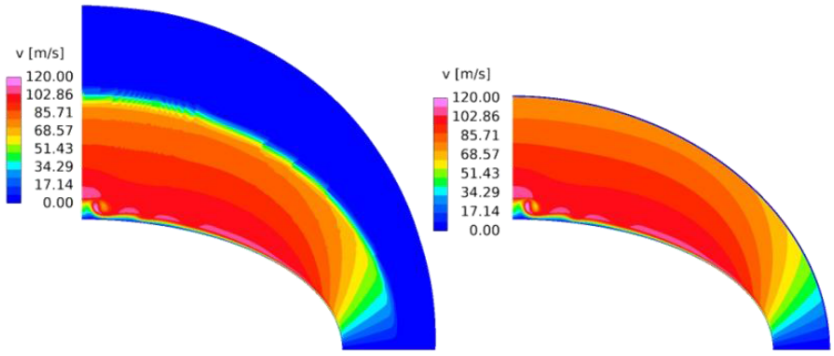

Figure C.41: v contours at $x/L = 0.83$, US3D left, BCFD right.

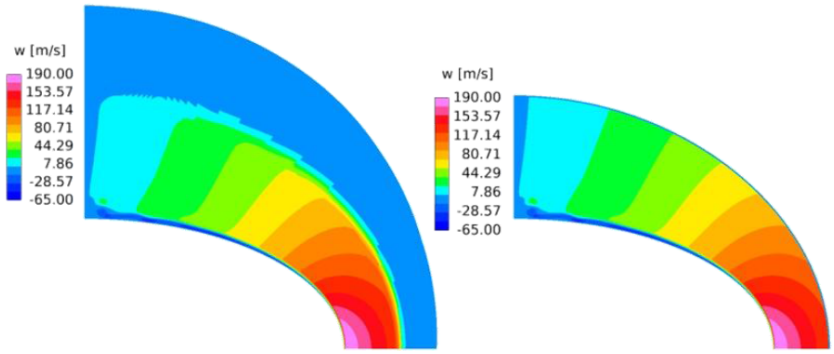

Figure C.42: w contours at $x/L = 0.83$, US3D left, BCFD right.

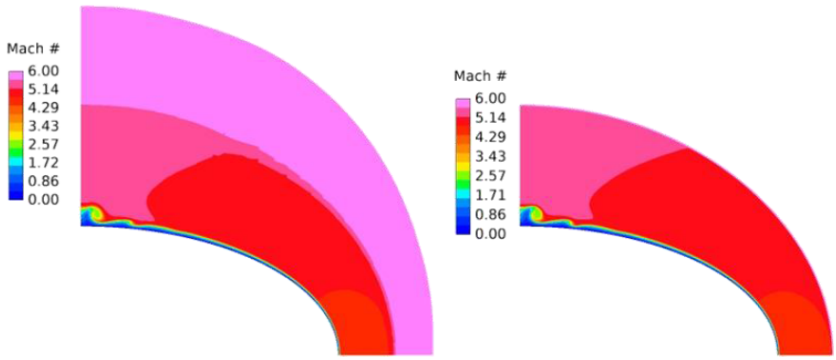

Figure C.43: Mach contours at $x/L = 0.99$, US3D left, BCFD right.

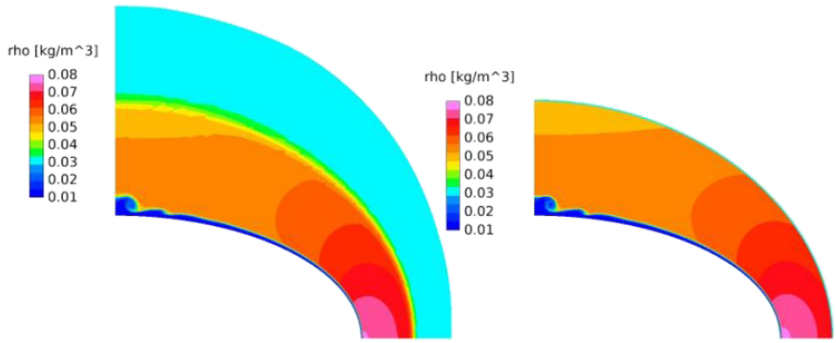

Figure C.44: Density contours at $x/L = 0.99$, US3D left, BCFD right.

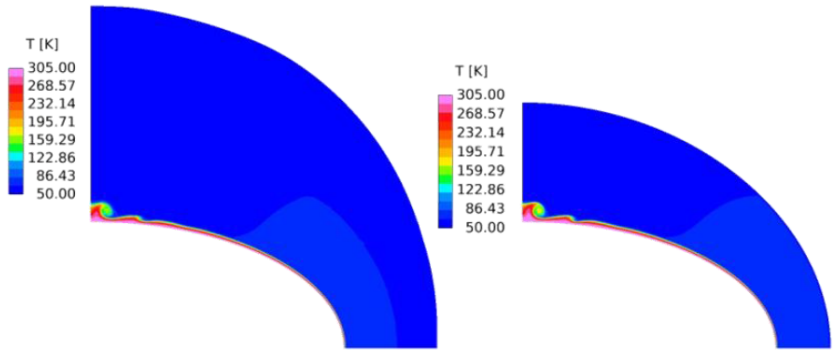

Figure C.45: Temperature contours at $x/L = 0.99$, US3D left, BCFD right.

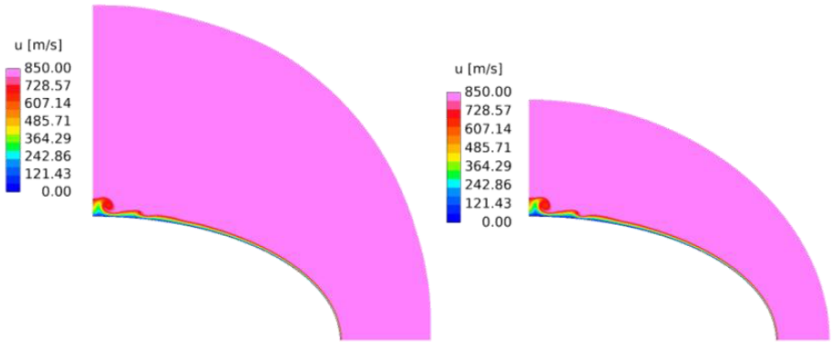

Figure C.46: u contours at $x/L = 0.99$, US3D left, BCFD right.

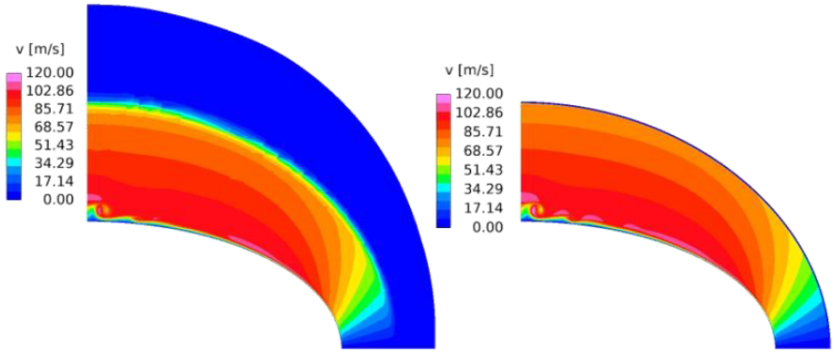

Figure C.47: v contours at $x/L = 0.99$, US3D left, BCFD right.

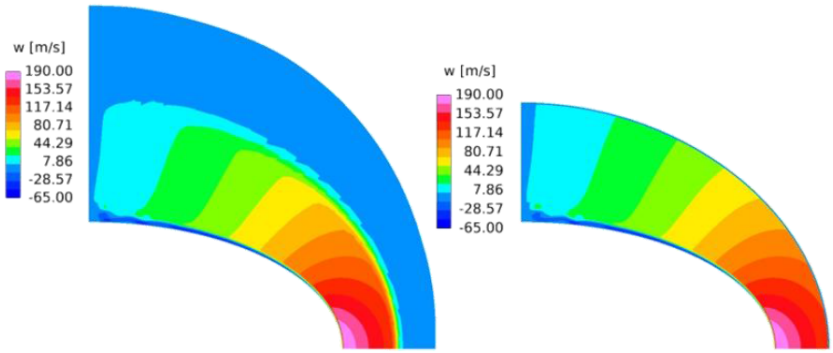

Figure C.48: w contours at $x/L = 0.9$, US3D left, BCFD right.

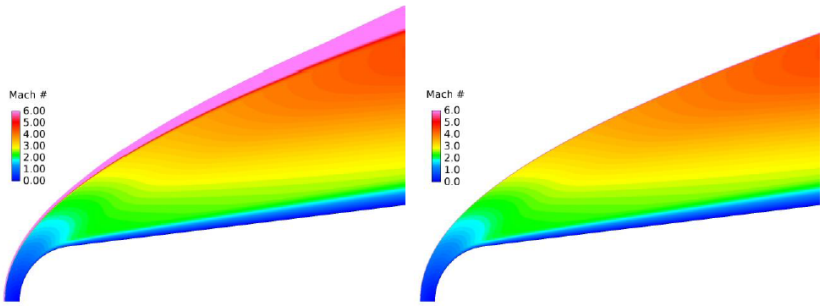

Figure C.49: Mach contours at $z = 0$, US3D left, BCFD right.

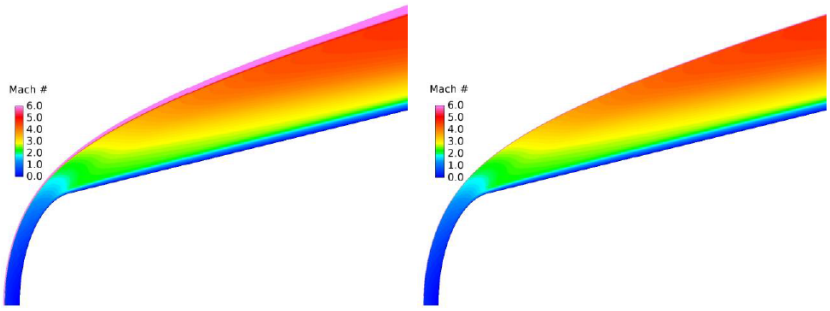

Figure C.50: Mach contours at $y = 0$, US3D left, BCFD right.